STRUCTURE AND FUNCTION OF SWITCHABLE SURFACES

by

David Peng

A dissertation submitted in partial fulfillment
of the requirements for the degree of
Doctor of Philosophy
(Chemical Engineering)
in The University of Michigan
2007

Doctoral Committee:

Assistant Professor Joerg Lahann, Chair
Professor Ronald G. Larson
Professor Carol A. Fierke
Assistant Professor Michael Mayer

ACKNOWLEDGEMENTS

To my advisor, Professor Joerg Lahann, for his brilliant ingenuity, his endless drive, his expert guidance, and above all, for his belief in me when things got tough. To Professors Ron Larson, Carol Fierke, and Michael Mayer for their helpful feedback on my dissertation.

To Himabindu Nandivada for her lifeline of support and friendship since day one. To Kyung Ho Roh, Hsien-Yeh Chen, Allison Bourke, Allen Ahang Ahmadi, Mutsumi Yoshida, and Yaseen Elkasabi for being such great colleagues and such great friends. To all the other members of the Lahann Lab, past and present—Sandy Yu, Agusti Panades Llorens, Marc Aluma Lopez, Gemma Galvan Paris, Sonsoles de Olano Biada, Srijanani Bhaskar, Aiwu Sun, Abbass Kazemi, Xuwei Jiang, Lidija Bondarenko, Joseph Lai, Sridhar Valluri, David Alberts, Laura Chang, Eric Chang, and Daniel Schmidt—for adding so much to my Ph.D. experience.

To Tom Durkee for his impact on my life. To Charissa Huang and Julia Chung for their valuable friendship. To Sarah Young for her influence. To Philip Lester, Josefine Persson, Katherine Hu, and Michael Betenbaugh for their continued influence. To my sister, Carol Peng, for the high example she sets.

And to my parents, Chu-Shun and Anne Peng, for providing the foundation for all of my achievements and for their constant support and encouragement.

To all, my deepest love and gratitude.

TABLE OF CONTENTS

LIST OF FIGURES

LIST OF TABLES

ABSTRACT

The loosely-packed structure of low-density self-assembled monolayers (SAMs) enables the constituent molecules of these surfaces to undergo reversible conformational transitions in response to electrical stimulation, leading to controllable changes in macroscopic surface properties such as wettability. This dissertation reports key new findings on the structure and function of these dynamically switchable surfaces.

Low-density SAMs can switch their electrochemical impedance properties in response to applied electrical potential. This function is tunable, such that the magnitude of the impedance response can be selected by the user, and reversible, such that the material can be returned to its initial state after switching. These switchable impedance characteristics are exhibited by low-density SAMs of both 16-carbon and 11-carbon chain length, assembled on both gold and silver.

Low-density SAMs show robust stability in long-term storage conditions including air, argon at room temperature, argon at 4 °C, and ethanol. Analyses by infrared spectroscopy, electrochemical impedance spectroscopy, and X-ray photoelectron spectroscopy reveal the insensitivity of low-density SAMs to degradative phase-segregation, adventitious contamination, and oxidation.

Thiolates within a SAM can migrate laterally from high-density regions into low-density regions. This phenomenon is a function of temperature, with higher temperatures promoting greater lateral mobility, and a function of SAM chain length, with shorter

SAMs exhibiting mobility at lower thermal thresholds as a result of their weaker inter-chain interactions.

Low-density SAMs also have interstitial spaces between their thiolates which can accept the intercalation of linear hydrophobic and amphiphilic analyte molecules. Electrochemical impedance spectroscopy, infrared spectroscopy, and surface plasmon resonance analysis reveal the intercalation of stearic acid, palmitic acid, and octadecyl rhodamine into low-density SAMs, with more polar solvents encouraging greater levels of intercalation.

This dissertation thus expands our understanding of the unique characteristics of switchable low-density SAMs, providing a foundation for further study, optimization, and innovation. Such developments may ultimately lead to next-generation technologies such as diagnostic sensors for non-invasive detection of disease markers and dynamic substrates for cell growth and tissue development.

CHAPTER 1

INTRODUCTION

Background

"Stimuli-responsive" or "smart" materials are defined as synthetic materials that experience dramatic changes in physicochemical properties when subjected to small environmental influences. In biologically-related areas such as drug delivery, tissue engineering, and biosensors, the development of smart materials is providing new systems and devices with a level of responsiveness to micro- and nano-environments previously unachievable with conventional materials. The promises of drug carriers with programmable release profiles, of dynamic substrates for cell growth and tissue development, and of self-controlling *in vivo* diagnostic devices all can be brought a step closer to reality by advances in smart materials.

Smart surfaces find direct routes of application in areas such as tissue engineering and biosensors due to the importance of cell-surface or biomolecule-surface interactions in the function of biomedical materials and devices. In these applications, control over surface hydrophobicity/hydrophilicity (wettability) is critical. In tissue engineering studies, for example, cells will adhere only to relatively hydrophobic surfaces—thus, responsiveness of surface wettability is desirable for being able to attach or release cells on command[1,2] or to culture two different types of cells on patterned substrates for cell-

cell interaction studies.[3] In biosensor applications, surface wettability strongly influences non-specific binding of proteins, which can interfere with sensor specificity. Surface responsiveness would be desirable for controlling sensor activation and for regeneration of sensor function after a sensing event.

A variety of methods have been devised for fabrication of surfaces with smart wettability properties. Many of these methods rely on polymer components to confer environmental responsiveness to the surface. Grafting of thermo-responsive polymers has been achieved on various substrates such as silica, [4] gelatin, [5] and hyaluronic acid. [6] Grafting of one end of a solvent-responsive polymer to silica yielded a smart "polymer brush" system.[7] Deposition of a smart fluorinated liquid crystalline polymer on aluminum yielded a surface with switchable wettability and tackiness.[8] Oxidative chemical treatment of a polymer surface yielded a temperature-responsive film.[9] Synthesis of a hydrophilic-hydrophobic block copolymer yielded a surface responsive to solvent environment.[10] Mixing of a block copolymer and a homopolymer, followed by partitioning of the copolymer to the air/polymer interface, yielded a surface responsive to environmental humidity.[11] An elastin-like polypeptide, a thermo-responsive polymer, was adsorbed onto a self-assembled monolayer of mercaptoundecanoic acid on gold nanoparticles, which aggregated upon heating.[12] The chemical versatility of polymers makes this wide range of surface fabrication methods possible.

Unadorned self-assembled monolayers (SAMs), devoid of polymer adsorbates and grafts, form the foundation for another major class of smart surfaces. These surfaces are generally triggered by factors other than temperature, pH, and solvent environment—the factors which trigger most polymer-based surfaces. One study used a SAM of

pyrimidine-terminated thiols to form a photo-responsive surface capable of reversible wettability transitions.[13] Another photo-responsive surface was prepared using a SAM of macrocyclic amphiphile molecules on silica.[14] Wettability switching of an electro-responsive SAM of alkanethiols was based on electrochemical desorption/resorption of the monolayer.[15] And recently, an ion-exchange-responsive SAM of imidazolium-terminated molecules was formed on silica.[16]

In the context of these studies, the development of the switchable self-assembled monolayer, pictured in Figure 1.1, represents a key development in smart surfaces.[17] This monolayer of 16-mercaptohexadecanoic acid (MHA) on gold was designed to self-assemble in a low-density configuration, with increased separation between molecules on the surface and thus with reduced steric hindrance effects, giving the molecules of the monolayer freedom to assume bent conformations without interference from their neighbors. When a positive electrical potential is applied to the gold surface, the negatively-charged carboxyl head groups of MHA experience electrostatic attraction to the surface, causing the molecule to bend into a loop conformation. This switches the monolayer from a hydrophilic state (with surface exposure of polar carboxyl groups) to a hydrophobic state (with surface exposure of apolar aliphatic carbon chains). The concerted conformational transitions across the entire monolayer lead to a macroscopically observable change in surface wettability upon switching. The monolayer can switch reversibly from hydrophilic to hydrophobic and vice versa by application and removal of the electrical stimulus. Unlike polymer-based smart surfaces, this surface does not depend on changes in the solution environment in order to exhibit wettability changes. And unlike other self-assembled-monolayer-based smart surfaces, the switching

mechanism relies solely on conformational transitions; chemical reactions are not required to alter its surface properties. These characteristics make the low-density switchable SAM well-suited for applications such as biomolecular sensing.

Overview of Dissertation

This dissertation aims to extend our understanding of the structure and function of low-density self-assembled monolayers by answering four key questions:

(1) What influence does applied potential have on the electrochemical behavior of low-density SAMs?

(2) How stable are low-density SAMs in long-term storage conditions?

(3) Does elevated temperature affect low-density SAM structure either detrimentally or in a way that exhibits previously unobserved behavior?

(4) Do analyte molecules in solution interact with low-density SAMs in a way that could lead to potential applications in diagnostic devices?

The following chapters address each of these questions successively, leading us to a deeper understanding of the properties and capabilities of this unique technology platform.

Figure

Lahann *et al. Science* (2003)

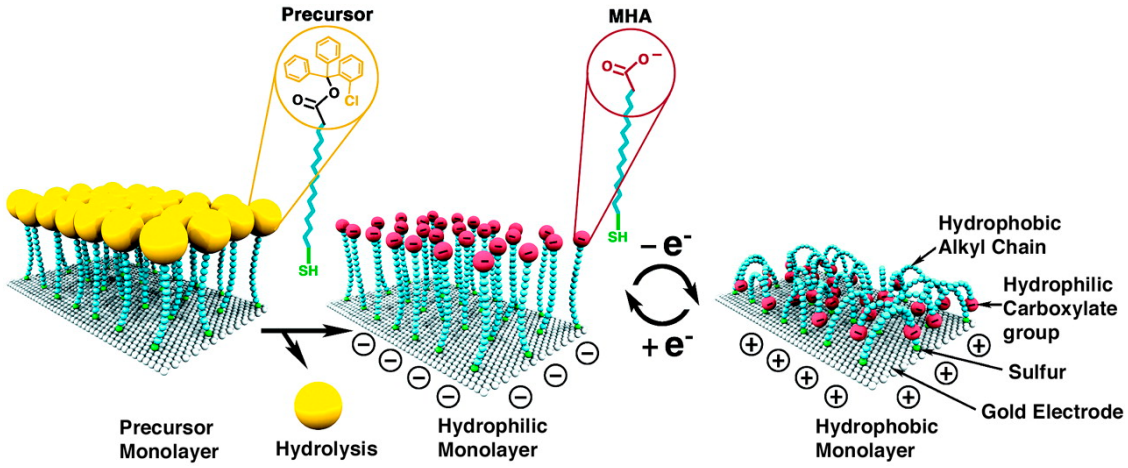

Figure 1.1. Illustration of the preparation and switching of a low-density self-assembled monolayer of mercaptohexadecanoic acid on gold.

References

(1) Schmaljohann, D.; Oswald, J.; Jorgensen, B.; Nitschke, M.; Beyerlein, D.; Werner, C. *Biomacromolecules* **2003**, *4*, 1733-1739.

(2) Okano, T.; Yamada, N.; Okuhara, M.; Sakai, H.; Sakurai, Y. *Biomaterials* **1995**, *16*, 297.

(3) Yamato, M., Konno, C., Utsumi, M., Kikuchi, A., Okano, T. *Biomaterials* **2002**, *23*, 561-567.

(4) Yakushiji, T., Sakai, K. *Langmuir* **1998**, *14*, 4657-4662.

(5) Morikawa, H., Matsuda, T. *J. Biomater. Sci. Polym Ed.* **2002**, *13*, 167-183.

(6) Ohya, S., Nakayama, Y., Matsuda, T. *Biomacromolecules* **2001**, *2*, 856-63.

(7) Minko, S., Patil, S., Datsyuk, V., Simon, F., Eichorn, K.-J., Motornov, M., Usov, D., Tokarev, I., Stamm, M. *Langmuir* **2002**, *18*, 289-296.

(8) de Crevoisier, G., Fabre, P., Corpart, J.-M., Leibler, L. *Science* **1999**, *285*, 1246-1249.

(9) Carey, D.H., Ferguson, G.S. *J. Am. Chem. Soc* **1996**, *118*, 9780-9781.

(10) Shenshu, K., Yamashita, S., Mori, H., Ito, M., Hirao, A., Nakahama, S. *Langmuir* **1999**, *15*, 1754-1762.

(11) Anastasiadis, S.H., Retsos, H., Pispas, S., Hadjichristidis, N., Neophytides, S. *Macromolecules* **2003**, *36*, 1994-1999.

(12) Nath, N., Chilkoti, A. *J. Am. Chem. Soc*. **2001**, *123*, 8197-8202.

(13) Abbott, S., Ralston, J., Reynolds, G., Hayes, R. *Langmuir* **1999**, *15*, 8923-8928.

(14) Ichimura, K., Oh, S.-K., Nakagawa, M. *Science* **2000**, *288*, 1624-1626.

(15) Abbott, N.L., Gorman, C.B., Whitesides, G.M. *Langmuir* **1995**, *11*, 16-18.

(16) Chi, Y.S., Lee, J.K., Lee, S.-G., Choi, I.S. *Langmuir* **2005**, *21*, 4268-4271.

(17) Lahann, J., Mitragotri S., Tran, T.N., Kaido, H., Sundaram, J., Choi, I.S., Hoffer, S., Somorjai, G.A., Langer, R. *Science* **2003**, *299*, 371-373.

CHAPTER 2

SWITCHING THE ELECTROCHEMICAL IMPEDANCE OF LOW-DENSITY SELF-ASSEMBLED MONOLAYERS

[This chapter has been adapted with minor modifications from the following published article: Peng, D. K.; Yu, S. T.; Alberts, D. J.; Lahann, J. *Langmuir* **2007**, *23*, 297-304.]

Abstract

Because the active remodeling of biointerfaces is a paramount feature of nature, it is very likely that future, advanced biomaterials will be required to mimic at least certain aspects of the dynamic properties of natural interfaces. This need has fueled a quest for model surfaces that can undergo reversible switching upon application of external stimuli. Herein, we report the synthesis and characterization of a model system for studying reversibly switching surfaces based on low-density monolayers of mercaptohexadecanoic acid and mercaptoundecanoic acid. These monolayers were assembled on both gold and silver electrodes. When conducting electrochemical impedance spectroscopy under physiological conditions, these monolayers exhibit significant changes in their electrochemical barrier properties upon application of electrical DC potentials below +400 mV with respect to a standard calomel electrode. We further found the impedance switching to be reversible under physiological conditions. Moreover, the impedance can be fine-tuned by changing the magnitude of the applied electrical potential. Before and

during impedance switching at pH 7.4 in aqueous buffer solutions, the low-density monolayers showed good stability according to grazing angle infrared spectroscopy data. We anticipate low-density monolayers to be potentially useful model surfaces when designing active biointerfaces for cell-based studies or rechargeable biosensors.

Introduction

Although great progress has been made over the past decade in the development of passive cell substrates for biomedical applications,[1-5] future research will need to address the intrinsically static character of such artificial substrates and the functional limitations encountered due to the lack of active, dynamic biomaterial properties.[5,6] At the cell-extracellular matrix (ECM) interface, both cell receptors and ECM proteins undergo rapid, dynamic remodeling.[7-10] This active remodeling of the biointerface is a critical feature of natural ECM, and the design of next-generation biomaterials must account for the dynamic aspects of these interfaces. The need for substrates that can dynamically regulate biological functions such as cell adhesion, proliferation, and differentiation has recently led to a variety of "smart material" designs in which control of biomaterial properties is stimulated by changes in temperature or pH or via light-induced or electrochemical modifications.[11-23] Herein, we report studies on a new class of smart materials—low-density self-assembled monolayers, or LDSAMs—which can undergo reversible conformational transitions that dynamically change the macroscopic surface properties of the monolayers.[23,24] Unlike traditional self-assembled monolayers (SAMs), which assemble in tightly packed arrangements, LDSAMs show increased conformational freedom of their constituent alkanethiolate molecules, which allows

LDSAMs to exhibit unique, reversible responsiveness to the application of electrical potential.[23]

Although a range of surface analysis methods are available for characterization of switchable surfaces—including infrared spectroscopy, X-ray photoelectron spectroscopy (XPS), surface plasmon spectroscopy, ellipsometry, sum frequency generation spectroscopy, and cyclic voltammetry (CV)—electrochemical impedance spectroscopy (EIS) has become an increasingly important tool for SAM analysis. This trend is seen mainly because of the precise surface-sensitive analytical information that electrochemical methods provide and because of the small (~10 mV) sinusoidal probe voltages that are used in EIS, which make it a less perturbing method than CV.

Studies of the electrical properties of SAMs by EIS can be divided into those that examine electronic conduction through SAMs using redox-active probes and those that follow the ionic conduction through SAMs using solution ions in the absence of redox probes. The majority of the EIS studies on SAMs reported in the literature have been conducted using redox probes, which has enabled studies of a variety of important characteristics of SAMs.[25-36] For instance, studies have examined the growth properties of dodecaneselenol,[26] octadecanethiol,[27] and naphthalene disulfide[28] monolayers, determining the relative times scales for monolayer adsorption and reorganization/crystallization; electron-transfer kinetics have been examined for dodecanethiol[29] and 4'-hydroxy-4-mercaptobiphenyl[30,31] monolayers; and monolayer pinhole size and separation have been studied for octadecanethiol monolayers.[32] Redox probe studies have also examined the passivation of a gold surface by 2-mercapto-3-*n*-

octylthiophene,[33] the fractional coverage of octadecanethiol molecules,[34] and the change in the electrical "apparent thickness" of alkanethiol monolayers.[35]

In solutions without redox couples, ionic permeability through the monolayers plays the dominant role in the conduction of current. This phenomenon has been used to study acid-base reactions for mercaptohexadecanoic acid (MHA) and mercaptododecylamine monolayers,[37] the ionic insulating properties of alkanethiol monolayers of different chain lengths,[38,39] the effect of applied potential on alkanethiol monolayer structure,40 the potential-induced desorption of monolayers,[41] and the insulating properties of adsorbed protein layers on alkanethiol monolayers.[42] The studies of Boubour and Lennox[39-41] in particular have presented a number of observations that suggest the usefulness of redox-inactive EIS for studying ionic permeability of low-density monolayers. First, well-packed SAMs, which exhibit strong barriers to ionic penetration, typically display low frequency (1 Hz < f < 1000 Hz) phase angles approaching 90° (the theoretical phase angle for an ideal capacitor). In contrast, SAMs that display low-frequency phase angles below 87° show current leakage at pinholes and grain boundaries. Second, only in the medium-to-high-frequency range (100 Hz and up) does a change in electrolyte composition (e.g., salt concentration) affect the impedance trace. Third, upon the application of DC potential greater than a certain critical potential, the monolayer structure is perturbed and ionic permeability increases significantly, as long as potential-induced desorption can be excluded.

Despite the usefulness of redox probes for the determination of monolayer properties, practical concerns, particularly when pursuing biological or biomedical applications, will require far different environments from those seen in a typical

electrochemical cell containing soluble hexaferrocyanide/hexaferricyanide. For this reason, the EIS measurements taken during these studies were performed in phosphate-buffered saline (PBS), an inert, redox-inactive, and physiologically relevant electrolyte solution. Our findings show that this analytical setup can be used to make accurate distinctions between different SAM types that are structurally very similar, and the aforementioned studies also provide a precedent for the study of purely ionic conductance through SAMs in the absence of redox couples.[39-41]

Although the physicochemical properties of a range of different SAMs have been studied extensively,[25,43-46] these studies have been limited to traditional dense SAMs, which do not exhibit tunable responsiveness to dynamic stimuli. Here we extend this method to LDSAMs assembled on gold and silver.

Experimental Section

Materials

MHA, mercaptoundecanoic acid (MUA), hexadecanethiol (HDT), undecanethiol (UDT), dimethoxytrityl chloride (DMT-Cl), triethylamine (TEA), diisopropylethylamine (DIPEA), absolute ethanol, and PBS were purchased from Sigma Aldrich (St. Louis, MO). Chlorotrityl chloride (CT-Cl) was purchased from TCI America (Portland, OR). Chemicals were used as received. Deionized water was produced using a Barnstead International (Dubuque, IA) E-pure system. Prime grade silicon wafers were purchased from Silicon Valley Microelectronics (Santa Clara, CA). Gold, silver, and titanium (99.99+%) were purchased from Alfa Aesar (Ward Hill, MA).

Synthesis of 16-chlorotrityl-mercaptohexadecanoic Acid (CT-MHA) and 16-chlorotrityl-mercaptoundecanoic Acid (CT-MUA)

The synthesis of 16-chlorotrityl-mercaptohexadecanoic acid (CT-MHA) has been reported previously.[23] The synthesis of 16-chlorotrityl-mercaptoundecanoic acid (CT-MUA) was performed using a protocol that was similar to that of CT-MHA. The first step involves protection of the thiol tail of MUA with a dimethoxytrityl (DMT) group to form the thioether MUA-DMT. Next, 1.09 g of MUA was reacted with 1.76 g of DMT-Cl and 0.84 mL of triethylamine in 50 mL of 5:4:1 tetrahydrofuran/acetic acid/water, at room temperature, under argon atmosphere, for 14 h. MUA-DMT was isolated and purified by silica column chromatography (3:1:1 hexane/ethyl ether/THF) yielding 1.3 g of a yellow/amber oil product. The second step involves protection of the carboxyl headgroup of MUA-DMT with a chlorotrityl (CT) group to form the ester/thioether CT-MUA-DMT. Next, 1.3 g of purified MUA-DMT was reacted with 0.91 g of CT-Cl and 0.91 mL of DIPEA in 50 mL methylene chloride at room temperature under argon atmosphere for 14 h. CT-MUA-DMT was isolated and purified by silica column chromatography (3:1 hexane/ethyl ether) yielding 0.68 g of a clear oil product. The third step involves deprotection of the DMT group from the thiol tail of MUA to form the ester CT-MUA. Purified CT-MUA-DMT (0.68 g) was dissolved in 20 mL of 3:1 THF/methanol and 2 mL of 1 M sodium acetate to which was added a solution of 340 mg of silver nitrate in 4 mL of 5:1 methanol/water. The mixture was stirred for 1 h at room temperature. Precipitate was removed by centrifugation at 4000*g* for 5 min, followed by resuspension of the pellet in 15 mL of 3:1 THF/methanol, recentrifugation at 4000*g* for 5 min, and combination of the two supernatants. A solution of 308 g of dithioerythritol (DTE) in 3 mL of 1 M sodium acetate was then added, and the mixture was stirred for 5 h at room temperature.

Precipitate was removed by centrifugation at 4000*g* for 5 min, followed by resuspension of the pellet in 15 mL of 3:1 THF/methanol, recentrifugation at 4000*g* for 5 min, and combination of the two supernatants. CT-MUA was isolated and purified by silica column chromatography (50 mL of 3:1 hexane/ethyl ether, followed by 1:1 hexane/ethyl ether), yielding 0.22 g of a clear oil product. CT-MUA (and CT-MHA) was aliquoted and stored at -20 °C until used. [MUA-DMT] ^{1}H NMR (300 MHz, $CDCl_3$) δ 1.17-1.39 (m), 1.57-1.69 (m), 1.81-1.88 (m), 2.12-2.17 (t), 2.31-2.38 (t); 2.67-2.72 (t), 3.79 (s), 6.78-6.85 (m), 7.15-7.40 (m); ^{13}C NMR (100 MHz, $CDCl_3$) δ 29.25, 29.40, 55.44, 113.23, 113.40, 127.99, 128.09, 129.08, 129.36, 129.64, 130.90, 132.35. [CT-MUA-DMT] ^{1}H NMR (300 MHz, $CDCl_3$) δ 1.17-1.29 (m), 1.62-1.69 (m), 1.79-1.88 (m) 2.12-2.17 (t), 2.31-2.37 (m), 2.66-2.71 (t) 3.34 (s), 3.74-3.80 (m), 3.90 (s), 3.95-3.99 (m) 6.69-6.85 (m) 6.94-6.99 (m) 7.08-7.60 (m) 7.74-7.86 (m); ^{13}C NMR (75 MHz, $CDCl_3$) δ 24.92, 25.83, 28.67, 29.18, 29.38, 29.55, 34.20, 39.52, 55.45, 55.74, 55.99, 68.19, 82.82, 113.25, 113.39, 113.80, 115.01, 116.24, 126.63, 127.61, 127.98, 128.23, 128.43, 129.34, 129.65, 129.99, 130.90, 131.58, 131.72, 132.16, 132.84, 137.77, 143.93, 145.75, 179.63. [CT-MUA] ^{1}H NMR (300 MHz, $CDCl_3$) δ 1.10-1.35 (m), 1.56-1.68 (m), 1.95-2.00 (t), 2.31-2.36 (t), 7.17-7.35 (m), 7.43-7.46 (m); ^{13}C NMR (75 MHz, $CDCl_3$) δ 24.92, 25.83, 28.67, 29.18, 29.38, 29.55, 34.20, 39.52, 52.68, 55.45, 55.74, 55.99, 68.19, 82.82, 113.25, 113.39, 113.80, 115.006, 116.243, 126.632, 127.611, 127.98, 128.23, 128.43, 129.34, 129.65, 129.99, 130.90, 131.58, 131.72, 132.16, 132.84, 137.77, 143.93, 145.75, 179.63. Electrospray mass spectrometry gave a mass-to-charge ratio of 517.1948 for the CT-MUA [M + Na]+ adduct, consistent with a theoretical molar mass of 517.1944 g/mol calculated for the nondimerized product.

Substrate and SAM Preparation

Substrates were prepared using prime grade silicon wafers upon which were deposited a 4500 Å SiO_2 insulating layer, a 100 Å titanium adhesive layer, and a 1000 Å gold or silver outer layer. Photolithographic techniques were used to produce patterned devices with a defined 2.2 cm^2 surface area for monolayer assembly and a separate electrical contacting patch; these patterned devices were used for electrochemical impedance spectroscopy measurements, the results of which scale with surface area. Surface roughness of the substrates was <2 nm rms by atomic force microscopy. Substrates were rinsed with a sequence of absolute ethanol, deionized water, and absolute ethanol, then dried under a stream of N_2 prior to SAM preparation. SAMs were prepared by immersion of the target region of the substrates in 1 mM ethanolic solutions of adsorbate for 48 h at room temperature. After incubation, samples were rinsed with a sequence of absolute ethanol, deionized water, and absolute ethanol, then dried under a stream of N_2. LDSAMs were prepared by incubation of CT-MHA or CT-MUA monolayer samples in 50% trifluoroacetic acid in ethanol for 2 min, which results in cleavage of the acid-labile ester bonds between the chlorotrityl groups and the immobilized alkanethiolates. Following cleavage, the samples were rinsed with a sequence of absolute ethanol, deionized water, and absolute ethanol, then dried in a stream of N_2.

Instrumentation: EIS and FTIR Spectroscopy

EIS was performed using a standard three-electrode electrochemical cell (SAM sample as working electrode, saturated standard calomel electrode [SCE] as reference electrode, and platinum mesh as counter electrode) with N_2-purged PBS as electrolyte

solution. A Gamry PCI4/300 potentiostat with EIS300 software module was used to take EIS measurements. The applied potential had an AC amplitude of 10 mV rms and a frequency range from 1 to 105 Hz, with DC bias potentials varying between 0 and +400 mV with respect to (wrt) SCE. The amplitude and phase angle of the current response were recorded at 10 points per decade in frequency. Fourier transform infrared (FTIR) spectroscopy was performed using a liquid-nitrogen-cooled Thermo Nicolet 6700 spectrometer in 85° grazing angle mode with a 16 mm aperture. One hundred twenty eight scans were taken per sample at 4 cm^{-1} resolution.

Results and Discussion

Self-Assembly

In this study, LDSAMs of MHA and MUA prepared on gold and silver electrodes are compared to their traditional dense SAM analogues. Figure 2.1 outlines the direct self-assembly method for preparing regular SAMs of MHA and MUA, as well as the indirect assembly method for preparing LDSAMs. The indirect method was designed to circumvent the tendency of alkanethiolates to form tightly packed assemblies resembling two-dimensional crystals.[25,43,45] The approach involves a multistep process of conjugating MHA or MUA to bulky, space-filling CT groups to form CT-MHA or CT-MUA esters. The subsequent assembly of CT-MHA or CT-MUA monolayers on gold or silver is followed by cleavage of the bulky CT groups, resulting in LDSAMs of MHA and MUA that are chemically identical to regular SAMs, but differ from the latter in the molecular spacing between the chains. Analysis of the CT-MHA and CT-MUA esters by NMR, mass spectrometry, and FTIR showed agreement of the thiols with the anticipated

structures, verified the absence of disulfide dimers, and demonstrated the esters' stability for several months, when stored under inert gas at -20 °C.

Electrochemical Impedance Spectroscopy

Figure 2.2 shows EIS Nyquist plots acquired in PBS buffer (pH 7.4) at 0 mV DC (wrt SCE) for various types of monolayers on gold and silver. When we compare different types of monolayers with the same chain length and on the same substrate, we notice that the highest impedances are seen with the dense CH_3-terminated SAMs (HDT and UDT) followed by the CT-terminated SAMs (CT-MHA and CT-MUA), then the dense COOH-terminated SAMs (MHA and MUA), and finally the LDSAMs (LDMHA and LDMUA). As expected, hydrophobic headgroups and higher packing densities result in greater ionic barrier properties. The greater impedance of the CT-terminated SAMs compared to MHA/MUA can be attributed to the dense packing of the large, hydrophobic CT groups on the surface. Although the impedance of the LDSAMs is low relative to the other monolayers, it is significantly higher than that of bare gold or silver; the impedance modulus at 1 Hz (maximum *y*-axis value) of bare gold and silver is on the order of 1000-2000 Ω (too low to be clearly plotted in Figure 2.2), which is significantly lower than the most permeable LDSAM of LDMUA on Ag, which has a modulus of 7500 Ω at 1 Hz. This observation suggests the relative homogeneity and continuity of the LDSAMs, with a lack of gross levels of pinhole defects. When we compare the impedance of monolayers with different chain lengths (Figure 2.2a vs 2.2b), we typically see higher impedances for the C16-length SAMs than for the corresponding C11-length monolayers. This observation is expected because of the greater resistance to ionic permeation that monolayers with longer chain lengths display.[39] Similarly, monolayers assembled on gold

typically showed higher impedances than monolayers assembled on silver (Figure 2.2a vs 2.2c). Also noticeable in the Nyquist plots of SAMs on silver are some deviations from linearity in the slope of the data; greater phase angle deviations are seen for the data taken at lower frequencies (closer to the origin). Since solution resistance is the dominant source of impedance at low frequencies, this effect could result from oxidation at the surface of the silver due to trace levels of dissolved oxygen in the PBS solution.

Impedance Switching

The next series of EIS analyses examined the effect of the applied DC potential on monolayer impedances. During these experiments, a series of increasingly positive DC electrical potentials was applied during EIS measurements. Because our LDSAMs have enhanced conformational freedom,[23] we would anticipate the application of positive potential to more easily influence the structure of the monolayers and thus alter their impedance profiles to a greater degree compared to the more sterically hindered dense SAMs. Nyquist plots of the potential responses of SAMs on gold are shown in Figure 2.3. The measurements for each type of monolayer were performed consecutively, in order of increasing positive potential, without removing the sample from the electrochemical cell during the experiments. An electrochemical potential of +400 mV wrt SCE was chosen as the upper potential limit to avoid electrochemical oxidation of the thiol or potential-induced monolayer defects.[40] In the case of both (a) the C16- and (b) the C11-length monolayers, the impedance of dense SAMs does not change significantly upon application of potentials up to +400 mV, while the impedance of the LDSAMs decreases stepwise with increasing positive potential, culminating in a decrease in impedance modulus (*y*-axis value) of about 30% for LDMHA at +400 mV and about 50% for

LDMUA at +100 mV. LDSAMs of MUA thus showed greater sensitivity to the application of the electrochemical potential than LDSAMs of MHA. These data are in agreement with an increased flexibility of the shorter chain LDSAMs. The increase of phase angle (trace tilt) seen for LDSAMs at higher potentials also indicates increasingly greater deviations from ideal capacitor behavior and increasing ionic permeability as a result of the conformational transitions induced by the applied potential. The potential responses of SAMs on silver are shown in Figure 2.4. In this case, +40 mV wrt SCE was chosen as an upper potential limit because of the increased potential sensitivity of the SAMs on silver (gross deformation of the impedance traces are seen at +60 mV, data not shown). Although the potential response trends were similar to those of SAMs on gold, some differences are apparent. The dense SAMs appear to be somewhat more sensitive to potential than the corresponding monolayers on gold. The effect of applied potential on LDMUA is also relatively small, possibly because of the shorter chain length of this monolayer. The very high level of conformational flexibility that results from this structure may obscure the effect of actively induced conformational transitions. The results from Figures 2.3 and 2.4 generally suggest that the impedance of LDSAMs, unlike that of dense SAMs, can be controlled or tuned across a relatively wide range through the application of small electrical potentials. After demonstrating the tunability of LDSAMs, we conducted a series of EIS experiments to test the reversibility of the electrical impedance response of LDSAMs—a property which could be useful for technological applications. Previous studies have demonstrated the reversible switching of LDSAMs on gold, conferring dynamic control over surface properties such as wettability.[23] The present experiments address reversible switching of the DC bias potential during EIS

analysis between 0 and +400 mV wrt SCE for all Au monolayers (except LDMUA, for which it was between 0 and +100 mV). In contrast, the DC bias potential was switched between 0 and +40 mV wrt SCE for all Ag monolayers. The concurrent EIS analysis provides an assessment of reversible control over ionic conduction through the monolayer. Figure 2.5 shows the resulting pattern of impedance moduli and phase angles at 1 Hz from the series of experiments on Au SAMs. Toggling the potential through four switching cycles has the least effect on dense MHA SAMs, whereas MUA SAMs show only a slight response. LDMHAs show a pronounced response, and LDMUAs exhibit the strongest response. The effect is generally similar for impedance modulus and phase angle, although interestingly, with MUA we see a slight inversion effect where the phase angle is marginally higher at +400 mV. The greater responsiveness of the C11 SAMs and the LDSAMs is consistent with our previous observations of the effect of monolayer chain length and density on impedance. Reversibility is very good, with little drift seen in impedance levels over the course of the measurement sequence. Figure 2.6 shows the resulting pattern of impedance moduli and phase angles at 1Hz from the series of experiments on Ag SAMs. Here we see increased potential sensitivity to smaller applied fields but also less dramatic contrast between dense SAMs and LDSAMs. The data show excellent reversibility, again with very little drift of the impedance levels over the course of the experiment. The data shown in Figures 2.5 and 2.6 suggest that conformational flexibility is essential to producing monolayer systems with reversible impedance properties. Although the flexibility conferred by the Ag lattice is clearly sufficient to yield reversibility trends, more distinctly contrasting effects are seen on Au, when comparing LDSAMs with dense SAMs.

Fourier Transform Infrared Spectroscopy

Grazing angle FTIR spectra were recorded for dense SAMs and LDSAMs before and after the EIS reversibility cycling experiments in order to assess the effect of EIS on monolayer integrity and stability. Spectra for Au monolayers are shown in Figure 2.7, spectra for Ag monolayers are shown in Figure 2.8, and characteristic peak locations are listed in Table 2.1. Dense monolayers have characteristic asymmetric and symmetric methylene CH_2 stretches at ~2920 and ~2850 cm^{-1}, as well as C=O stretches at ~1720 cm^{-1}. Chlorotrityl-terminated monolayers show additional peaks at ~3060 and ~3030 cm^{-1} (asymmetric and symmetric aromatic C-H stretch) and ~1150 cm^{-1} (C-Cl stretch), as well as a shift of the C=O stretch from ~1720 to ~1740 cm^{-1} due to the ester bond. Details of the FTIR studies are given in Table 2.1. After CT group cleavage, LDSAMs show an absence of the previously present aromatic and C-Cl stretches, a C=O shift to the ~1720 cm^{-1} carbonyl range, and generally minimal shifts in CH_2 stretches, with the exception of LDSAMs of MUA on Ag. LDSAMs show a red-shift in their CH_2 stretches compared to dense MHA and MUA monolayers. This shift reflects the more fluid and less crystalline environment experienced by the methylene groups within low-density monolayers and is also the reason Ag monolayers show a greater red-shift than Au monolayers. With the exception of a slight shift in the asymmetric CH_2 stretch for LDSAMs of MUA on Ag, there is no difference between the spectra recorded before and after impedance switching. The data generally suggest that the repeated application of small electrical potentials does not affect the integrity of LDSAMs.

Conclusions

Low-density monolayers of MHA can be prepared via self-assembly of bulky precursor thiols and subsequent cleavage of the spacer.[23] Compared to their dense counterparts, these monolayers show enhanced responsiveness to the application of even small electrical potentials.[23] Although previous studies have focused on LDSAMs assembled on gold,[23] we have now extended this concept to shorter thiols (MUA) self-assembled on gold and to LDSAMs of MHA and MUA on silver substrates. Moreover, we have demonstrated that the application of small electrical potentials can induce switching of the electrochemical barrier properties of these monolayers. EIS conducted in PBS buffer at physiological pH values has proven to be an exquisite method for studying reversible transitions in low-density monolayers. Moreover, the switching of the four LDSAMs (MHA and MUA on Au and Ag) was found to be in clear contrast to the regular SAMs of MHA and MUA that were included in this study as references. In fact, the stepwise application of electrochemical potentials between 0 and +400 mV wrt SCE for Au and between 0 and +40 mV wrt SCE for Ag enabled a fine-tuning of the impedance of LDSAMs. The potential-induced changes in impedance were found to be reversible, as demonstrated by the repeated switching of LDSAMs of MHA and MUA on both gold and silver electrodes. The stability of the LDSAMs during the impedance switching was verified by comparing the grazing angle FTIR spectra of the LDSAMs before and after impedance switching. Within the margins of error, these spectra were identical. LDSAMs show an interesting responsiveness to the application of small electrical potentials. The demonstrated ability to tune and switch their impedance properties may be useful when considering their potential for biosensors or active

biointerfaces for cell-based studies. Significant future work is needed, however, before these applications become a reality.

Acknowledgment

We thank Hsien-Yeh Chen, Onnop Srivannavit, Brian Johnson, and Kenneth Chomistek for help with electrode microfabrication. D.K.P. acknowledges support from a graduate fellowship from the National Institutes of Health through the University of Michigan Cellular Biotechnology Training Program. The project was funded by grants from the National Institutes of Health and an Idea Award of the Department of Defense.

Figures

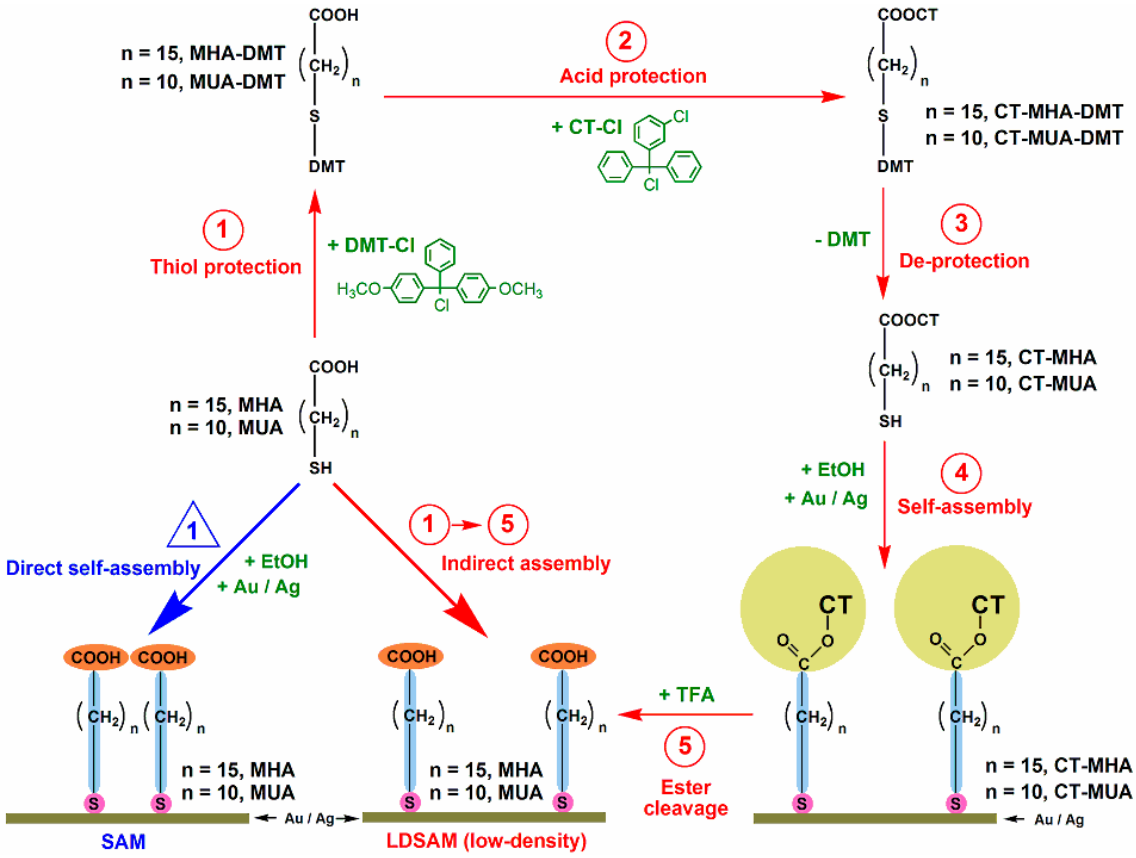

Figure 2.1. Preparation methods for traditional SAMs and LDSAMs. The formation of LDSAMs involves an indirect strategy via the CT ester.

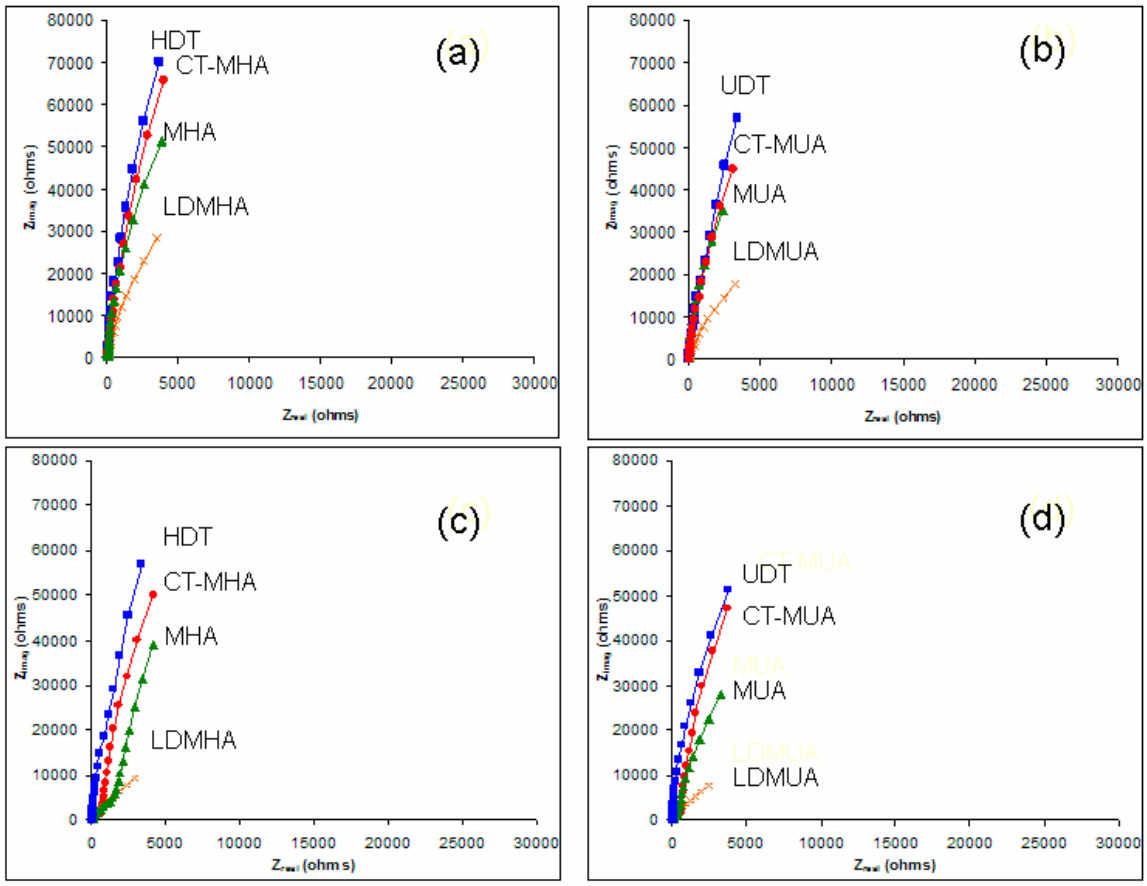

Figure 2.2. EIS Nyquist plots comparing different monolayer types. (a) C16 SAMs on Au, (b) C11 SAMs on Au, (c) C16 SAMs on Ag, (d) C11 SAMs on Ag.

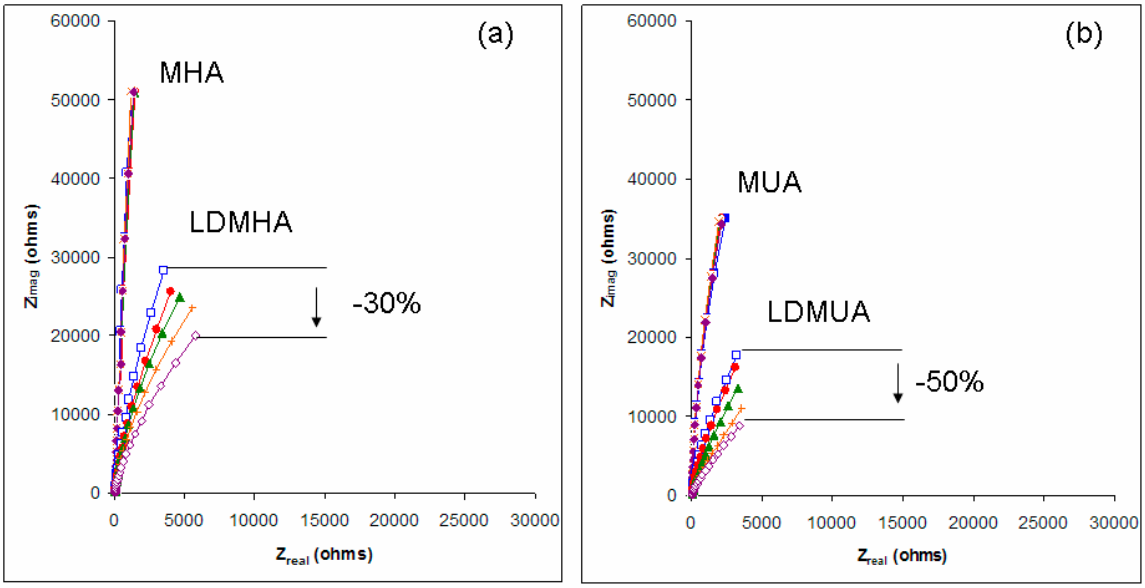

Figure 2.3. Impedance response of monolayers on Au to a stepwise change in electrical potential between 0 and +400 mV wrt SCE. (a) C16 monolayers and (b) C11 monolayers.

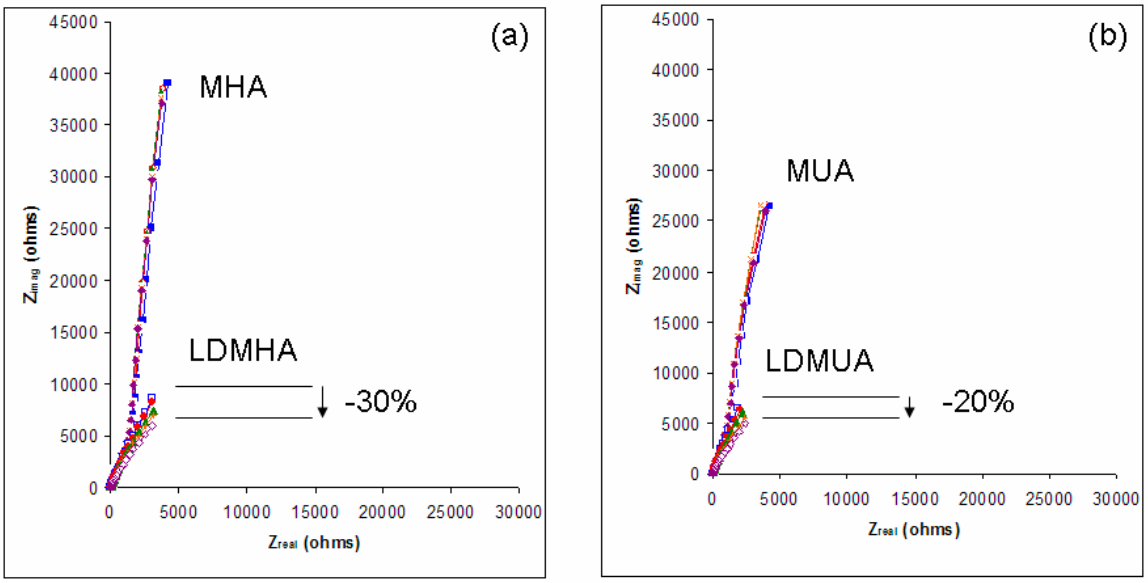

Figure 2.4. Impedance response of monolayers on Ag to a stepwise change in electrical potential between 0 and +40 mV wrt SCE. (a) C16 monolayers and (b) C11 monolayers.

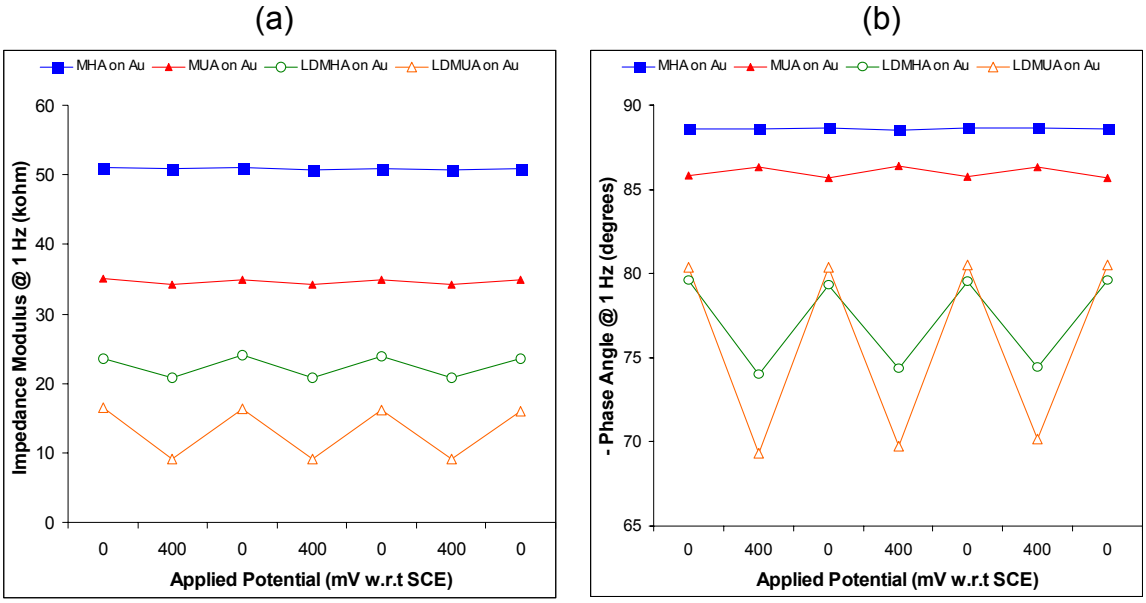

Figure 2.5. Reversibility of the impedance response for potential switching between 0 and +400 mV wrt SCE for monolayers on Au. (a) Impedance modulus vs. applied potential and (b) phase angle vs. applied potential.

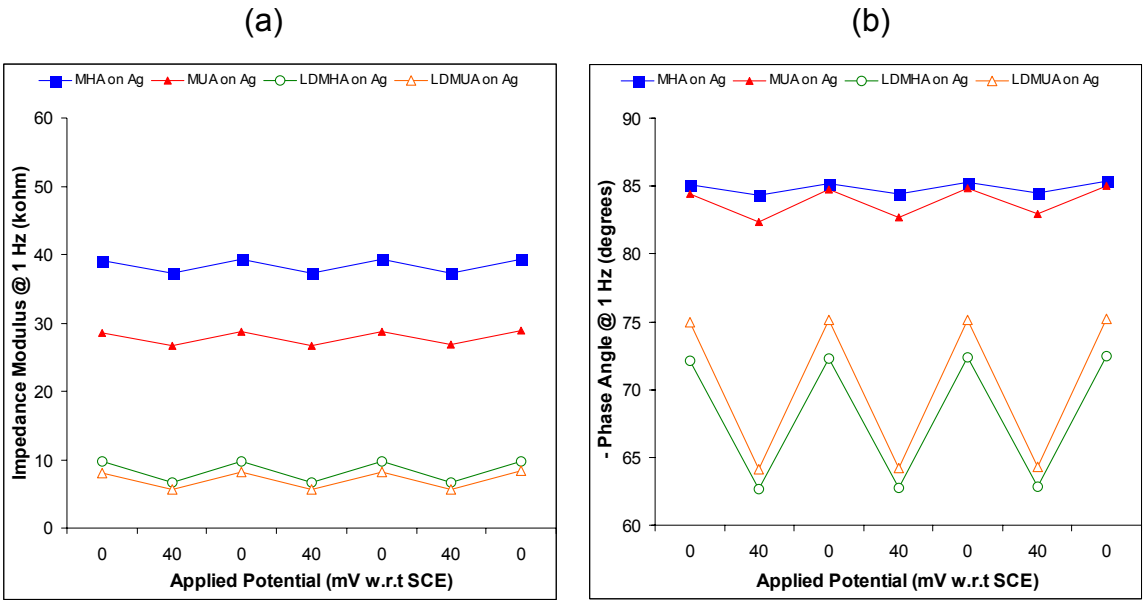

Figure 2.6. Reversibility of the impedance response for potential switching between 0 and +40 mV wrt SCE for monolayers on Ag. (a) Impedance modulus vs. applied potential and (b) phase angle vs. applied potential.

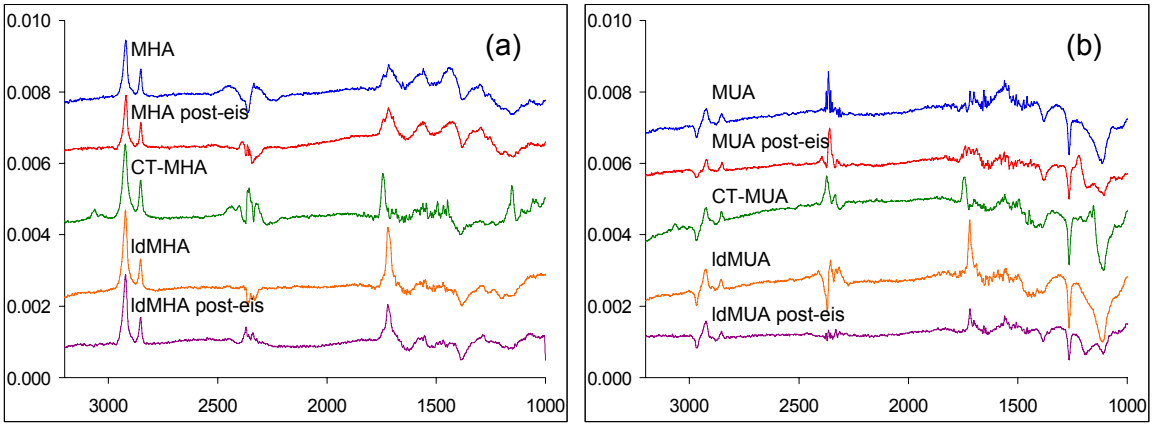

Figure 2.7. FTIR spectra of monolayers on Au. (a) C16 monolayers and (b) C11 monolayers.

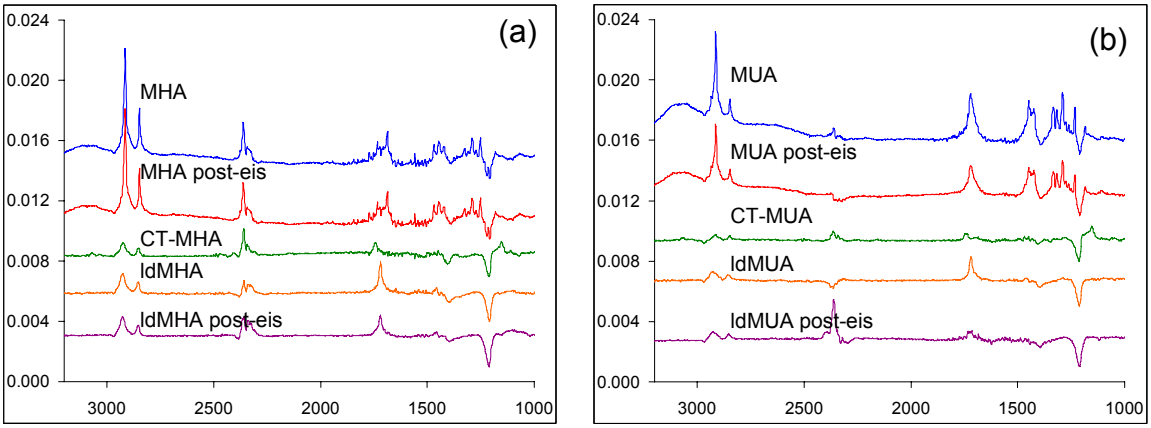

Figure 2.8. FTIR spectra of monolayers on Ag. (a) C16 monolayers and (b) C11 monolayers.

Table

Monolayer	Substrate	asym C-H	sym C-H	asym CH_2	sym CH_2	C=O, Carbonyl	C=O, Ester	C-Cl
MHA	Au	-	-	2919.6	2850.9	1716.2	-	-
MHA post-EIS	Au	-	-	2919.0	2850.5	1717.7	-	-
CT-MHA	Au	3063.2	3032.6	2921.9	2851.6	-	1743.5	1153.1
LDMHA	Au	-	-	2921.3	2852.0	1720.0	-	-
LDMHA post-EIS	Au	-	-	2920.8	2851.5	1720.1	-	-

Monolayer	Substrate	asym C-H	C-H	assym CH_2	sym CH_2	C=O, Carbonyl	C=O, Ester	C-Cl
MUA	Au	-	-	2922.4	2851.0	1717.5	-	-
MUA post-EIS	Au	-	-	2921.8	2850.2	1718.1	-	-
CT-MUA	Au	3066.37	3028.8	2922.9	2853.2	-	1743.0	1154.6
LDMUA	Au	-	-	2925.3	2855.3	1718.6	-	-
LDMUA post-EIS	Au	-	-	2923.1	2852.1	1717.8	-	-

Monolayer	Substrate	asym C-H	C-H	assym CH_2	sym CH_2	C=O, Carbonyl	C=O, Ester	C-Cl
MHA	Ag	-	-	2913.9	2846.6	1687.8	-	-
MHA post-EIS	Ag	-	-	2914.3	2847.2	1686.2	-	-
CT-MHA	Ag	3067.8	3035.7	2923.2	2851.0	-	1741.8	1154.2
LDMHA	Ag	-	-	2925.1	2853.4	1718.4	-	-
LDMHA post-EIS	Ag	-	-	2926.7	2853.7	1720.2	-	-

Monolayer	Substrate	asym C-H	C-H	assym CH_2	sym CH_2	C=O, Carbonyl	C=O, Ester	C-Cl
MUA	Ag	-	-	2913.4	2846.3	1720.7	-	-
MUA post-EIS	Ag	-	-	2913.3	2846.2	1720.6	-	-
CT-MUA	Ag	3066.1	3025.8	2915.0	2847.9	-	1745.7	1153.0
LDMUA	Ag	-	-	2923.9	2854.8	1718.6	-	-
LDMUA post-EIS	Ag	-	-	2928.9	2853.5	1720.8	-	-

Table 2.1. FTIR Peak Locations for Monolayers Assembled on Au and Ag.

References

(1) Stevens, M. M.; George, J. H. *Science* **2005**, *310*, 1135-1138.

(2) Lutolf, M. P.; Hubbell, J. A. *Nat. Biotechnol.* **2005**, *23*, 47-55.

(3) Vogel, V.; Baneyx, G. *Annu. Rev. Biomed. Eng.* **2003**, *5*, 441-63.

(4) Mrksich, M. *Curr. Opin. Chem. Biol.* **2002**, *6*, 794-797.

(5) Lahann, J.; Langer, R. *MRS Bull.* **2005**, *30*, 185-188.

(6) Stupp, S. I.; Donners, J. J. J. M.; Li, L. S.; Mata. A. *MRS Bull.* **2005**, *30*, 864-873.

(7) Holmbeck, K.; Szabova, L. *Birth Defects Res. C Embryo Today* **2006**, *78*, 11-23.

(8) Midwood, K. S.; Williams, L. V.; Schwarzbauer, J. E. *Int. J. Biochem. Cell Biol.* **2004**, *36*, 1031-1037.

(9) Brown, L. *Am. J. Physiol. Heart Circ. Physiol.* **2005**, *289*, H973-974.

(10) Davis, G. E.; Senger, D. R. *Circ. Res.* **2005**, *97*, 1093-1107.

(11) de las Heras Alarcon C.; Pennadam, S.; Alexander, C. *Chem Soc. Rev.* **2005**, *34*, 276-285.

(12) Kikuchi, A.; Okano, T. *J. Controlled Release* **2005**, *101*, 69-84.

(13) Tsuda, Y.; Kikuchi, A.; Yamato, M.; Sakurai, Y.; Umezu, M.; Okano, T. *J. Biomed. Mater. Res. A* **2004**, *69*, 70-78.

(14) Riskin, M.; Basnar, B.; Chegel, V. I.; Katz, E.; Willner, I.; Shi, F.; Zhang, X. *J. Am. Chem. Soc.* **2006**, *128*, 1253-1260.

(15) Wang, X.; Kharitonov, A.; Katz, E.; Willner, I. *Chem. Commun.* **2003**, *9*, 1542-1543.

(16) Jeong, B.; Gutowska, A. *Trends Biotechnol.* **2002**, *20*, 305-311.

(17) Russell, T. P. *Science* **2002**, *297*, 964-967.

(18) Liu, Y.; Mu, L.; Liu, B. H.; Zhang, S.; Yang, P. Y.; Kong, J. L. *Chem. Commun.* **2004,** *10*, 1194-1195.

(19) Abbott, S.; Ralston, J.; Reynolds, G.; Hayes, R. *Langmuir* **1999**, *15*, 8923-8928.

(20) Ichimura, K.; Oh, S. K.; Nakagawa, M. *Science* **2000**, *288*, 1624-1626.

(21) Abbott, N. L.; Gorman, C. B.; Whitesides, G. M. *Langmuir* **1995**, *11*, 16-18.

(22) Chi, Y. S.; Lee J. K.; Lee, S. G.; Choi, I. S. *Langmuir* **2004**, *20*, 3024-3027.

(23) Lahann, J.; Mitragotri, S.; Tran, T. N.; Kaido, H.; Sundaram, J.; Choi, I. S.; Hoffer, S.; Somorjai, G. A.; Langer, R. *Science* **2003**, *299*, 371-373.

(24) Katz, E.; Lioubashevsky, O.; Willner, I. *J. Am. Chem. Soc.* **2004**, *126*, 15520-15532.

(25) Love, J. C.; Estroff, L. A.; Kriebel, J. K.; Nuzzo. R. G.; Whitesides G.

M. *Chem. Rev.* **2005**, *105*, 1103-1169.

(26) Protsailo, L. V.; Fawcett, W. R.; Russell, D.; Meyer, R. L. *Langmuir* **2002**, *18*, 9342-9349.

(27) Diao, P.; Jiang, D.; Cui, X.; Gu, D.; Tong, R.; Zhong, B. *J. Electroanal. Chem.* **1999**, *464*, 61-67.

(28) Bandyopadhyay, K.; Vijayamohanan, K.; Shekhawat, G. S.; Gupta, R. P. *J. Electroanal. Chem.* **1998**, 447, *1*, 11-16.

(29) Xing, Y. F.; O'Shea, S. J.; Li, S. F. Y. *J. Electroanal. Chem.* **2003**, *542*, 7-11.

(30) Janek, R. P.; Fawcett, W. R.; Ulman, A. *Langmuir* **1998**, *14*, 3011-3018.

(31) Janek, R. P.; Fawcett, W. R.; Ulman, A. *J. Phys. Chem. B* **1997,** *101*, 8550-8558.

(32) Diao, P.; Guo, M.; Tong, R. *J. Electroanal. Chem.* **2001**, *495*, 98-105.

(33) Peng, Z.; Dong, S. *Langmuir* **2001**, *17*, 4904-4909.

(34) Diao, P.; Guo, M.; Jiang, D.; Jia, Z.; Cui, X.; Gu, D.; Tong, R.; Zhong, B. *J. Electroanal. Chem.* **2000**, *480*, 59-63.

(35) Cui, X.; Jiang, D.; Diao, P.; Li, J.; Tong, R.; Wang, X. *J. Electroanal. Chem.* **1999**, *470*, 1, 9-13.

(36) Widrig, C. A.; Chung, C.; Porter, M. D. *J. Electroanal. Chem.* **1991**, *310*, 335-359.

(37) Schweiss, R.; Werner, C.; Knoll, W. *J. Electroanal. Chem.* **2003**, *540*, 145-151.

(38) Protsailo, L. V.; Fawcett, W. R. *Langmuir* **2002**, *18*, 8933-8941.

(39) Boubour, E.; Lennox, R. B. *Langmuir* **2000**, *16*, 4222-4228.

(40) Boubour, E.; Lennox, R. B. *J. Phys. Chem. B* **2000**, *104*, 9004-9010.

(41) Boubour, E.; Lennox, R. B. *Langmuir* **2000**, *16*, 7464-7470.

(42) Bordi, F.; Prato, M.; Cavalleri, O.; Cametti, C.; Canepa, M.; Gliozzi, A. *J. Phys. Chem. B* **2004**, *108*, 20263-20272.

(43) Schreiber, F. *J. Phys.: Condens. Matter* **2004**, *16*, R881-R900.

(44) Schwartz, D. K. *Annu. Rev. Phys. Chem.* **2001**, *52*, 107-137.

(45) Ulman, A. *Chem. Rev.* **1996**, *96*, 1533-1554.

(46) Dubois, L. H. *Annu. Rev. Phys. Chem.* **1992**, *43*, 437-463.

CHAPTER 3

CHEMICAL, ELECTROCHEMICAL, AND STRUCTURAL STABILITY OF LOW-DENSITY SELF-ASSEMBLED MONOLAYERS

[This chapter has been adapted with minor modifications from the following published article: Peng, D.K.; Lahann, J. *Langmuir* **2007**, *23*, 10184-10189.]

Abstract

The stability of low-density self-assembled monolayers (LDSAMs) of mercaptohexadecanoic acid on gold is studied under a variety of storage conditions—air at room temperature, argon at room temperature and 4 °C, and ethanol at room temperature. The structural monotony of the low-density monolayers was assessed by monitoring the alkyl chains of LDSAMs by grazing-angle Fourier transform infrared spectroscopy as a function of time. Independently of the storage conditions, both symmetric and asymmetric methylene stretches at 2923 and 2852 cm^{-1} decreased after 4 weeks to 2919 and 2849 cm^{-1}, respectively. These data suggest an increased ordering of the alkyl chains that is distinctly different from that of conventional high-density monolayers of mercaptohexadecanoic acid included as a reference in this study. As a further extension of this observation, the electrochemical barrier properties of the low-density monolayers were assessed by electrochemical impedance spectroscopy and did not change significantly for any of the storage conditions over a period of 4 weeks. Moreover, X-ray photoelectron spectroscopy was used to assess the chemical changes in

the low-density monolayers over time. The chemical composition was essentially unaltered for all storage conditions. Specifically, oxidation of the sulfur headgroup, a common cause of monolayer degradation, was excluded for all test conditions on the basis of XPS analysis. This study confirms excellent storage stability for low-density monolayers under commonly used storage conditions and bridges an important technological gap between these systems and conventional high-density systems.

Introduction

Self-assembled monolayers (SAMs) have been studied extensively because of the ease and flexibility with which they can produce a diverse range of functionalized surfaces.[1-4] Widely characterized SAM systems, such as alkanethiolate monolayers on gold, are typically formed through the spontaneous assembly of their constituent molecules into films with tightly packed, sterically constrained alkyl chains. Several previous studies examined the stability of high-density SAMs. For instance, Schoenfisch et al.[5] and Horn et al.[6] independently examined the stability of alkanethiolate SAMs in air, Flynn et al. investigated the stability of monolayers made of undecanethiol as well as tri(ethylene glycol)-terminated undecanethiol derivatives in biological media,[7] and Willey et al. examined the stability of dodecanethiolate SAMs in air and under the influence of UV light and found limited stability with time.[8]

More recently, low-density SAMs (LDSAMs), which are formed with increased inter-chain distances, have attracted increasing interest because they display enhanced conformational freedom paired with unique structural characteristics and functions.[9,10] Certain LDSAMs have also been employed as the structural basis of dynamically switchable surfaces.[11] For instance, carboxyl-terminated LDSAMs, such as

mercaptohexadecanoic acid monolayers, displayed reversible and controllable switching of surface properties, such as wettability[11] and impedance,[12] upon application of small electrical potentials.

The initial development of switchable LDSAMs has encouraged several related investigations in recent years. For example, the behavior of stimuli-responsive SAMs has been characterized by molecular dynamics simulation,[13] the effects of LDSAMs on protein adsorption[14] and surface friction[15] have been examined, and various LDSAM fabrication methods have been developed, including those employing cyclodextrin inclusion complexes,[14] multidentate chelating alkanethiols,[15] and cleavable fluorocarbons.[16] The promise of fundamental insights into dynamic surface transitions and the technological implications of stimuli-responsive materials have transformed this topic into an active area of research.[17-20]

Although LDSAMs are chemically similar to their high-density counterparts, their increased interstitial spacing may increase their propensity for oxidative degradation, phase segregation, and interfacial restructuring. Before practical applications of LDSAMs can be realized, the influence of extended storage on chemical, structural, and electrochemical stability must be fundamentally examined. Thus far, repeated potential-induced switching of carboxyl-terminated LDSAMs in aqueous solution was demonstrated only over several hours.[11] Longer-term stability under different conditions has not yet been assessed in detail and is the focus of this study.

Experimental Section

Materials

Mercaptohexadecanoic acid (MHA), dimethoxytrityl chloride, absolute ethanol, and phosphate-buffered saline (PBS) were purchased from Sigma-Aldrich (St. Louis, MO). Chlorotrityl chloride was purchased from TCI America (Portland, OR). Chemicals were used as received. Deionized water was produced using a Barnstead International (Dubuque, IA) E-pure system. Prime-grade silicon wafers were purchased from Silicon Valley Microelectronics (Santa Clara, CA). Gold and titanium (99.99+%) were purchased from Alfa Aesar (Ward Hill, MA).

Synthesis

As previously reported,[11] 16-chlorotrityl-mercaptohexadecanoic acid (CT-MHA) was synthesized using a three-step protocol involving thiol protection using a dimethoxytrityl group, followed by carboxyl protection using a chlorotrityl group and thiol deprotection to yield CT-MHA.

SAM Preparation

Gold-coated silicon substrates with titanium adhesion layers (100 nm Au, 10 nm Ti) were prepared as previously reported,[12] with a defined 2.2 cm^2 surface area for monolayer assembly and a separate electrical contacting patch for electrochemical measurements. SAMs were prepared by immersion of the target region of the substrates in 1 mM ethanol solutions of adsorbate for 48 h at room temperature. After incubation, samples were rinsed with a sequence of absolute ethanol, deionized water, and absolute ethanol and were dried in a stream of N_2. Low-density SAMs were prepared from the CT-MHA monolayers by incubation for 2 min in 50% trifluoroacetic acid in ethanol, which results in quantitative cleavage of the acid-labile ester bonds and yielded acid-terminated

alkanethiolate monolayers. Following cleavage, the samples were rinsed with a sequence of absolute ethanol, deionized water, and absolute ethanol and then dried in a stream of N_2. Three replicate samples were then stored under each of the following conditions: an air atmosphere at room temperature, an argon atmosphere at room temperature, an argon atmosphere at 4 °C, or a N_2-purged ethanol bath with an argon atmosphere. In each case (including the air atmosphere), samples were enclosed within a tightly sealed jar. Three replicate samples of high-density SAMs of MHA were also stored under the same conditions as the control samples.

Instrumentation

Electrochemical impedance spectroscopy (EIS) was performed using a standard three-electrode electrochemical cell (a SAM sample as the working electrode, a saturated standard calomel electrode [SCE] as the reference electrode, and a platinum mesh as the counter electrode) with N_2-purged phosphate-buffered saline as the electrolyte solution. A Gamry PCI4/300 potentiostat with an EIS300 software module was used to take EIS measurements. The applied potential had an ac amplitude of 10 mV rms and a frequency range from 1 to 105 Hz, with a dc bias of 0 mV with respect to the SCE. The amplitude and phase angle of the current response were recorded at 10 points per decade in frequency. X-ray photoelectron spectroscopy (XPS) was performed using an Axis Ultra (Kratos Analyticals, U.K.) instrument equipped with a monochromatized Al KR X-ray source. Electrons were collected with a pass energy of 20 keV for C 1s and 40 keV for S 2p spectra. Spectra were normalized with respect to aliphatic carbon at 285.0 eV, and components were modeled with a Marquardt fitting algorithm. Fourier transform infrared (FTIR) spectroscopy was performed using a liquid-nitrogen-cooled Thermo Nicolet 6700

spectrometer in 85° grazing angle mode with a 16 mm aperture. At least 128 scans were taken per sample at 4 cm^{-1} resolution.

Results and Discussion

Prior to monolayer formation, 16-chlorotrityl-mercaptohexadecanoic acid (CT-MHA) was synthesized using a three-step protocol as described previously.[11] Low-density SAMs and conventional SAMs were prepared by the immersion of microfabricated gold electrodes into ethanol solutions of either CT-MHA or MHA for 48 h at room temperature. In the case of the low-density SAMs, samples were immersed for 2 min in a 1:1 mixture of trifluoroacetic acid and ethanol, which resulted in quantitative cleavage of the acid-labile ester bonds. The reaction can be conveniently monitored by grazing-angle FTIR spectroscopy.[11,12] Monolayers were prepared and stored at room temperature under air, argon, and ethanol as well as at 4 °C under argon. The samples were compared to the corresponding high-density SAMs of MHA, which were stored under identical conditions. The stability of monolayer electrochemical insulating properties was assessed using electrochemical impedance spectroscopy (EIS), and the structural and chemical properties were assessed using Fourier transform infrared (FT-IR) spectroscopy and X-ray photoelectron spectroscopy (XPS), respectively.

Fourier Transform Infrared Spectroscopy

FTIR was performed to assess the effect of storage on the structure of low-density monolayers.[21] High- density SAMs of MHA typically show two characteristic high-frequency IR peaks: an asymmetric C-H stretching peak at ~2918 cm^{-1} and a symmetric C-H stretching peak at ~2850 cm^{-1} (peak assignments according to Nuzzo et al.[21]). These

stretches are representative of densely packed, crystalline alkyl chains whereas loosely packed alkyl chains typically show asymmetric C-H stretching peaks above 2920 cm^{-1} and symmetric C-H stretching peaks above 2852 cm^{-1}.[11,12] Figure 3.1 summarizes time-dependent storage experiments signifying the change in asymmetric C-H stretching peaks for low- and high-density MHA SAMs under various storage conditions. Figure 3.2 shows the corresponding data for the symmetric C-H stretching peaks. The high-density SAMs (solid circles) do not experience significant IR band shifts over time under any of the storage conditions examined in this study. In contrast, significant variations were observed for the low-density SAMs over the studied time course. Both symmetric and asymmetric methylene stretches, which were initially at 2923 and 2852 cm^{-1}, decreased significantly during the course of the study and were found to be at 2919 and 2849 cm^{-1} after 4 weeks of storage. The direction of the peak shifts toward lower wavenumbers suggests that the alkyl chains of the LDSAMs increased their packing order. This effect is observed to be independent of the storage conditions (Figure 3.2b,c). Possible explanations for this red shift of the symmetric and asymmetric methylene stretches may be as follows: (1) The alkyl chains of LDSAMs undergo a thermodynamically driven ordering over time, which can be attributed to energetically favorable van der Waals interactions of individual alkyl chains. (2) Chemical modification of the monolayers due to thiol oxidation and/or intercalation of contaminants restricts alkyl chain flexibility and leads to the red shift of the methylene stretches. (3) Segregation of the initially homogeneously distributed MHA thiolates leads to the formation of dense, crystalline islands over time. Whereas the phase segregation behavior (third hypothesis) has been well documented for high-density SAMs,[22-25] island formation should affect the

electrochemical barrier properties of the monolayer because the formation of dense islands would inevitably result in areas where the gold surface is exposed. However, the exposure of uncovered gold areas should be detectable on the basis of decreased electrochemical impedance.

Electrochemical Impedance Spectroscopy

To probe this hypothesis, electrochemical impedance spectroscopy (EIS) data for low- and high-density MHA SAMs were measured for 1 Hz $< f <$ 100 kHz to assess the broad electrochemical response of samples in both the capacitance- and resistance-dominated regimes.[26] Because the contribution to the observed impedance due to monolayer capacitance is dominant only at lower frequencies ($f <$ ~1000) and impedance at 1 Hz is representative of impedance in this regime, $|Z|_{1\ \mathrm{Hz}}$ has been reported to be a surrogate for the overall insulating properties exhibited by the SAMs.[26,27] For freshly prepared samples, $|Z|_{1\ \mathrm{Hz}}$ of LDSAMs was 17 kΩ, which is significantly lower than the impedance measured for the corresponding high-density monolayers, which was consistently above 40 kΩ. These values are in agreement with previously reported data[12] and are an indication of reduced barrier properties of the LDSAMs as compared to their conventional high-density counterparts. However, the impedance values of the LDSAMs are significantly higher than the values measured for bare gold surfaces under identical conditions (< 2 kΩ), suggesting that LDSAMs indeed exhibit homogeneous and robust coverage of the electrode surface.[11,12] After storage for up to 4 weeks in different environments and under two different temperatures, the electrochemical properties did not change significantly. Figure 3.3 shows the effect of extended storage over 1 month under different conditions for high- and low-density monolayers. Although LDSAMs are

hypothetically more susceptible to oxidative degradation compared to their high-density counterparts, the LDSAM samples stored in air at room temperature (Figure 3.3a, open circles) did not show dramatically different changes in impedance than the samples stored in less stressful environments (although greater deviation was observed at week 4). The differences between samples stored under argon at room temperature versus those stored at 4 °C (Figure 3.3b,c, open circles) were also negligible. For all storage conditions examined in this study, the impedance data of LDSAMs were constant for 4 weeks, indicating a robust maintenance of the insulating properties over this time period, thereby effectively ruling out the possibility of phase segregation as the cause of the changes in the FTIR spectra. Still, chemical changes such as oxidation or contamination could in principle contribute to the observed red shift in the FTIR spectra. In fact, it is important to recognize that oxidative degradation of SAMs under ambient conditions may occur without an adverse impact on electrochemical barrier properties. Schoenfisch et al.[5] demonstrated for high-density SAMs on gold that monolayer oxidation can concur with the maintenance of high impedance values. To assess changes in the chemical composition of the low-density monolayers under different storage conditions, XPS analysis was conducted for samples stored for 4 weeks, and the data were compared to those for freshly prepared samples.

X-ray Photoelectron Spectroscopy

XPS was performed to determine whether the different storage conditions had an effect on the oxidation of the LDSAMs, even beyond the level that may be detected by EIS. As shown in Table 3.1, the chemical compositions of both LDSAMs and conventional SAMs of MHA were in good agreement with the theoretically expected

values. Table 3.1 summarizes the component model fitting for these spectra. The observed peak areas for aliphatic carbons, carbons adjacent to the head and tail groups, and the carbonyl carbon correspond well with theoretical expectations. In addition, detailed analysis of the fine structure of the high-resolution S 2p spectra can reveal additional information regarding thiol oxidation. Figure 3.4a shows LD-MHA after 4 weeks of storage in air at room temperature. The high-resolution S 2p spectra of low-density SAMs show characteristic doublet signals at ~162.5 eV, which can be attributed to surface-bound thiols.[28] In contrast, doublet signals at ~167 eV, which are characteristic of oxidized sulfinate and sulfonate species,[6,29] are not present. Although a small shoulder on the left side of the original S $2p_{1/2}$ signal can be identified at ~163.5 eV, the spectra do not indicate substantial amounts of oxidized species as expected for a widely oxidized monolayer. Likewise, for LDMHA stored for 4 weeks in argon at room temperature (Figure 3.4b) and in argon at 4 °C (Figure 3.4c), characteristic oxidation peaks at ~167 eV are not observed. Whereas storage under inert conditions (argon) can be expected to reduce oxidation significantly, the lack of oxidation for the sample kept in an air environment may be less intuitive. This can be elucidated, however, by the work of Willey et al., who observed the rapid (< 24 h) oxidation of dodecanethiol SAMs exposed on a benchtop to ambient air, yet no significant oxidation when the samples were enclosed in sealed vials (as in this study).[8] It was suggested that the oxidation is driven by dilute atmospheric ozone,[5,28-29] which is rapidly depleted in sealed containers. To complement the high-resolution sulfur analysis, Figure 3.5 shows the corresponding high-resolution C 1s spectra of the low-density SAM samples. The high-resolution C 1s spectra reveal characteristic signals for aliphatic carbon (*C*-H) at 285.0 eV and carboxyl

carbon (*C*-OOH) at 288.8 eV. In addition, there is a third signal at 286.6 eV that can be attributed to thiol-bond carbon (*C*-SH) as well as carbon in the R position with respect to the carboxyl group (*C*-COOH). Quantitative analysis of the spectra is given in Table 3.1 and is in excellent agreement with the theoretically expected values for all examined storage conditions. Given the intrinsic sensitivity limit of XPS, any change in the overall composition of the SAM of about 1 atom % or more can be expected to be detected by XPS and can be ruled out on the basis of this study. Although the XPS data cannot entirely rule out oxidation and/or minimal contamination as the cause of the red shift observed in the FTIR study, these factors are most likely not the major contributors, given the XPS results. In addition, it is worthwhile to recognize that Figures 3.1d and 3.2d show the FTIR spectra of LDSAMs stored in ethanol solutions, which clearly provide different sources of contamination or oxidation than do samples stored under air or argon conditions, but the FTIR spectra show identical shifts of the methylene bands. On the basis of the XPS and electrochemical impedance analysis, thermodynamically driven chain ordering due to an increase in van der Waals interactions appears to be the most likely cause of the structural changes observed with FTIR. Similar ordering effects have been observed for high-density monolayers at increased temperatures, which increase the fluidity of the monolayers.[30]

Conclusions

Low-density self-assembled monolayers of mercaptohexadecanoic acid on gold were stored under air, argon (25 and 4 °C), and ethanol. Analysis by electrochemical impedance spectroscopy showed no significant change in the electrochemical insulating

properties of the air, argon, and ethanol samples over the course of 4 weeks. Oxidative degradation of these samples was also not observed by X-ray photoelectron spectroscopy. However, the fine structure of low-density SAMs as determined by Fourier transform infrared spectroscopy showed a trend toward decreasing alkyl chain fluidity over time. Increased ordering of MHA molecules on the surface is a possible cause of these observations. The robust chemical and electrochemical stability of low-density SAMs under a variety of practical storage conditions points toward the applicability of these systems in potential technological applications.

Acknowledgment

D.K.P. acknowledges support from a graduate fellowship from the National Institutes of Health through the University of Michigan Cellular Biotechnology Training Program. This project was funded by grants from the National Institutes of Health (5 R21 EB005732-02) and the Department of Defense (Idea award, W81XWH-06-1-0271).

Figures

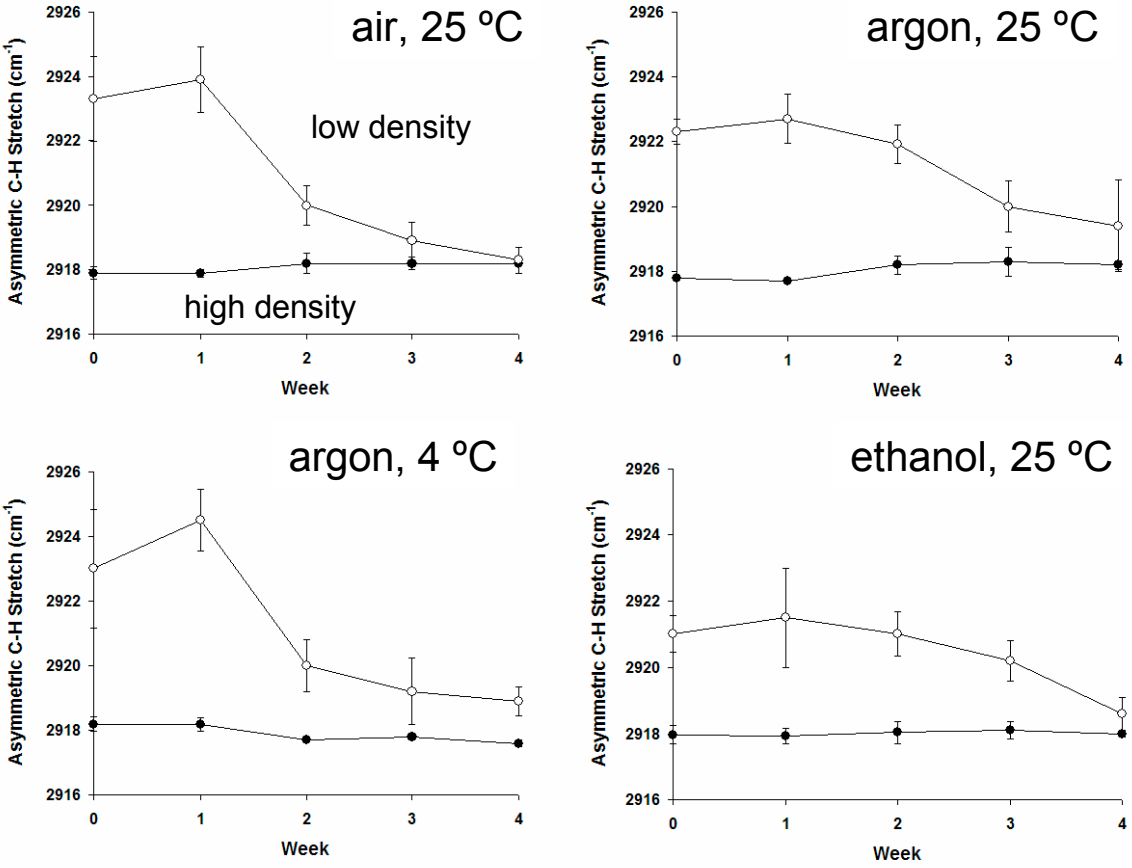

Figure 3.1. FTIR peak locations for the asymmetric C-H stretch of high-density SAMs (●) and low-density SAMs (O) stored under various conditions: (a) 20 °C under air, (b) 20 °C under argon, (c) 4 °C under argon, and (d) 20 °C under ethanol.

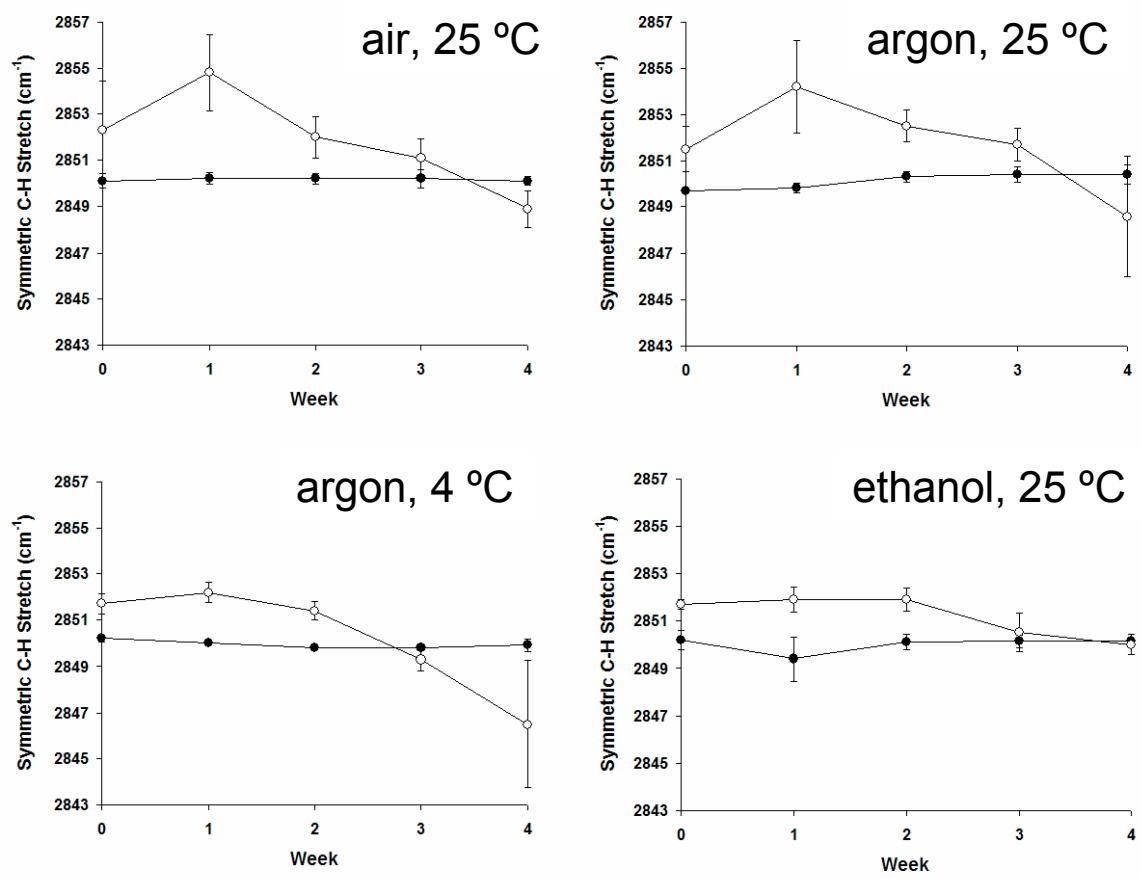

Figure 3.2. FTIR peak locations for the symmetric C-H stretch of high-density SAMs (●) and low-density SAMs (O) stored under various conditions: (a) 20 °C under air, (b) 20 °C under argon, (c) 4 °C under argon, and (d) 20 °C under ethanol.

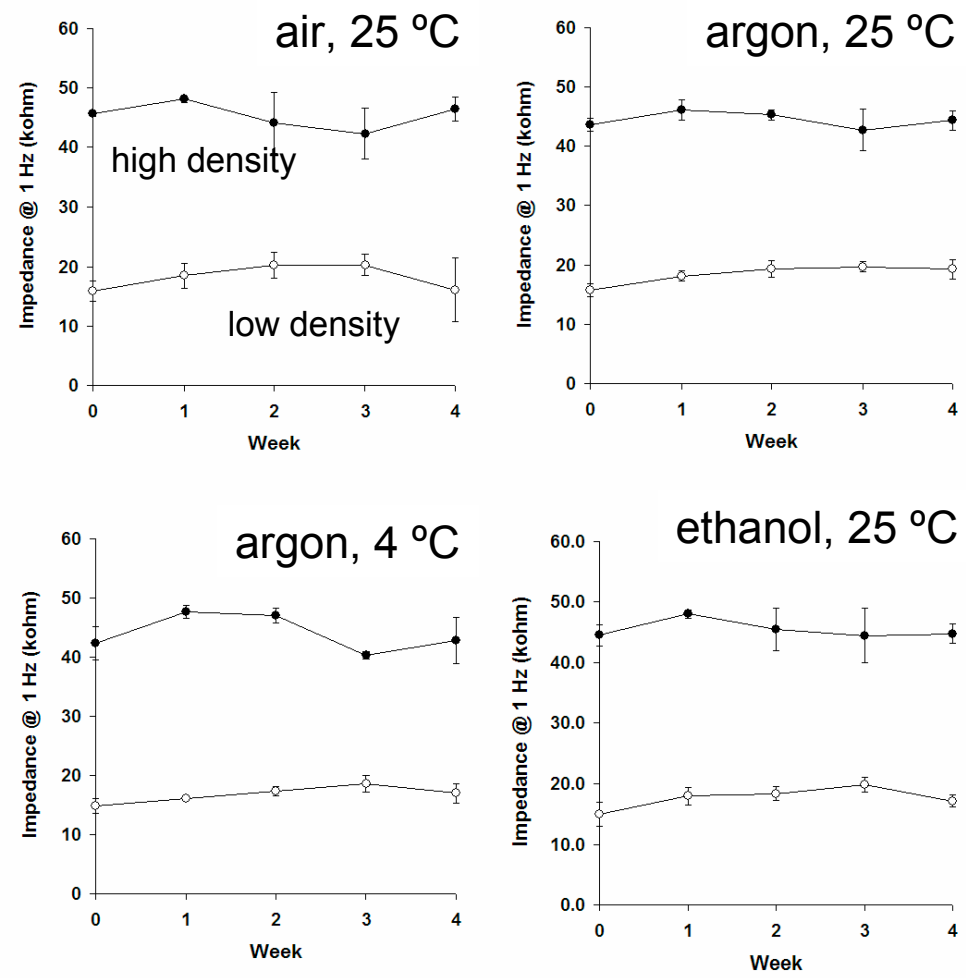

Figure 3.3. Impedance modulus at 1 Hz of high-density SAMs (●) and low-density SAMs (O) stored under various conditions: (a) 20 °C under air, (b) 20 °C under argon, (c) 4 °C under argon, and (d) 20 °C under ethanol.

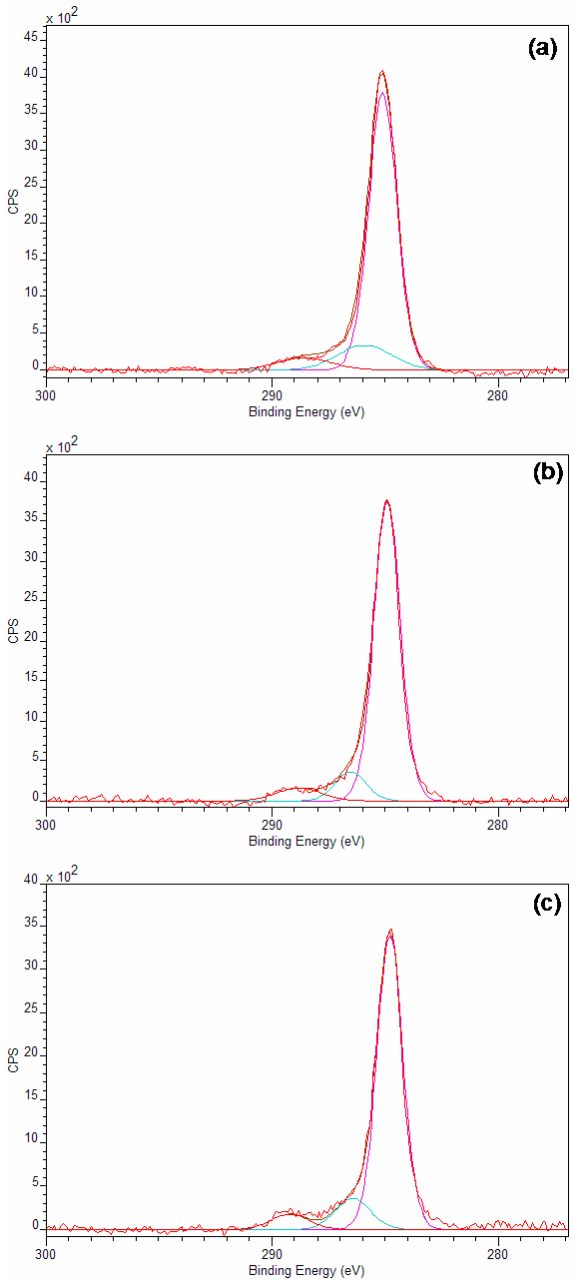

Figure 3.4. High-resolution S 2p XPS spectra of low-density SAMs before storage (a) after 4 weeks at 20 °C under air, (b) after 4 weeks at 20 °C under argon, and (c) after 4 weeks at 4 °C under argon.

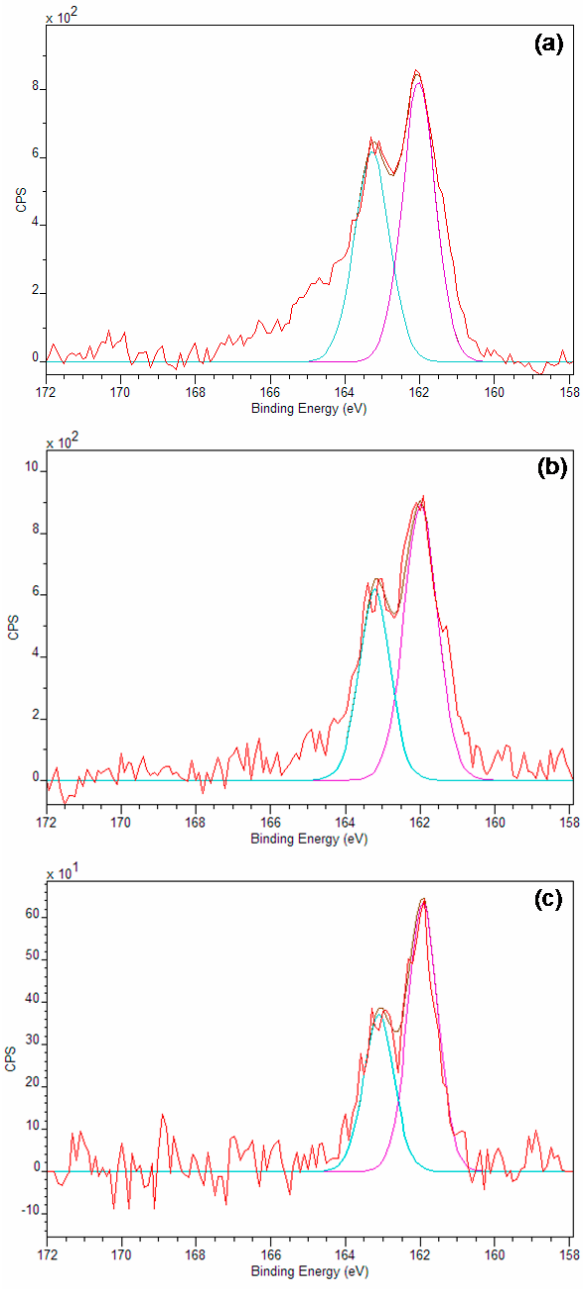

Figure 3.5. High-resolution C 1s XPS spectra of low-density SAMs before storage (a) after 4 weeks at 20 °C under air, (b) after 4 weeks at 20 °C under argon, and (c) after 4 weeks at 4 °C under argon.

Table

	Theoretical	25° C, air		25° C, argon		4° C, argon	
	%	Area	%	Area	%	Area	%
C-H_2	82	5951	80	5368	84	4854	82
C-S, C-CO_2H	12	994	13	612	10	696	12
CO_2H	6	497	7	399	6	367	6

Table 3.1. XPS C 1s Spectra Component Analysis for LDSAMs Stored for 4 Weeks under Different Storage Conditions.

References

(1) Love, J. C.; Estroff, L. A.; Kriebel, J. K.; Nuzzo. R. G.; Whitesides, G. M. *Chem. Rev.* **2005**, *105*, 1103-1169.

(2) Schreiber, F. *J. Phys.: Condens. Matter* **2004**, *16*, R881-R900.

(3) Schwartz, D. K. *Annu. Rev. Phys. Chem.* **2001**, *52*, 107-137.

(4) Ulman, A. *Chem. Rev.* **1996**, *96*, 1533-1554.

(5) Schoenfisch, M. H.; Pemberton, J. E. *J. Am. Chem. Soc.* **1998**, *120*, 4502- 4513.

(6) Horn, A. B.; Russell, D. A.; Shorthouse, L. J.; Simpson, R. E. *J. Chem. Soc., Faraday Trans.* **1996**, *92*, 4759-4762.

(7) Flynn, N. T.; Tran, T. N. T.; Cima, M. J.; Langer, R. *Langmuir* **2003**, *19*, 10909-10915.

(8) Willey, T. M.; Vance, A. L.; van Buuren, T.; Bostedt, C.; Terminello, L. J.; Fadley, C. S. *Surf. Sci.* **2005**, *576*, 188-196.

(9) Lahann, J.; Langer R. *MRS Bull.* **2005**, *30*, 185-188.

(10) Choi, I. S.; Chi, Y. S. *Angew. Chem., Int. Ed.* **2006**, *45*, 4894-4897.

(11) Lahann, J.; Mitragotri, S.; Tran, T. N.; Kaido, H.; Sundaram, J.; Choi, I. S.; Hoffer, S.; Somorjai, G. A.; Langer, R. *Science* **2003**, *299*, 371-373.

(12) Peng, D. K.; Yu, S. T.; Alberts, D. J.; Lahann, J. *Langmuir* **2007**, *23*, 297-304.

(13) Vemparala, S.; Kalia, R. K.; Nakano, A.; Vashishta, P. *J. Chem. Phys.* **2004**, *121*, 5427-5433.

(14) Liu, Y.; Mu, L.; Liu, B.; Zhang, S.; Yang, P.; Kong, J. *Chem. Commun.* **2004**, 1194-1195.

(15) Park, J. S.; Vo, A. N.; Barriet, D.; Shon, Y. S.; Lee, T. R. *Langmuir* **2005**, *21*, 2902-2911.

(16) Berron, B.; Jennings, G. K. *Langmuir* **2006**, *22*, 7235-7240.

(17) Winnik, F. M.; Whitten, D. G. *Langmuir* **2007**, *23*, 1-2.

(18) de Las Heras Alarcon, C.; Pennadam, S.; Alexander, C. *Langmuir* **2005**, *34*, 276-285.

(19) Yoshida, M.; Langer, R.; Lendlein, A.; Lahann, J. *Poly. Rev.* **2006**, *4*, 347-375.

(20) Squires, T. M.; Quake, S. R. *Rev. Mod. Phys.* **2005**, *77*, 977-1026.

(21) Nuzzo, R. G.; Dubois, L. H.; Allara, D. L. *Langmuir* **1990**, *112*, 558-569.

(22) Stranick, S. J.; Parikh, A. N.; Tao, Y. Y.; Allara, D. L.; Weiss, P. S. *J. Phys. Chem.* **1994**, *98*, 7636-7646.

(23) Chen, S.; Li, L.; Boozer, C. L.; Jiang, S. *Langmuir* **2000**, *16*, 9287-9293.

(24) Smith, R. K.; Reed, M. S.; Lewis, P. A.; Monnell, J. D.; Clegg, R. S.; Kelly, K. F.; Bumm, L. A.; Hutchison, J. E.; Weiss, P. S. *J. Phys. Chem. B* **2001**, *105*, 1119-1122.

(25) Imabayashi, S.; Hobara, D.; Kakiuchi, T. *Langmuir* **2001**, *17*, 2560-2563.

(26) Boubour, E.; Lennox, R. B. *Langmuir* **2000**, *16*, 4222-4228.

(27) Boubour, E.; Lennox, R. B. *Langmuir* **2000**, *16*, 7464-7470.

(28) Lee, M. T.; Hsueh, C. C.; Freund, M. S.; Ferguson, G. S. *Langmuir* **1998**, *14*, 6419-6423.

(29) Tarlov, M. J.; Burgess, D. R. F.; Gillen, G. J. *J. Am. Chem. Soc.* **1993**, *115*, 5305-5306.

(30) Norrod, K. L.; Rowlen, K. L. *J. Am. Chem. Soc.* **1998**, *9*, 2656-2657.

(31) Zhang, Y. M.; Terrill, R. H.; Tanzer, T. A.; Bohn, P. W. *J. Am. Chem. Soc.* **1998**, *9*, 2654-2655.

(32) Delamarche, E.; Michel, B.; Kang, H.; Gerber, C. *Langmuir* **1994**, *10*, 4103.

CHAPTER 4

LATERAL MOBILITY IN LOW-DENSITY SELF-ASSEMBLED MONOLAYERS

Abstract

This chapter presents the analysis of micropatterned surfaces with defined regions of low-density self-assembled monolayer residing in a background of high density monolayer. The influence of incubation temperature and monolayer chain length is examined. Ellipsometry, infrared spectroscopy, and electrochemical impedance spectroscopy reveal robust thermal stability of the micropatterned surfaces up to 373 K, greater thermal sensitivity of shorter chain length surfaces, and an apparent diffusion phenomenon of thiolate species from regions of high-density to regions of low-density.

Introduction

Self-assembled monolayers (SAMs) of organothiolates on metals have been widely studied because of the flexibility and consistency with which they can produce well-defined structures with diverse surface chemistries.[1] A distinguishing characteristic of the most widely studied SAM systems—alkanethiolates on gold—is the high degree of order and constraint exhibited by their constituent molecules as a result of the spontaneous self-assembly process. Although this tightly packed structure is important for certain applications (e.g., electrical insulators, chemical etch resists), increasing

attention is being given to SAMs designed with low density configurations and increased steric freedom, allowing for functions such as active conformational transitions[2-4] and the tuning of surface properties including friction,[5] electron transfer,[6] protein adsorption,[7-9] and surfactant interactions.[10-12]

Thermal stability is an important characteristic for technological applications of SAMs, yet little work has addressed thermally-induced mobility—i.e., lateral diffusion of thiolates—in the context of low-density SAMs. The effect of elevated temperature on traditional, high-density SAMs has been examined since the initial discoveries of the Whitesides group[13] and for a wide variety of SAM systems thereafter,[14-17] but low-density systems have not yet been characterized as thoroughly. Past studies on high-density systems generally observe that with increasing temperature comes, first, increased disorder amongst the flexible alkyl chains of the monolayer, followed by thermally-induced desorption of the thiolate from the surface, with the energetic thresholds for each stage differing depending on the specific monolayer system. To these factors one can add the potential influence of thermally-induced interactions between domains of differing density, driven by lateral displacement of thiols within the plane of the gold surface. Along this line, one study has examined the lateral motion at room temperature of a single thiolate molecule embedded in a SAM.[18] However, the role of such phenomena in aggregate and as a function of temperature has not yet been emphasized.

In this study, we address the thermal stability of low-density SAMs, examining the role of interactions between neighboring low- and high-density regions that are otherwise chemically identical. We do this by using microcontact printing to generate surfaces with well-defined, micropatterned regions of low-density SAM residing in a

background of high-density SAM. We then expose these surfaces to elevated temperature for a defined time period, and then use ellipsometry, infrared spectroscopy, and electrochemical impedance spectroscopy to analyze the resulting effects on film thickness, conformational structure, and electrochemical permeability. We perform this analysis on surfaces with two different chain lengths, in order to assess the influence of inter-chain interactions on thermally driven behavior.

Experimental Section

The procedure for producing the micropatterned SAMs is summarized in Figure 1. A PDMS stamp with a 35 x 35 μm square pattern is UV ozone treated for 5 min, then inked with a 1 mM ethanolic solution of a low-density SAM precursor, the chlorotrityl (CT) ester of either mercaptohexadecanodoic acid (MHA, C16 length) or mercaptoundecanoic acid (MUA, C11 length) (synthesis described previously).[2,3] The inked PDMS is then stamped onto a gold surface (100 nm gold E-beam deposited on silicon with a 10 nm titanium adhesion layer) for 30 s. The unprinted region is then backfilled by immersing substrate for 30 min in a 1 mM ethanolic solution of mercaptohexadecanodoic acid or mercaptoundecanoic acid, with the backfilling molecules' chain length matching that of the precursor. The substrate is then washed with ethanol and immersed in a 1:1 solution of trifluoroacetic acid and ethanol for 2 min to cleave the acid labile chlorotrityl ester from the low-density precursor molecules. The substrate is then washed with ethanol, dried under a stream of N_2, and held at room temperature for 90 min to promote cohesion of the high density background region. (Holding at room temperature for periods up to and beyond 1 week do not influence the observed pattern; data not shown.) This procedure yields surfaces of low-density SAM

square regions in a high density SAM background, either at the C16 or C11 chain length. Samples were then held either on the benchtop at 298 K or in a temperature-controlled oven at 333 K, 373 K, and 423 K for 5 hours each.

Results and Discussion

Imaging ellipsometry analysis of the samples was performed using a Nanofilm EP3 nulling ellipsometer with a wavelength of 532 nm, angle of incidence of 60°, and polarizer range of 4º, with 10 image scans per sample for both ellipsometric delta and psi. Figure 2 shows imaging ellipsometry delta maps and delta profiles of C16 and C11 density-patterned SAMs after 5 hr exposure at each temperature level. Because the chemical identity of both regions is identical, the contrast observed reflects differences in film thickness caused by differences in packing density between the square and background regions; the more crystalline high density regions show greater thickness than the loosely-packed low-density regions. For the C16 length samples, the density pattern can be observed on the samples kept at 298 K, 333 K, and 373 K, but for the sample kept at 423 K, the pattern is no longer visible. For the C11 length samples, the density pattern is clearly visible for the samples kept at 298 K and 333 K, but begins to fade for the sample kept at 373 K, and is no longer visible for the sample kept at 423 K.

Figure 3 shows the results of thickness modeling using the obtained delta and psi data. The modeling layers were air atmosphere, monolayer film (n = 1.45, k = 0), and gold film (n = 0.4632, k = 2.3171). For the C16 length samples shown in Figure 3a, we see an increase in apparent thickness of the high-density background region from the sample kept at 298 K (1.62 nm) to the sample kept at 333 K (1.82 nm) and to the sample kept at 373 K (1.85 nm), but a decrease in apparent thickness from the sample kept at 373

K (1.85 nm) to the sample kept at 423 K (1.40 nm). The low-density region in Figure 3a, meanwhile, does not experience significant thickness changes for the samples kept at 298 K (1.23 nm), 333 K (1.16 nm), and 373 K (1.26 nm), but they experience an increase in thickness for the sample kept at 423 K (1.40 nm).

The increase in apparent thickness of the high density region at 333 K and 373 K, relative to that seen at 298 K, can be explained by an annealing effect at moderately elevated temperatures. This effect is not experienced by the low-density region, possibly because of the greater steric freedom of the alkyl chains in that region. At 423 K, the decrease in apparent thickness observed in the high density region may be explained by desorption of MHA from the surface, infiltration of MHA from the high-density region into the low-density region, or a combination of these two factors. We note again the increase in thickness of the low-density region from 373 K to 423 K, such that the thickness becomes equal to that of the high-density region and the contrast between the two regions disappears. This suggests that the net density of MHA in the low-density region increases between 373 K and 423 K and that infiltration of MHA from the high-density region into the low-density region is occurring until the entire surface becomes homogeneously distributed with MHA. Desorption of MHA from either the high- or low-density region can be occurring simultaneously.

For the C11 samples shown in Figure 3b, we see an increase in apparent thickness of the high-density background region from the sample kept at 298 K (0.97 nm) to the sample kept at 333 K (1.18 nm) and to the sample kept at 373 K (1.22 nm), and a decrease in apparent thickness from the sample kept at 373 K (1.22 nm) to the sample kept at 423 K (0.97 nm). The low-density region in Figure 3b experiences an increase in

thickness from the sample kept at 298 K (0.66 nm) to the sample kept at 333 K (0.78 nm) and to the sample kept at 373 K (1.12 nm), but a decrease in thickness from the sample kept at 373 K (1.12 nm) to the sample kept at 423 K (0.97 nm).

An annealing effect in the high density region is observed for the C11 samples at 333 K and 373 K, as was seen with the C16 samples. The drop in thickness of the C11 high density region at 424 K is also observed. What differs for the C11 length is the behavior of the low-density region. The increase in thickness observed at 373 K suggests that the C11 system has a lower temperature threshold than the C16 system for infiltration of thiols from the high-density region to the low-density region. At 423 K, the elimination of contrast between the high- and low-density regions, as well as the decrease in thickness for both regions from the values seen at 373 K, suggests completion of the infiltration process and the onset of desorption of MUA thiols from the homogeneous surface.

Fourier transform infrared (FTIR) spectra of the samples were obtained in order to assess the effect of patterning and temperature on the conformational structure of the SAMs. Analysis was performed using a Thermo Nicolet 6700 spectrometer with an 85° grazing angle attachment and 128 scans per sample at 4 cm^{-1} resolution. Figure 3 shows the resulting spectra, which represent an average over the entire patterned surface, including both low- and high-density regions. C16 length samples are shown in Figure 3a, and C11 length samples are shown in Figure 3b. Spectra for unpatterned high- and low-density SAMs at room temperature are included as reference (black and grey lines, respectively), and upon comparison of the reference samples, we see the low-density asymmetric and symmetric C-H stretching peaks are red-shifted relative to the high-

density peaks—an effect resulting from the increased fluidity of the low-density alkyl chains. For the micropatterned samples, the C16 length sample at 298 K shows peaks at 2918.5 cm^{-1} and 2850.3 cm^{-1}, while the C11 length sample at 298 K shows peaks at 2919.7 cm^{-1} and 2850.1 cm^{-1}. These peaks are modestly red-shifted relative to the unpatterned high-density C16 and C11 samples. Peak broadening is also evident, particularly for the C11 sample at 298 K. Although here we do not observe distinct peaks for high- and low-density regions—a possible function of instrument resolution—the intermediately located and broadened FTIR peaks of the patterned samples suggest an aggregate level of fluidity and structure consistent with the ellipsometric data above. As temperature is increased, the peaks for the C16 length patterned samples do not shift significantly until 423 K, at which point they are shifted further than the low-density C16 reference sample. The C11 samples, meanwhile, begin to shift at 373 K, and at 423 K are shifted further than the low-density C11 reference sample. These data indicate structural stability of the C16 length patterned samples for 5 hr up to at least 373 K and increased thermal sensitivity of the C11 length samples.

The changes in structure and conformation induced by elevated temperature also influence the electrochemical properties of the patterned SAMs. Low-density SAMs exhibit greater ionic permeability and therefore lower resistance and capacitance than high-density SAMs.[3,4] Electrochemical impedance spectroscopy (EIS) is a sensitive method for measuring these properties.[19,20] Figure 4 shows EIS results for the patterned samples as well as unpatterned high- and low-density SAM and bare gold reference samples. Analysis was performed using a Gamry PCI4/300 potentiostat, EIS300 software module, and standard 3-electrode electrochemical cell (saturated calomel reference

electrode, platinum mesh counter electrode, and N_2-purged phosphate buffered saline electrolyte). The applied potential had an AC amplitude of 10 mV r.m.s., frequency range of 1 Hz to 10^5 Hz, and DC bias of 0 mV w.r.t. SCE, and the current response was recorded at ten points per decade in frequency. The results are analogous to the FTIR results, with patterned samples showing greater permeability (lower impedance) than high density samples as a result of the presence of the low-density patterned regions. For C16 length samples (Figure 4a), no significant difference in impedance was observed for samples kept at 298 K, 333 K, and 373 K, but the sample kept at 423 K had an impedance curve close to that of the low-density C16 reference sample. For C11 length samples (Figure 4b), no significant difference in impedance was observed for samples kept at 298 K and 333 K, but the sample kept at 373 K had a marginally lower impedance curve, and the sample kept at 423 K had a impedance curve very close to that of the low-density C11 reference sample. The maintenance of robust electrochemical barrier properties is thus observed for C16 patterned SAMs for 5 hr up to at least 373 K, while C11 patterned SAMs show a lower thermal threshold for losses in integrity.

Conclusions

Patterning and temperature were thus observed to have a consistent trend of effects on SAMs with respect to film thickness as measured by ellipsometry, conformational structure as measured by FTIR spectroscopy, and electrochemical barrier properties as measured by EIS. Elevated temperature appears to cause migration of thiolates from high density regions to low density regions. This effect depends both on temperature and on SAM chain length, suggesting interplay between the energetics of the gold-thiol interaction and inter-chain van der Waals interactions. Independent of the

lateral migration effect, micropatterned SAMs of low-density MHA and MUA show good thermal stability at temperatures up to 373 K and 333 K, respectively, which may have positive implications for potential technological applications.

Acknowledgment

This project was funded by grants from the National Institutes of Health (5 R21 EB005732-02) and the Department of Defense (Idea Award, W81XWH-06-1-0271), as well as a graduate fellowship for D.K.P. from the National Institutes of Health / University of Michigan Cellular Biotechnology Training Program.

Figures

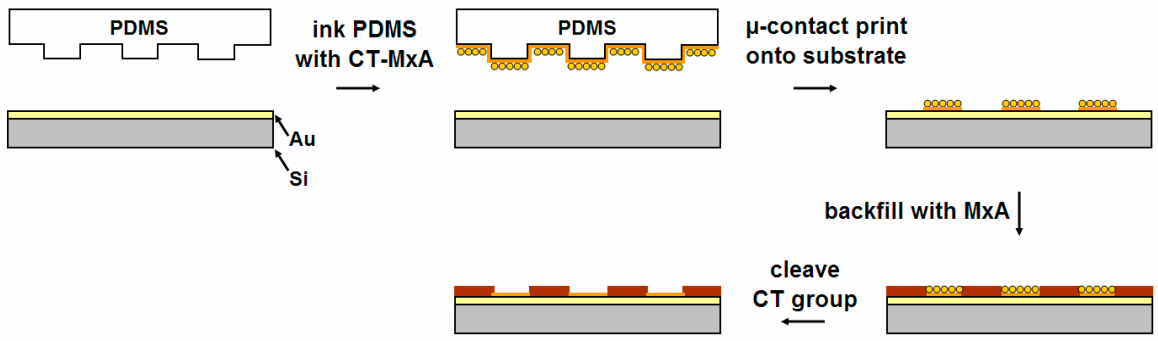

Figure 4.1. Schematic illustration of the procedure for patterning regions of low-density SAM in a background of high-density SAM.

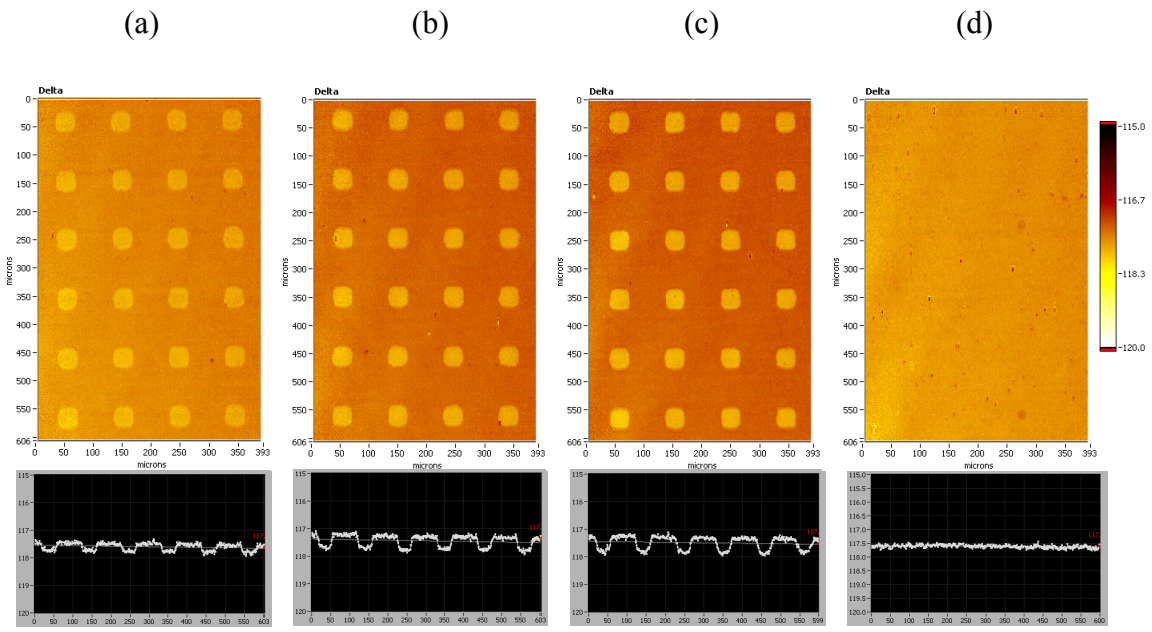

Figure 4.2. Imaging ellipsometry delta maps and delta profiles of micropatterned SAMs after 5hr exposure to elevated temperature (a) C16 length, 298 K (b) C16 length, 333 K, (c) C16 length, 373 K, and (d) C16 length, 423 K. Delta profiles shown below each map represent delta values along a vertical line drawn across one column of square patterns.

(a) (b) (c) (d)

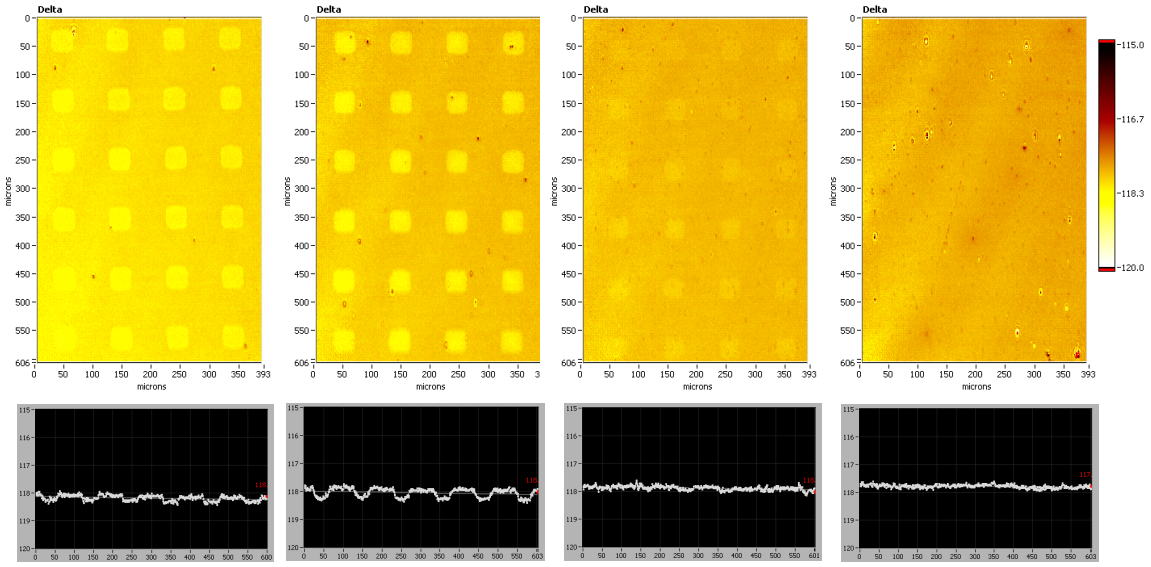

Figure 4.3. Imaging ellipsometry delta maps and delta profiles of micropatterned SAMs after 5hr exposure to elevated temperature (a) C11 length, 298 K, (b) C11 length, 333 K, (c) C11 length, 373 K, and (d) C11 length, 423 K. Delta profiles shown below each map represent delta values along a vertical line drawn across one column of square patterns.

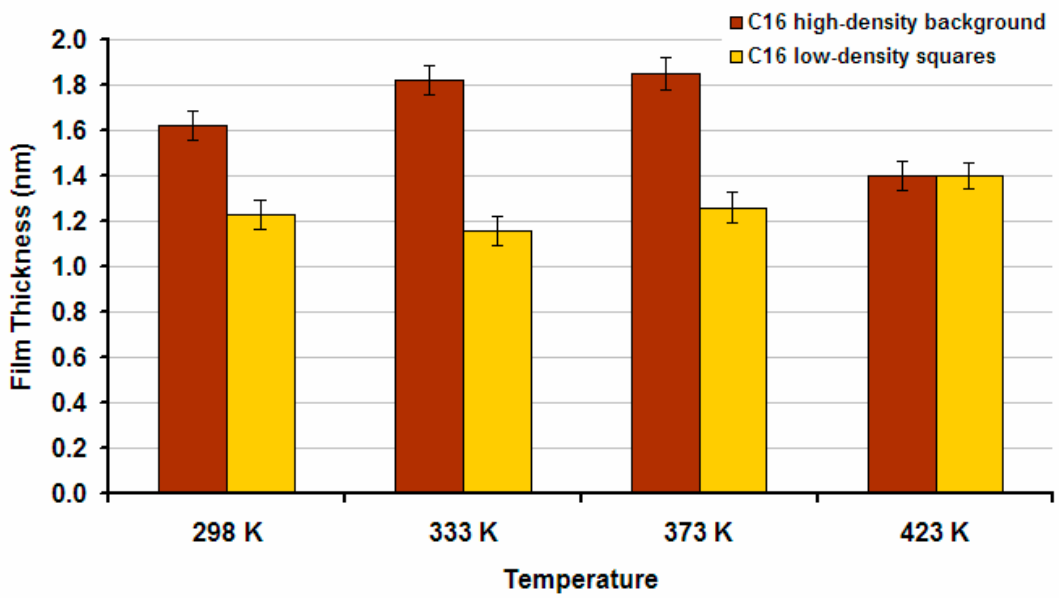

Figure 4.4. Ellipsometric thickness modeling of C16 micropatterned SAMs.

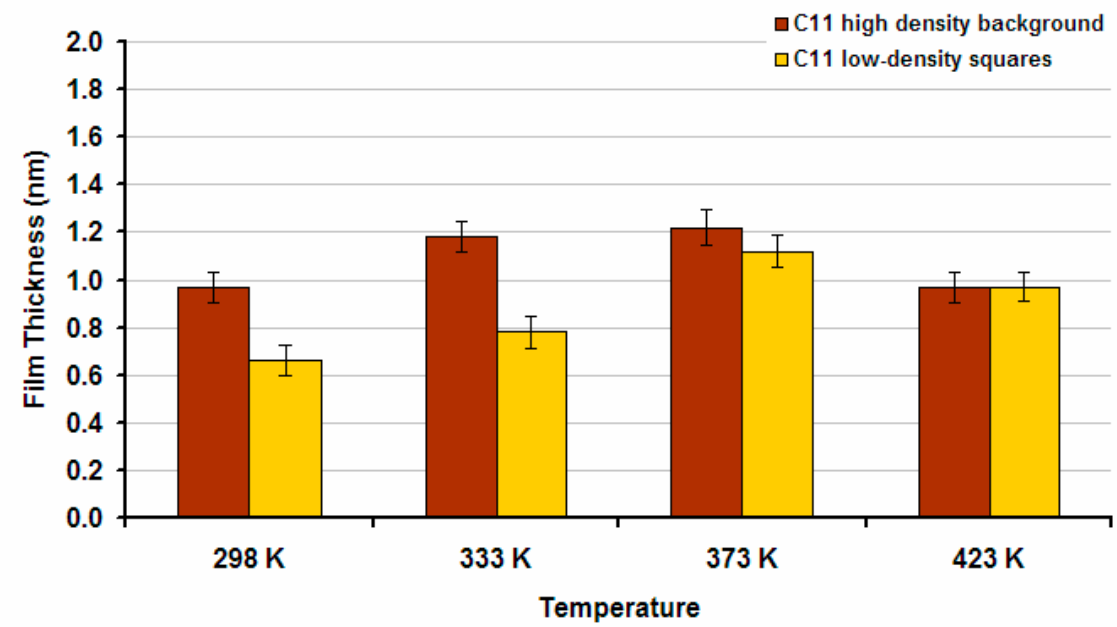

Figure 4.5. Ellipsometric thickness modeling of C11 micropatterned SAMs.

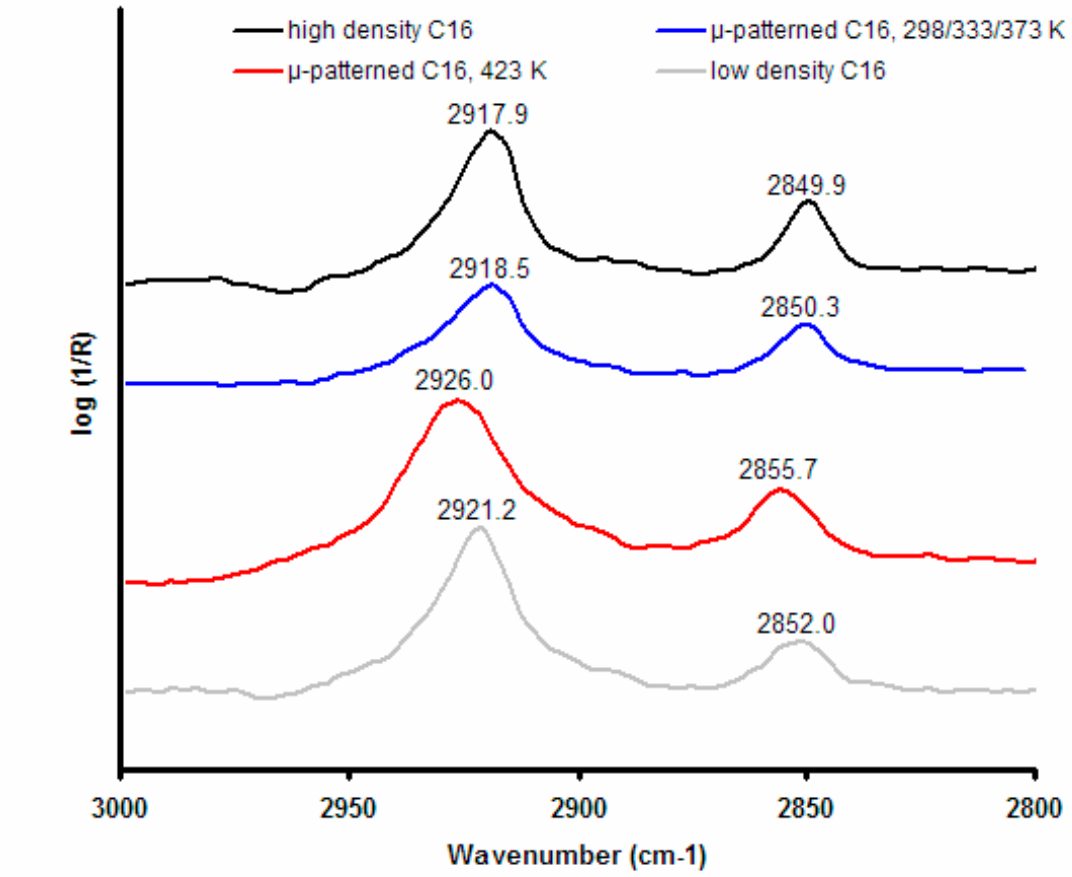

Figure 4.6. FTIR of C16 micropatterned SAMs.

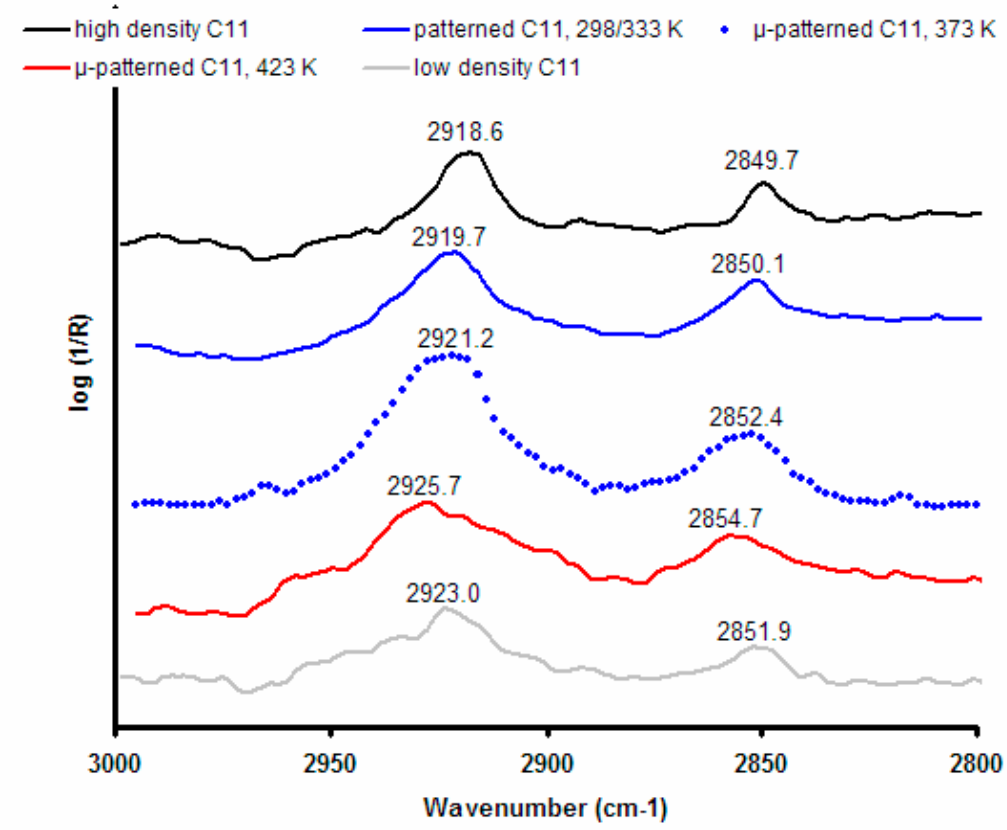

Figure 4.7. FTIR of C11 micropatterned SAMs.

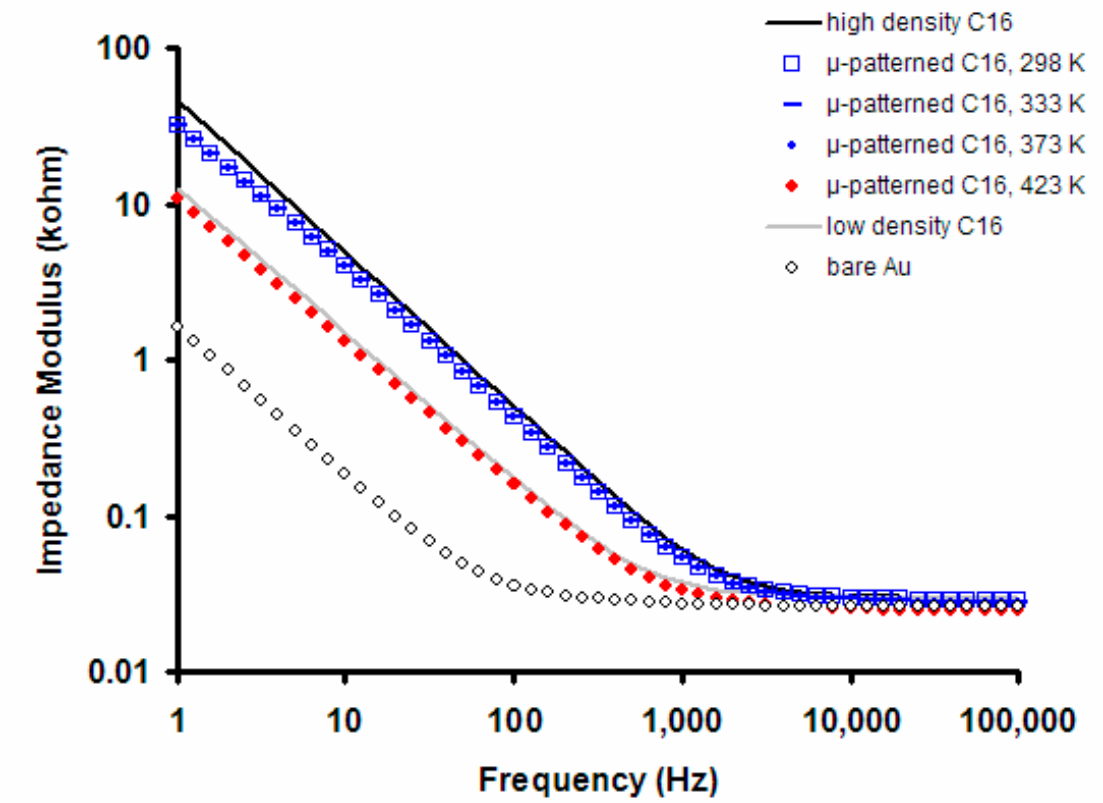

Figure 4.8. Ellipsometric thickness modeling of C16 micropatterned SAMs.

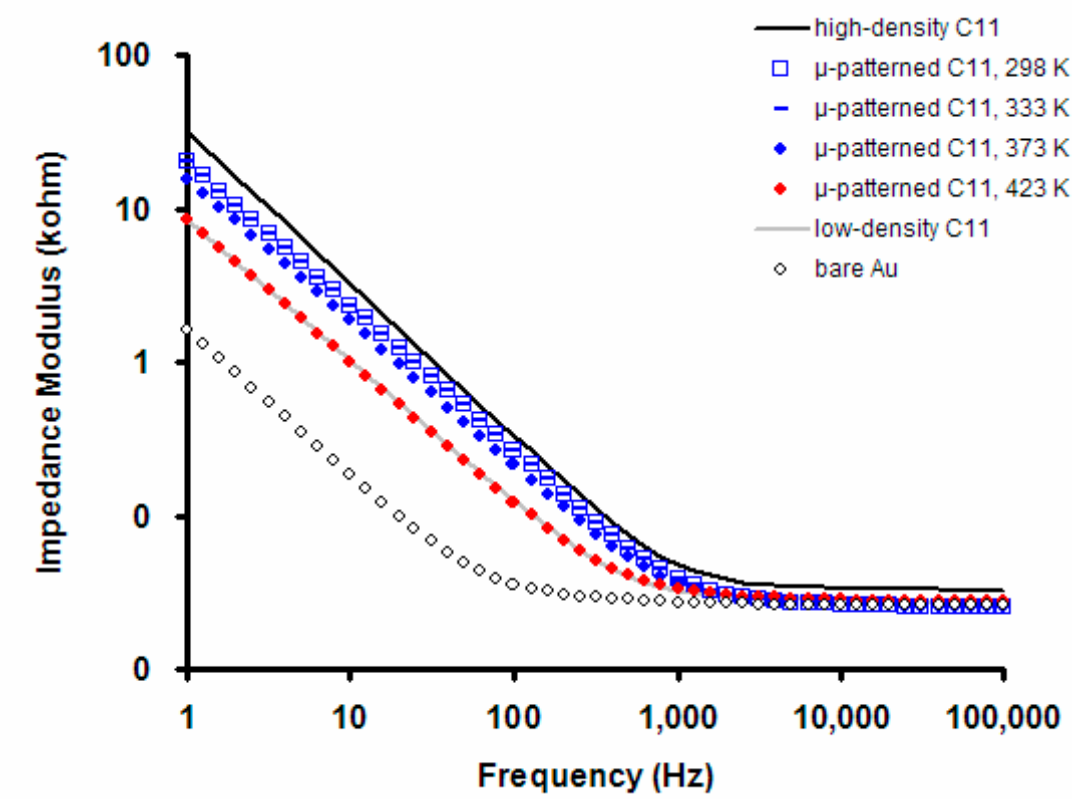

Figure 4.9. Ellipsometric thickness modeling of C11 micropatterned SAMs.

References

(1) Love, J.C.; Estroff, L.A.; Kriebel, J.K.; Nuzzo. R.G.; Whitesides G.M. *Chem. Rev.* **2005**, *105*, 1103-1169.

(2) Lahann, J.; Mitragotri, S.; Tran, T.N.; Kaido, H.; Sundaram, J.; Choi, I.S.; Hoffer, S.; Somorjai, G.A.; Langer, R. *Science* **2003**, *299*, 371-373.

(3) Peng, D.K.; Yu, S.T.; Alberts, D.J.; Lahann, J. *Langmuir* **2007**, *23*, 297-304.

(4) Peng, D.K.; Lahann, J. *Langmuir* **2007**, *23*, 10184-10189.

(5) Lee, S.; Shon, Y.S.; Colorado R.; Guenard, R.L.; Lee, T.R.; Perry, S.S. *Langmuir* **2000**, *16*, 2220-2224.

(6) Shao, H.B.; Yu, H.Z.; Zhao, J.W.; Zhang, H.L.; Liu, Z.F. *Chem Lett* **1997**, 749-750.

(7) Choi, E.J.; Foster M.D.; Daly, S.; Tilton, R.; Przybycien, T.; Majkrzak, C.F.; Witte, P.; Menzel, H. *Langmuir* **2003**, *19*, 5464-5474.

(8) Liu, Y.; Mu, L.; Liu, B.; Zhang, S.; Yang, P.; Kong, J. *Chemical Communications* **2004**, *10*, 1194-1195.

(9) Petrash, S.; Cregger, T.; Zhao, B.; Pokidysheva, E.; Foster, M.D.; Brittain, W.J.; Sevastianov, V.; Majkrzak, C.F. *Langmuir* **2001,** *17*, 7645-7651.

(10) Arduengo, A.J.; Moran, J.R.; Rodriguez-Parada, J.; Ward, M.D. *J. Am. Chem. Soc.* **1990**, *112*, 6153-6154.

(11) Bao, H.F.; Peng, Z.Q.; Wang, E.K.; Dong, S.J. *Langmuir* **2004**, *20*, 10992-10997.

(12) Peng, Z.Q.; Dong, S.J. *Langmuir* **2001**, *17*, 4904-4909.

(13) Bain, C.D.; Troughton, E.B.; Tao, Y.T.; Whitesides, G.M. *J Am. Chem. Soc.* **1989**, *111*, 321-335.

(14) Zhang, Z.S.; Wilson, O.M.; Efremov, M.Y.; Olson, E.A.; Braun, P.V.; Senaratne, W.; Ober, C.K.; Zhang, M.; Allen, L.H. *Applied Physics Letters* **2004**, *84*, 5198-5200.

(15) Schreiber, F. *Progress in Surface Science* **2000**, *65*, 151-256.

(16) Nuzzo, R.G.; Korenic, E.M.; Dubois, L.H. *J. Chem. Phys.* **1990**, *93*, 767-773.

(17) Fenter, P.; Eisenberger, P.; Liang, K.S. *Physical Review Letters* **1993**, *70*, 2447-2450.

(18) Wakamatsu, S.; Fujii, S.; Akiba, U.; Fujihira, M. *Nanotechnology* **2003**, *14*, 258-263.

(19) Boubour, E.; Lennox, R.B. *Langmuir* **2000**, *16*, 4222-4228.

(20) Boubour, E.; Lennox, R.B. *Langmuir* **2000**, *16*, 7464-7470.

CHAPTER 5

INTERACTION OF ANALYTE MOLECULES WITH LOW-DENSITY SELF-ASSEMBLED MONOLAYERS

Abstract

Switchable self-assembled monolayer technology employs a unique method to generate low surfaces densities of carboxyl-terminated thiolates on gold substrates, allowing steric freedom for reversible conformational transitions that can reversibly switch the properties of the surface between hydrophilic and hydrophobic states. This study examines the ability of these low density monolayers to capture or intercalate molecules from the external solution in a controllable fashion. We confirm the ability of low density SAMs to intercalate fatty acids and fluorescently labeled hydrophobic molecules. This capability will enable further study in potential areas of application such as dynamic surfaces for cell adhesion studies and biosensor platforms for molecular disease markers.

Introduction

A self-assembled monolayer (SAM) is a single layer of amphiphilic molecules that spontaneously organizes itself upon a solid substrate due to specific affinity between the headgroup of the amphiphile and the substrate. A schematic of a basic SAM is shown in Figure 5.1. The spontaneous formation of SAMs by initial adsorption of the

headgroups to the surface and by subsequent restructuring of the tailgroups to form a crystalline or semi-crystalline thin film makes possible the formation of ordered structures that could not be practically achieved by traditional chemical synthesis. Recent review articles discussing the general properties of SAMs have focused on SAM structure,[1-4] formation and growth,[2-5] dynamics,[6,7] phase transitions,[7] stability,[8] and spectroscopic properties.[9,10]

SAMs are desirable for use in a diverse range of applications due to their practical ease of production and the flexibility that they offer for modification and functionalization of surfaces. This flexibility comes from the diversity of head group-substrate interactions[1] (thiol headgroups on gold substrates being the most common), the ability to produce functionalized surfaces through changes in tailgroup chemistry, the reactivity of functionalized monolayer surfaces,[11-13] and the ability to pattern monolayers on surfaces.[14-17] For these reasons, SAMs have been documented for use in a wide variety of applications, including etch resists,[18] chemical separations,[19] chemical sensors,[20,21] electronic transistors,[22,23] electroanalysis,[24] biomolecular electronics,[25] biosensors,[26,27] bioactive surfaces,[28,29] and biological microarrays.[30,31]

The unique property of the monolayers examined in this study is the engineered low density of molecules on the surface, yielding a loose-packed and conformationally flexible structure which has the potential to allow intercalation of compatible hydrophobic molecules or amphiphiles from the external solution. This behavior would contrast with that of high density monolayers, which in such cases typically form hybrid bilayers.[32,33]

Alternate methods have been demonstrated for generating loose-packed, low density monolayers, and some of them have demonstrated intercalative interactions. However, our system demonstrates advantages over each of these alternate methods.

One method for generating low-density SAMs is to use reduced-assembly times: immersing the gold substrates in thiolate solutions for ~30 seconds rather than the hours that are typically used to form a densely packed monolayer. This has been used by the Foster group to study the effect of packing density for hexadecyltrichlorosilane monolayers on protein adsorption to the surface,[34,35] and also by the Liu group to study the effect of packing density on electron-transfer kinetics of azobenzenethiol monolayers.[36] Although this method may be useful for demonstrating the dependence of certain monolayer properties on packing density, the lack of precise control over the spatial arrangement of adsorbate molecules makes this method less desirable for applications involving specific interactions between monolayers and target molecules.

Another method that demonstrated lower packing densities takes advantage of the "odd-even effect" that SAMs typically demonstrate. The Woll[37] group showed that changing the length of the aliphatic spacer group in biphenyl-*n* monolayers from *n* = odd to *n* = even was able to change surface spacing from 21.5 $Å^2$ to 27 $Å^2$. Although this is a significant increase in spacing considering the small changes in chemical structure, our method allows spacings of 65 $Å^2$ using our current, 1st generation spacer groups. This spacing allows greater steric freedom for intercalation, as well as the ability to tailor the spacing simply by changing end group chemistry, a property not allowed by exploitation of the odd-even effect.

Another method for generating low-density SAMs involves adsorption of amphiphiles with bulky thiol-containing headgroups and aliphatic tails (as opposed to our technique of using a bulky cleavable tailgroup moiety). The Lee group has used di- and tri-thiols[38-40] to achieve monolayers with greater surface spacings, but at ~25 $Å^2$ per molecule, the increases are still only moderate with this method.

Two other groups have used the bulky headgroup method with greater success, generating well-spaced monolayers and demonstrating intercalation of molecules into these monolayers. The first example of this was seen in 1990, when the Ward group[41] assembled imidazole-2-thione monolayers on gold with ~66 $Å^2$ spacings and observed intercalation of fluorinated aliphatic alcohols, as pictured in Figure 5.2. More recently, the Dong group has used thiolated-ring groups (e.g., thiophenes, mercaptophenyl carbazoles) as pictured in Figure 5.3 and demonstrated intercalation of surfactants and hydrophobic probes.[42,43-45]

This study aims to take advantage of the unique structure and properties of low-density self-assembled monolayers by assessing their capacity to capture or "intercalate" molecules from solution within the interstitial spaces between the thiolate. The intercalation concept is pictured in Figure 5.4. Although molecular intercalation has been demonstrated with some systems described above, a key advantage that our method has over these methods is the increased capacity for responsiveness to electrical potential. The greater coverage of the bulky headgroups over the substrate surface can act as an electrostatic shield, preventing the types of actively-driven conformational transitions that our system exhibits. Active control of intercalation and/or active expulsion of previously

intercalated molecules are capabilities that may dramatically increase the usefulness of our surfaces for biosensor or tissue engineering applications.

Considering these factors, we believe our method for generating low-density monolayers has the potential to become an effective approach for creating a dynamically responsive surface with precisely tunable density characteristics and which has the capacity for controllable intercalation of compatible target molecules.

We envision extending the technology of molecular intercalation in dynamically switchable surfaces towards two primary areas of application: (1) dynamic surfaces for cell adhesion studies, and (2) sensors for molecular disease markers. The following sections detail the case for these potential applications.

Dynamic surfaces for cell adhesion

Interactions between cells and the extracellular matrix (ECM) influence a variety of cellular functions such as adhesion, motility, proliferation, and differentiation.[46-49] The primary cell surface receptors that govern cell-matrix interactions are the integrins—a family of heterodimeric transmembrane proteins which adhere to ECM components such as fibronectin, laminin, and collagen.[50] The integrins form the physical link between the ECM outside of the cell and the cytoskeleton within the cell; when an activated integrin binds a matrix component, the cytoplasmic tail of the integrin binds a complex of cytoplasmic proteins (including talin, α-actinin, and vinculin) which then attaches to the termini of cytoskeletal actin filaments. The specialized regions of the cell's plasma membrane where these integrin-linked complexes are located and where contact with the ECM is made are called *focal adhesions*.

The specific epitopes of ECM proteins to which integrins bind can often be localized to very short peptide sequences,[51] the most widely studied being the Arg-Gly-Asp (RGD) sequence.[52] The RGD sequence in isolation can compete with intact matrix components such as fibronectin for cell surface binding sites. For this reason, the RGD sequence has been used in many cell-substrate interaction studies.

The most widely studied method of associating RGD peptides to surfaces involves covalently binding the peptides to polymer substrates. This method allows optimization of surface parameters that influence cell behavior—such as spacer length between the surface and the RGD sequence,[53,54] surface density of RGD,[55-57] and RGD surface distribution or clustering.[58,59] An alternate strategy is to rely on the self-assembly of amphiphilic RGD-containing amphiphiles to form cell-adhesive surfaces; Mrksich et al. have examined RGD-alkanethiol conjugates which self-assemble on gold substrates,[60] and Tirrell et al. have examined Langmuir-Blodgett deposition of lipid-conjugated RGD-peptides on surfaces.[61]

The advantage of self-assembly techniques for bioactive surface preparation is the high degree of organization of the interface afforded by self-assembly and the well-defined secondary and tertiary conformations that are achievable, allowing greater precision of presentation of ligands compared to covalent attachment techniques. The self-assembly based method of Mrksich, however, has the disadvantage of immobilizing the RGD peptides in a static arrangement on the surface, preventing the assessment of cellular remodeling of the substrate. The self-assembly method of Tirrell relies on the Langmuir-Blodgett technique, which requires specialized equipment and optimization of conditions to produce good films.

There is great potential in a self-assembly based system for the study of cell-substrate interactions which allows lateral mobility of RGD ligands, yet which involves a simple and robust means of substrate preparation. Low-density SAM technology can provide a unique platform for such studies. Intercalation of RGD-terminated lipids may simply require incubation of LDSAMs in solutions of lipopeptide. This may provide a system which exhibits RGD-presentation, mobility of RGDs, and simple and robust self-assembly, allowing study of ligand restructuring due to cell adhesion and focal adhesion formation.

Biosensors for molecular disease markers

In the last thirty years, the fight against breast cancer has made impressive strides in diagnosis and treatment. Although late-stage treatments continue to show higher and higher survival rates, early diagnosis remains essential to the fight against breast cancer. Table 1 shows data from the American Cancer Society for 5-year survival rates for breast cancer in different stages ranging from I (tumor size < 2 cm) to IV (metastatic tumors). Because of the clear importance of early detection, the American Cancer Society currently recommends that women over the age of 20 should have a clinical breast exam every three years and that women over the age of 40 should have a screening mammogram and a clinical breast exam every year.[62] Although these screening methods save thousands of lives each year, there are many more lives that could be saved. The American Cancer Society reports that the average number of women over the age of 40 that have had a mammogram within the past year is 60-65%, while the number having had both a mammogram and a clinical breast exam within the past year is 50-55%.[63] These numbers drop sharply to 37% and 31%, respectively, for those without health

insurance. There is thus much room for improvement for increasing the rate of early screening.

Although many important educational efforts are underway for increasing awareness of breast health and increasing the number of women who take breast exams and mammograms, technology has the potential to make a tremendous impact in early screening for breast cancer. The advent of a new type of screening test—one that is fast, easy-to-use, accurate, and inexpensive—could make it much easier for women of all demographics and economic classes to obtain screening.

There is strong demand to develop technology that could ultimately lead to a new breast cancer screening test—one which could potentially be performed in the home, eliminating the inconvenience of visiting the doctor's office in order to obtain initial screening. This would also provide much greater accessibility to initial screening for those without health insurance. The need for an effective and convenient option in addition to mammography and clinical breast exams is evident from the numbers of women who are not currently receiving adequate screening.

In terms of ease-of-use, the characteristic of greatest potential value for a screening test would be non-invasiveness—not requiring puncturing of the skin to take a blood sample. Potential non-invasive avenues would be to analyze the urine or the breath for biochemical markers which act as early indicators of breast cancer. N^1,N^{12}-diacetylspermine (DiAcSpm), which is excreted in urine, has recently been shown to act as a marker for early-stage breast cancer.[64] In this study, Hiramatsu et al. showed that DiAcSpm was even more predictive of breast cancer than widely studied blood-borne molecules such as CEA and CA15-3. They found increased levels of DiAcSpm in 28% of

early-stage breast cancer patients, whereas only 3% were CEA-positive and only 3% were CA15-3-positive. This is encouraging evidence for the use of DiAcSpm levels in urine to act as early-stage markers for breast cancer.

Volatile organic compounds (VOCs) in the breath have also recently been shown to act as markers for screening breast cancer. Philips et al.[65] showed that breath tests for C4-C20 alkanes and monomethylated alkanes act as markers of oxidative stress, which accompanies breast cancer. Analysis of breath samples was shown to have comparable predictive values to screening mammograms. This is also encouraging evidence for the use of alkanes in breath as early-stage markers for breast cancer.

The current methods used to analyze DiAcSpm in urine are high-performance liquid chromatography (HPLC) and enzyme-linked immunosorbent assay (ELISA). The current methods used to analyze oxidative stress markers in breath are gas chromatography (GC) and mass spectrometry (MS). All of these methods require sophisticated laboratory instrumentation, making them impractical for widespread public use.

Low-density SAMs represent a technology platform which may, with further development, provide the capability to analyze DiAcSpm in urine or markers of oxidative stress in breath in the form of an easy-to-use device. The markers that we are targeting are hydrophobic molecules. The unique structure of our low-density self-assembled monolayers provides a nanoporous structure that can potentially capture such hydrophobic target molecules, causing measurable changes in surface properties. Modification of the functional groups may allow customized selectivity to be engineered into the surfaces. The unique switching function of these surfaces can also potentially be

used to regenerate the sensor surface and confer re-usability to the device. The mono-molecular thickness of the sensor surface also yields the potential for part-per-million sensitivity. We thus see this technology platform as a potentially innovative solution to bringing convenient early screening to all women.

With such promising potential applications such as dynamic surfaces for cell adhesion studies and sensors for molecular disease markers, the phenomenon of molecular intercalation in low-density SAMs is a development that shows significant promise. In this study, we explore the chemistry of these interactions and the conditions under which they occur.

Experimental Section

Materials

Hexadecanethiol (HDT), undecanethiol (UDT), hexadecanoic acid (HDA), undecanoic acid (UDA), mercaptohexadecanoic acid (MHA), mercaptoundecanoic acid (MUA), triethylamine (TEA), diisopropylethylamine (DIPEA), and absolute ethanol were purchased from Sigma Aldrich (St. Louis, MO). Dimethoxytrityl chloride (DMT-Cl) and stearic acid were purchased from Fluka (St. Louis, MO). Chlorotrityl chloride (CT-Cl) was purchased from TCI America (Portland, OR). 18 MΩ-cm deionized water was produced using a Barnstead International (Dubuque, IA) E-pure system.

Synthesis

MHA or MUA was reacted with DMT-Cl and triethylamine (5:4:1 tetrahydrofuran : acetic acid : water, room temperature under argon, 14 hr) to form the thioethers MHA-DMT or MUA-DMT. After evaporation of the solvent, the product was

dissolved in ethyl ether and extracted with 1 M aqueous ammonium bicarbonate (3 x 30 ml) and washed with ethyl ether (3 x 30 ml). The extract was then purified by silica column chromatography (4:1:1 hexane:ethyl ether:THF) and evaporated, leaving an amber/yellow oil product.

MHA-DMT or MUA-DMT was then reacted with CT-Cl and DIPEA (methylene chloride, room temperature under argon, 14 hr). The product was then extracted with HCl in NaCl (3 x 30ml, with 3 x 30 ml wash with methylene chloride), 1 M aqueous ammonium bicarbonate (3 x 30 ml) and washed with ethyl ether (3 x 30 ml). The extract was then purified by silica column chromatography (4:1:1 hexane:ethyl ether:THF) and evaporated, leaving an amber/yellow oil product. DIPEA is removed by extraction using aqueous hydrochloric acid; unreacted MHA-DMT is removed by extraction using aqueous ammonium bicarbonate; and the aqueous phases are washed with methylene chloride. The solvent is evaporated to leave crude CT-MHA-DMT, which is purified by silica column chromatography (2.3 × 35 cm, 4:1 hexane:ethyl ether), leaving a dull yellow oil product.

The third reaction is that of CT-MHA-DMT with silver nitrate (1 hr, room temp, in 3:1 THF:methanol) then with dithioerythritol (DTE) (5 hr, room temp, in 3:1 THF:methanol). Silver nitrate oxidizes the thiol of MHA, displacing DMT, and DTE is used to release silver from CT-MHA and to precipitate excess silver nitrate. Precipitate is removed by centrifugation, and the product is extracted using ethyl acetate and water. The solvent is evaporated to leave crude CT-MHA, which is purified by silica column chromatography (2.3 × 35 cm, 1:1 hexane:ethyl ether), leaving a clear oil product.

SAM Preparation

Gold substrates were fabricated upon silicon wafers with a 4500 Å SiO_2 insulating layer, a 100 Å titanium adhesive layer, and a 1000 Å gold outer layer. A custom mask was developed to yield devices with a defined surface area for monolayer assembly (an electrical contacting zone allows connection of an electrical lead to the monolayer-assembly zone via a narrow conductive strip). The monolayer zone is of a defined surface area for controlled measurement of electrochemical parameters that scale with surface area. Gold substrates were rinsed with a sequence of absolute ethanol, and absolute ethanol and then dried under a stream of N_2 prior to SAM preparation. Root mean square roughness of gold surfaces has been determined by atomic force microscopy to be <2 nm, providing an ultra-flat surface for monolayer assembly.

SAMs were prepared by immersion of substrates in 1 mM adsorbate in absolute ethanol, typically 16+ hours unless otherwise indicated. Monolayers are then rinsed with a sequence of absolute ethanol, and absolute ethanol and then dried under a stream of N_2. Low-density monolayers are produced by formation of a CT-MHA monolayer, followed by cleavage of the chlorotrityl groups by incubation in 50% trifluoroacetic acid in ethanol for 2 minutes, followed by ethanol-water-ethanol rinse and N_2 drying. Intercalated monolayers are produced by incubation of low-density monolayers in 1 mM solutions of target molecule (stearic acid or octadecyl rhodamine) in 65:35 ethanol:water (to encourage hydrophobic interactions between intercalates and monolayers while maintaining intercalate solubility).

Instrumentation

Electrochemical Impedance Spectroscopy (EIS) is a surface-sensitive analytical technique which can discriminate between different conformational states of molecules

self-assembled on surfaces and their impact on the permeability of the monolayer.[66] We use EIS to study barrier properties of the low density SAMs with and without intercalated molecules, detecting increases in monolayer capacitance due to accumulation of intercalated molecules within the monolayers. A small amplitude (≤ 10 mV) sinusoidal AC potential, superimposed upon a fixed DC potential, is applied to the sample within a standard, 3-electrode electrochemical cell (monolayer sample as working electrode, Standard Calomel Electrode [SCE] as reference electrode, and platinum mesh as counter electrode). The electrolyte solution is phosphate buffered saline (PBS) (to approximate physiological conditions). The potentiostat is a Gamry PCI4/300 controlled by the EIS300 software module. DC potentials can be varied to study charge effects on monolayer structure and properties. AC potential frequencies range from 1 to 10^5 Hz, and amplitude and phase data are collected at 10 points per decade. The time-variant potential allows stimulation and measurement of displacement currents and thus monolayer capacitance. The small-amplitude sinusoidal modulation also ensures linearity of the cell's voltage-current response, allowing simplified data analysis and modeling of equivalent circuits. The resulting current response will vary for different surface states (with and without intercalated molecules).

Reflection-Absorption Infrared Spectroscopy (RAIRS) is used to determine the presence of chemical functional groups on surfaces. Spectra were obtained with a Thermo Nicolet 4600 instrument with a 16 mm aperture, 64 scans per sample at 4 nm resolution.

Ellipsometry/SPR analysis of the samples was performed using a Nanofilm EP3 nulling ellipsometer with a wavelength of 532 nm, angle of incidence of 60°, and polarizer range of 4°.

Results and Discussion

As an indication of the successful preparation of low-density SAMs, Figure 5.5 shows IR spectra before and after cleavage of the space filling chlorotrityl end group. The shift in the carbonyl peak at ~1700 cm^{-1} and the disappearance of the characteristic C-Cl peak at 1153 cm^{-1} indicates cleavage and formation of the low density monolayer.

The distinctions that electrochemical impedance spectroscopy can draw between relatively subtle differences in monolayer structure are represented in Figure 5.6, which shows Bode impedance modulus plots comparing monolayer density, tailgroup functionality and chain length. At lower frequencies (<1000 Hz), the contribution of the impedance due to monolayer capacitance dominates that of the electrolyte solution resistance, and vice versa at high frequencies (>1000 hz). High density monolayers exhibit greater impedance than low density monolayers, due to increased coverage of the electrode area and reduced surface area for current transfer. Methyl-terminated monolayers show greater impedance than carboxyl-terminated monolayers, due to greater hydrophobicity and reduced penetration of charge-carrying solution ions. C16 chain length monolayers show greater impedance than C11 chain length monolayers, due to greater crystallinity and ordering of the hydrophobic aliphatic chains, which likewise provides a greater insulative barrier.

The effect that intercalation has on monolayer impedance is shown in Figures 5.6, 5.7, and 5.8. Low density monolayers were incubated in 1 mM solutions of either stearic

acid or octadecyl rhodamine in 65:35 ethanol:water overnight. Figure 5.6 shows the results for incubation of a low-density SAM of MHA in stearic acid solution, Figure 5.7 shows the results for incubation of a low-density SAM of MHA in octadecyl rhodamine solution, and Figure 5.8 shows the results for incubation of a low-density SAM of MUA (shorter chain length) in stearic acid solution. High-density and low-density SAMs stored overnight in ethanol are included as controls. Incubation in the analyte solution in each case increases the Nyquist plot modulus (line height) and phase angle (line steepness). This indicates intercalation of molecules into the monolayers due to blockage of electrode area by the fatty acids and a transition from the looser structure of the low density monolayers to a more highly ordered structure characteristic of high density monolayers. High density monolayer controls show the highest impedance, low density monolayer controls show the lowest impedance, and intercalated monolayers show an intermediate impedance.

If the impedance of high-density SAMs is also changes after incubation in analyte solutions, then it could be concluded that non-intercalative interactions are responsible for the observed shifts in monolayer permeability. However, Figures 5.9 and 5.10 show that incubation of high density SAMs in stearic acid solution does not alter their measured impedance. Figure 5.9 shows the results for incubation of a high-density SAM of MHA in stearic acid solution, and Figure 5.10 shows the results for incubation of a high-density SAM of MUA in stearic acid solution. The tightly-packed structure of high-density SAMs does not allow the penetration of analyte molecules exhibited by the low-density systems.

Intercalation of analyte molecules into low-density SAMs should lead to increased restriction of chain conformations, leading to a shift from a more fluid structure to a more tightly-packed structure. Figure 5.11 shows IR spectra comparing high density and low density reference monolayers versus a low-density monolayer with incubated in stearic acid. Intercalation of stearic acid within the low-density monolayer results in asymmetric and symmetric -CH_2- stretch peaks that are shifted towards the characteristic wavenumbers of high density monolayers and away from those of low density monolayers. This indicates that intercalation causes a low-density SAM to assume a more tightly packed structure as a result of increased occupation of the intersticial spaces in the monolayer.

In order to better understand the kinetics of the intercalation process, we performed a time-course study on the intercalation of stearic acid in a low-density MHA SAM. Figure 5.12 shows that impedance increases steadily with time until about 7 h. Equilibrium thus takes a significant amount of time to be reached—a time scale similar to that for the organization of the alkyl chains during self-assembly of a high density SAM. The conformational freedom inherent in the low density monolayer system may dictate such extended equilibration times for full intercalation of analyte molecules.

We next addressed the influence of solvent on the intercalation process. Figure 5.13 shows the affect of applied positive potential of +400 mV on monolayer impedance phase angle for a low-density SAM. The deviation of the phase angle at low-frequencies is indicative of the increase in electrochemical permeability of the SAM as a result of the applied potential. This effect is not experienced by a low-density MHA monolayer that is incubated in MHA solution in order to backfill the intersticial spaces, shown in Figure

5.14. In this case, there is much less conformational freedom to allow for changes in structure for a tightly packed monolayer. These data are shown as reference to illustrate the influence that the external solvent has on analyte intercalation. Figures 5.15, 5.16, and 5.17 show the response to applied potential of low-density SAMs incubated in 1 mM stearic acid solutions prepared with different solvents. The results shown in Figure 5.15 were for 1 mM stearic acid in ethanol. The results shown in Figure 5.16 were for 1 mM stearic acid in 2:1 ethanol:water. The results shown in Figure 5.17 were for 1 mM stearic acid in 1:1 ethanol:water. We see that as the solvent becomes more polar, there is less responsiveness to applied potential, indicating greater levels of intercalation. This is understandable because there should be a greater driving force for transfer of the hydrophobic tails of the analyte molecules out of an polar solvent and into the low-density SAMs.

Another method for assessing intercalation is observation of changes in the surface plasmon resonance signal, which is sensitive to the binding of analytes to a surface. Figure 5.18a shows a schematic picture of a patterned surface with low-density SAM regions within a high-density SAM background. This surface is produced by microcontact printing the MHA chlorotrityl ester precursor molecule onto a gold surface using a PDMS stamp. The surface is then incubated in a solution of MHA to backfill the unpatterned regions with high density SAM. The surface is then incubated in trifluoroacetic acid to cleave the chlorotrityl groups to leave low-density SAMs in the patterned region. Figure 5.18b shows an imaging ellipsometry picture of this surface, with darker regions indicating greater film thickness of the high-density regions and lighter regions indicating lower film thickness of the low-density regions. Figure 19

shows the changes in surface plasmon resonance experienced by the patterned surface when exposed in flow-through mode to a 1 mM stearic acid solution in 65:35 ethanol:water. When the stearic acid is introduced, the SPR signal in the low-density region increases, whereas the high-density region signal does not. Subsequent washing with the ethanol/water solution leads to a decrease in SPR signal in the low-density region, suggesting that the intercalated molecules are washed away as a result.

Conclusions

Intercalation of fatty acids (stearic and palmitic acid) and octadecyl rhodamine within low density monolayers has been demonstrated by electrochemical impedance spectroscopy, infrared spectroscopy, and surface plasmon resonance spectroscopy. A time-course study of intercalation shows that a steady increase of impedance accompanies intercalation of stearic acid until about 7 hours, when equilibrium is reached. The influence of external solvent on intercalation was also assessed, with more polar solvents promoting greater levels of intercalation.

Acknowledgment

D.K.P. acknowledges support from a graduate fellowship from the National Institutes of Health through the University of Michigan Cellular Biotechnology Training Program. This project was funded by grants from the National Institutes of Health (5 R21 EB005732-02) and the Department of Defense (Idea award, W81XWH-06-1-0271).

Figures

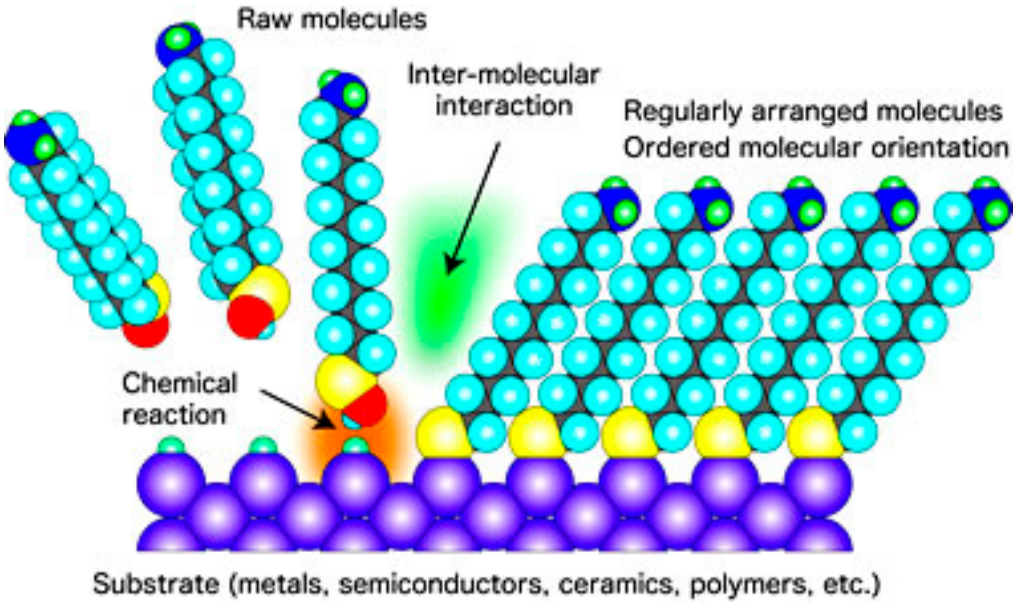

Nanoscopic Surface Architecture Lab, Kyoto University

Nanoscopic Surface Architecture Lab, Kyoto University

Figure 5.1. Schematic illustration of high-density self-assembled monolayer.

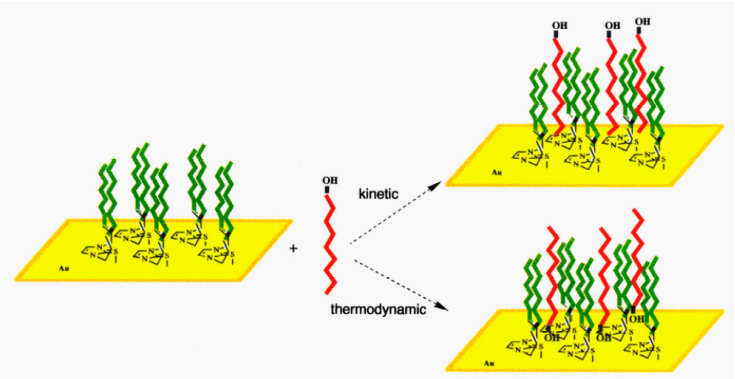

Figure 5.2. Ward[41] method for creating intercalating SAMs.

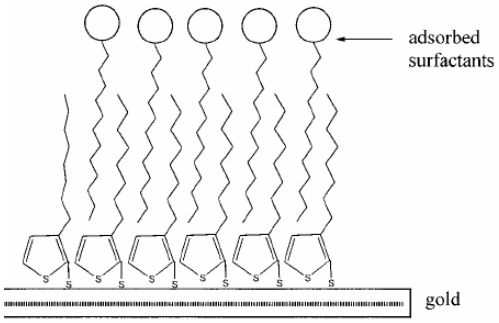

Figure 5.3. Dong[43] method for creating intercalating SAMs.

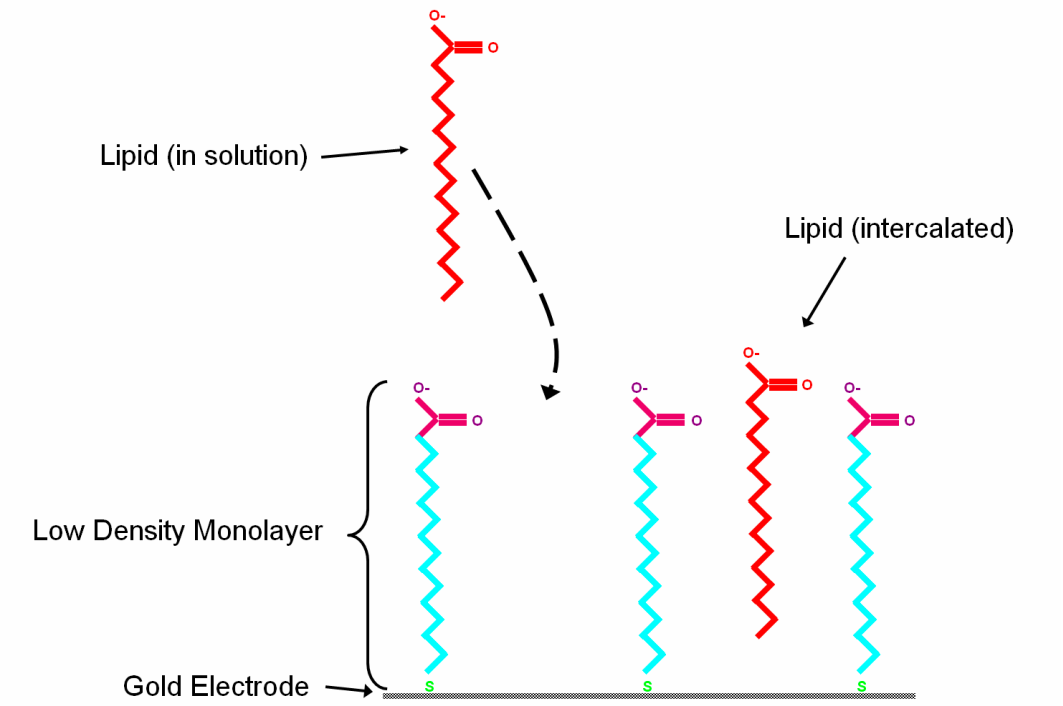

Figure 5.4. Illustration of intercalation concept.

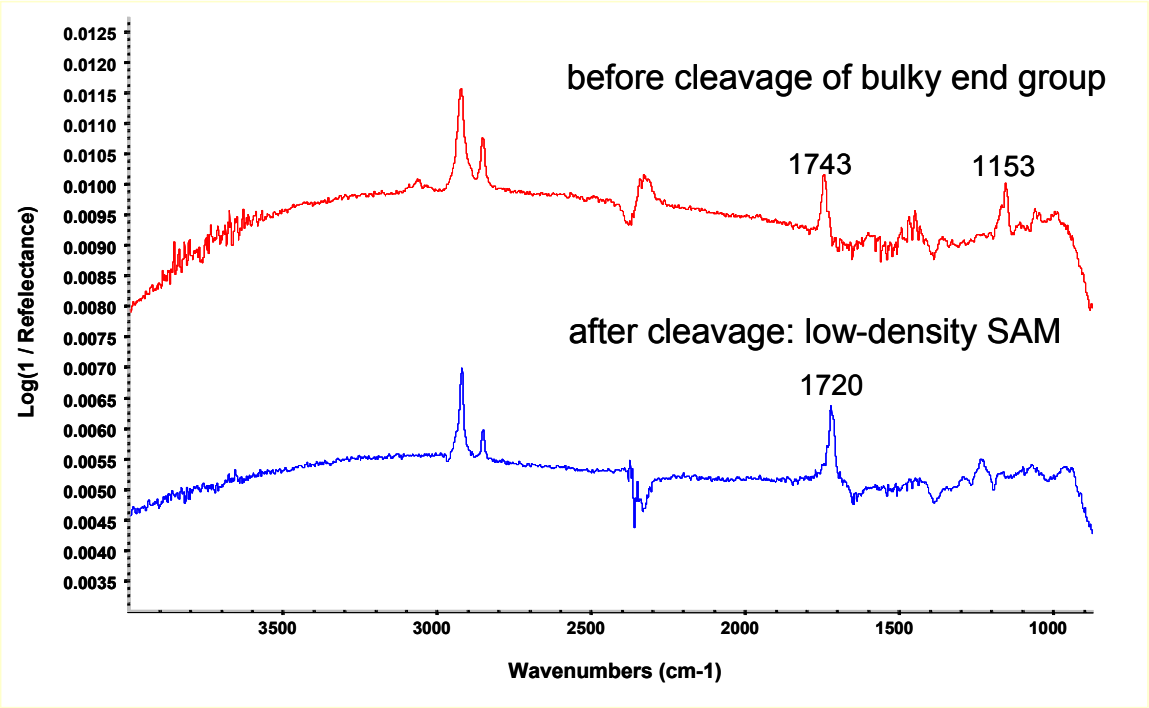

Figure 5.5. FTIR spectra of CT-MHA and low-density MHA SAMs.

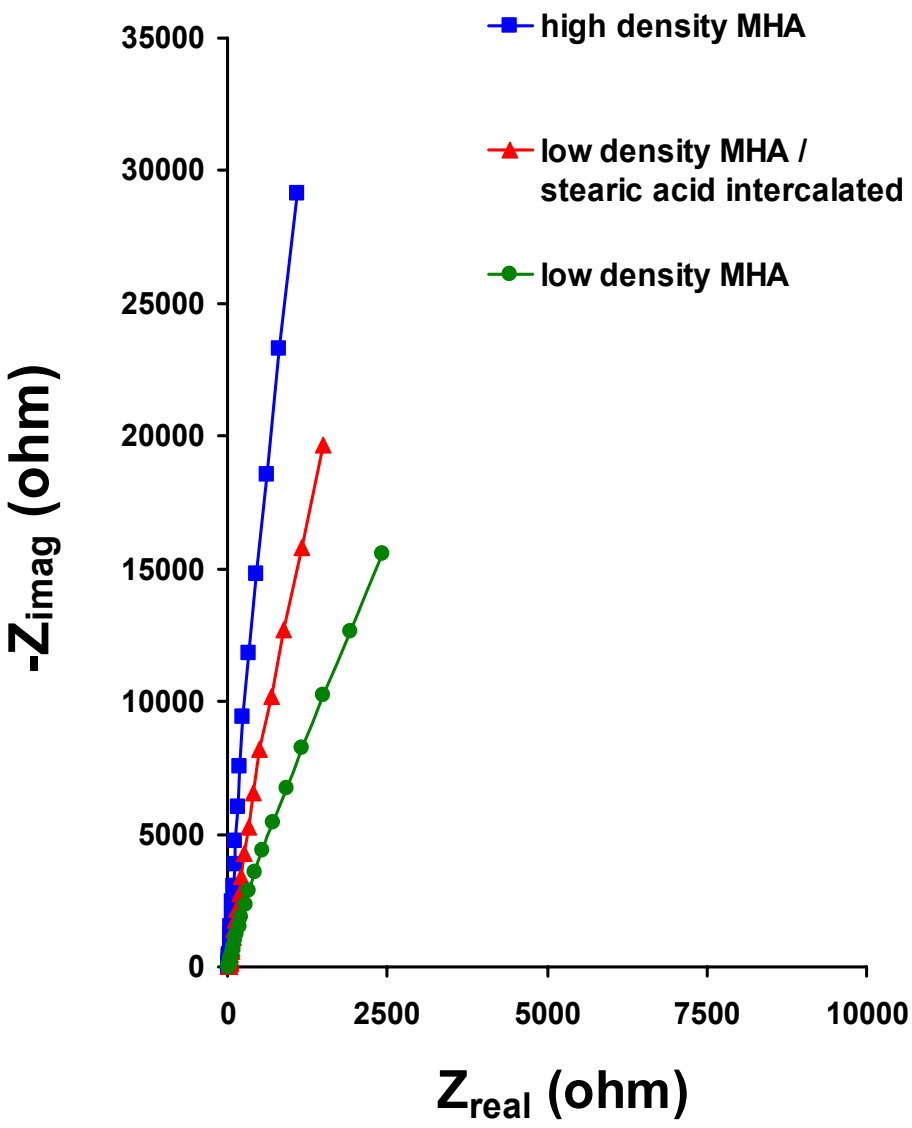

Figure 5.6. Nyquist impedance plots of MHA monolayers: high-density, low-density, and low-density incubated in stearic acid.

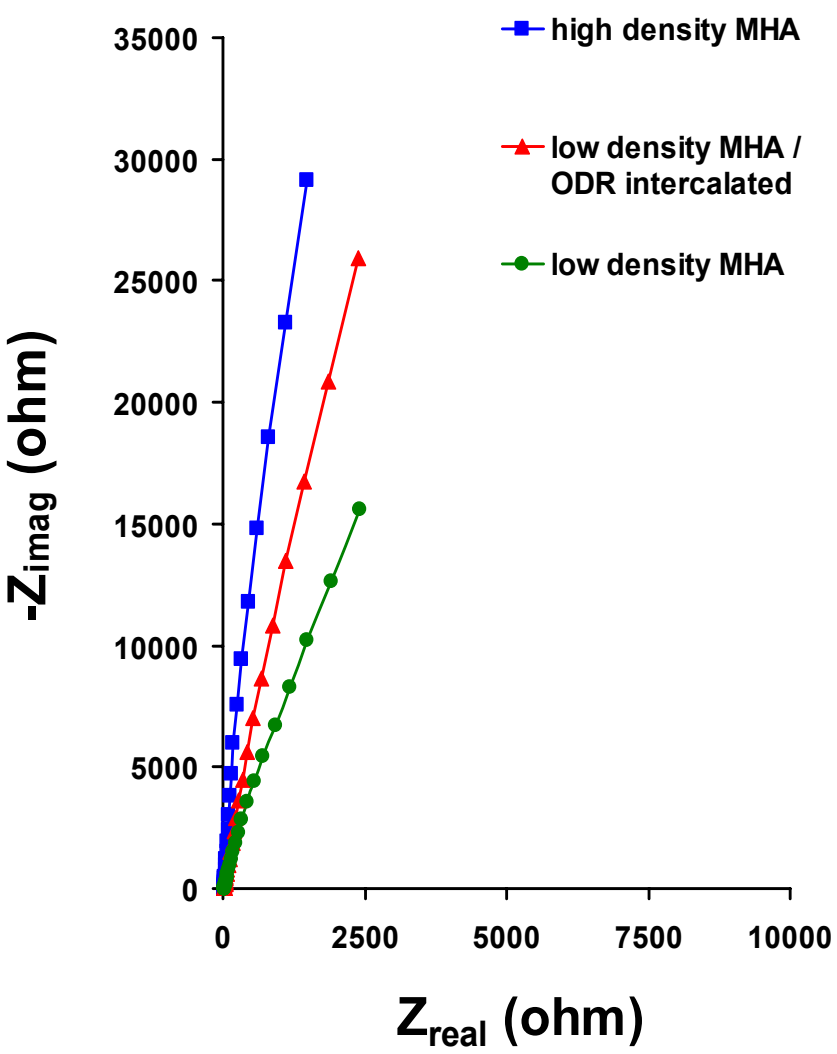

Figure 5.7. Nyquist impedance plots of MHA monolayers: high-density, low-density, and low-density incubated in octadecyl rhodamine.

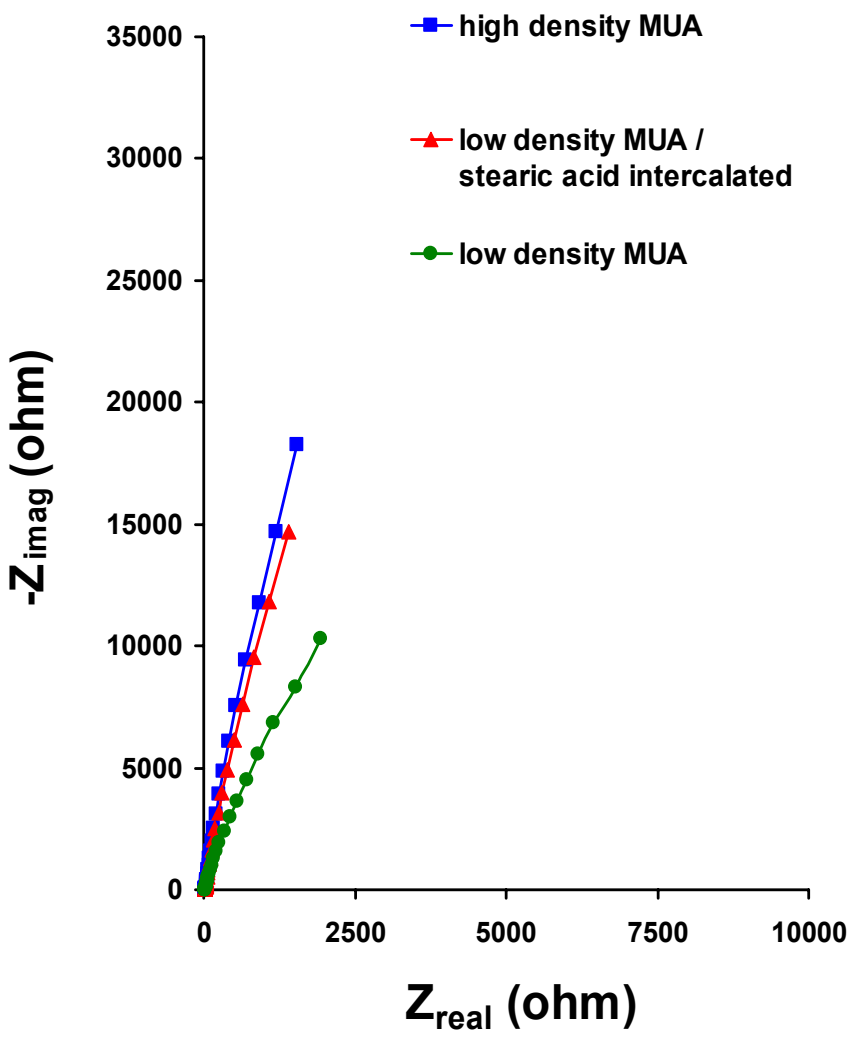

Figure 5.8. Nyquist impedance plots of MUA monolayers: high-density, low-density, and low-density incubated in stearic acid.

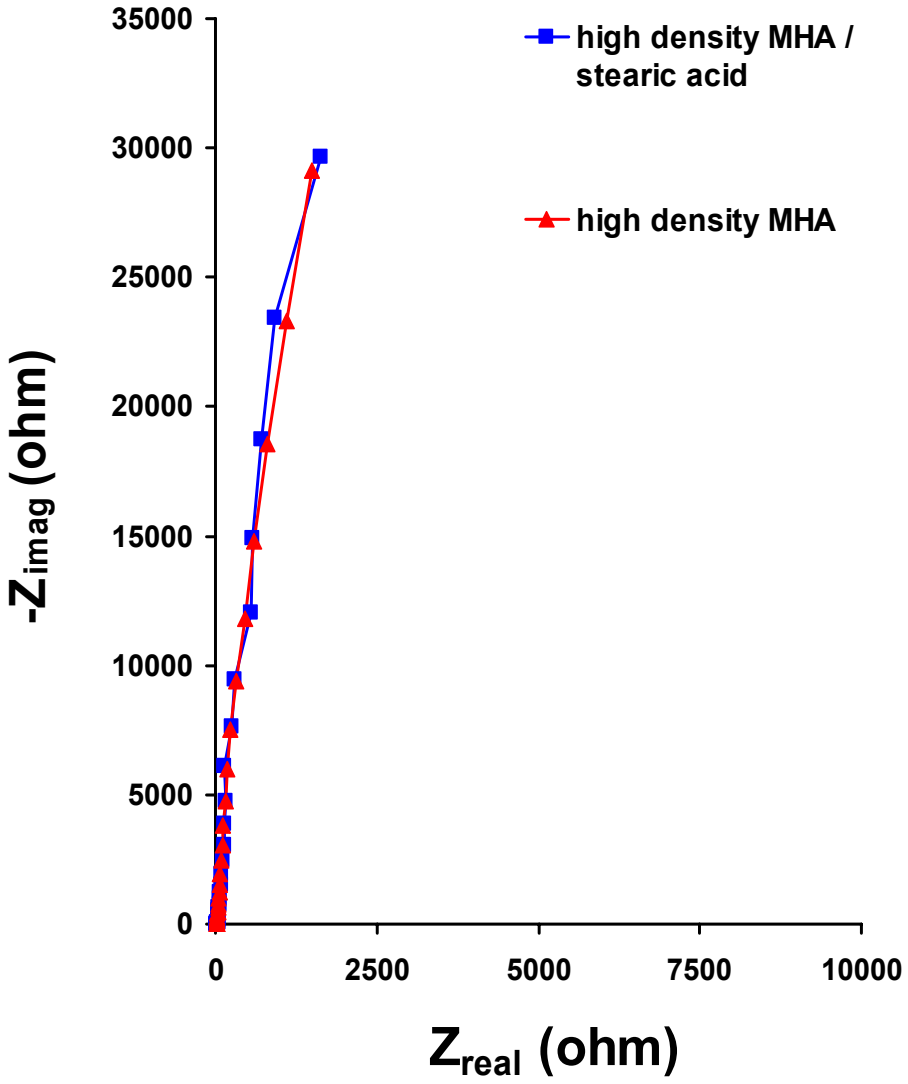

Figure 5.9. Nyquist impedance plots of MHA monolayers: high density and high density incubated in stearic acid.

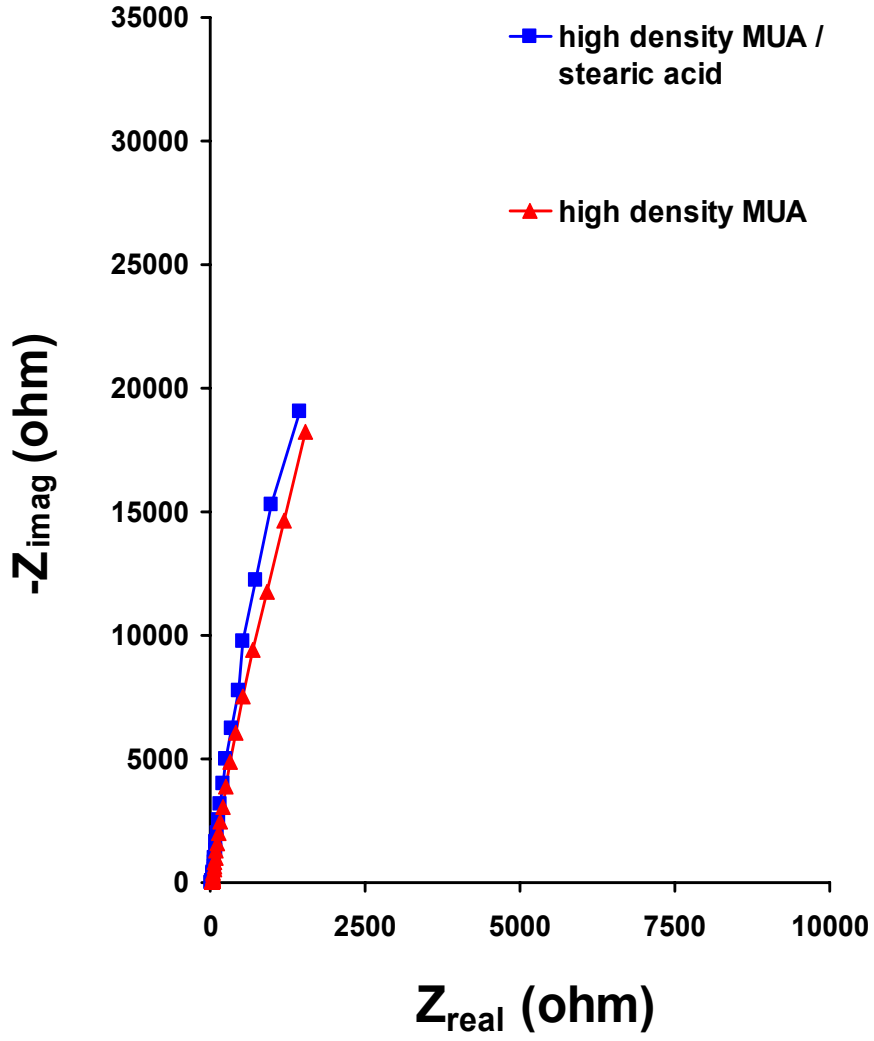

Figure 5.10. Nyquist impedance plots of MUA monolayers: high density and high density incubated in stearic acid.

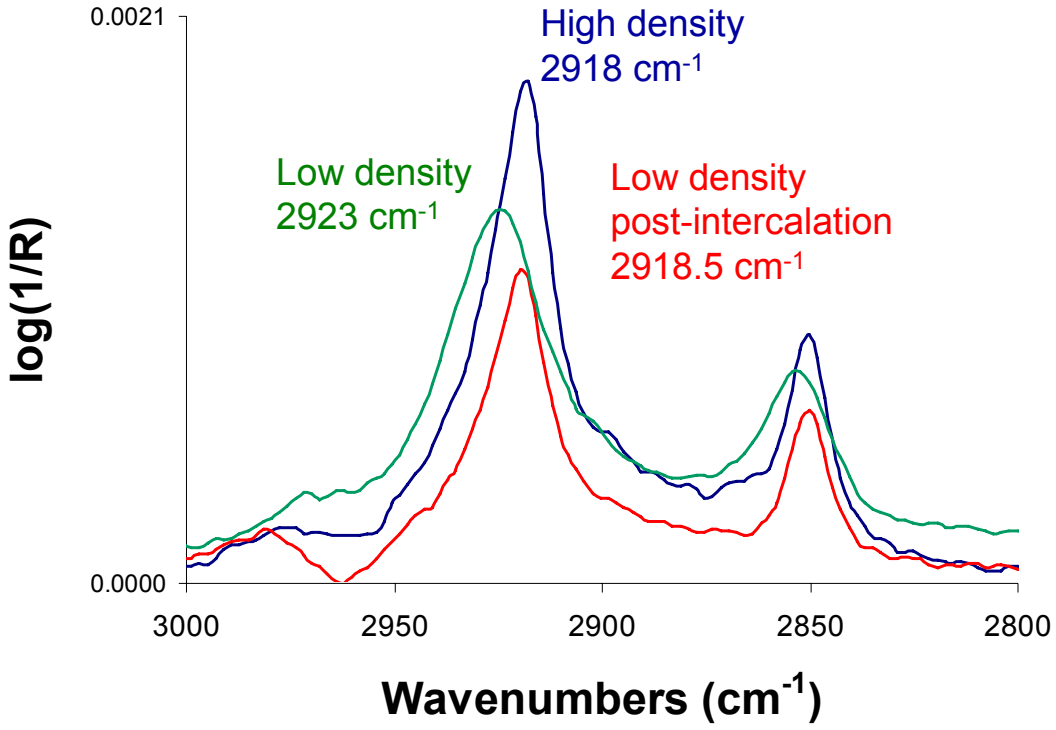

Figure 5.11. FTIR spectra demonstrating effect of intercalation on monolayer structure.

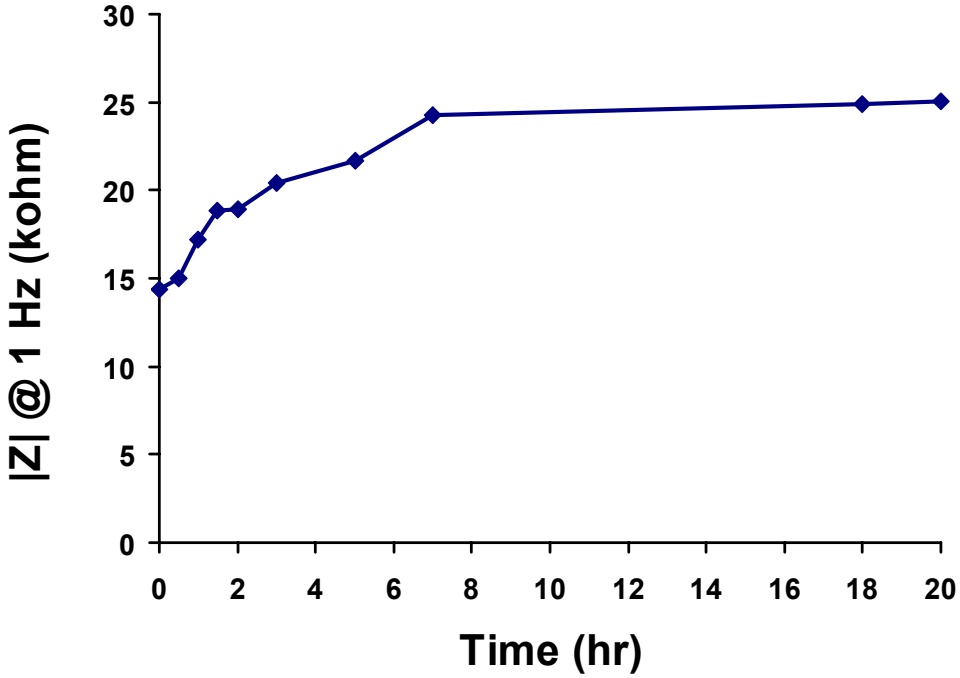

Figure 5.12. Time-course evaluation of intercalation of low-density MHA in 1 mM stearic acid.

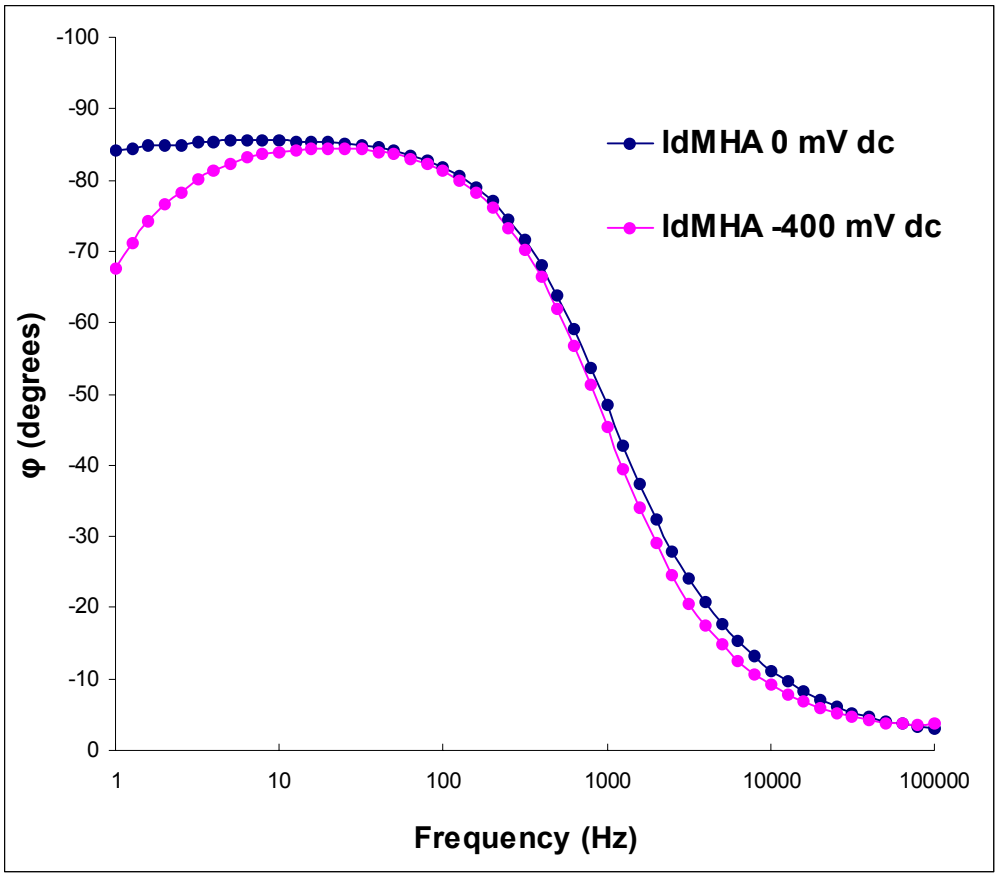

Figure 5.13. Effect of applied potential on impedance phase angle of low-density MHA.

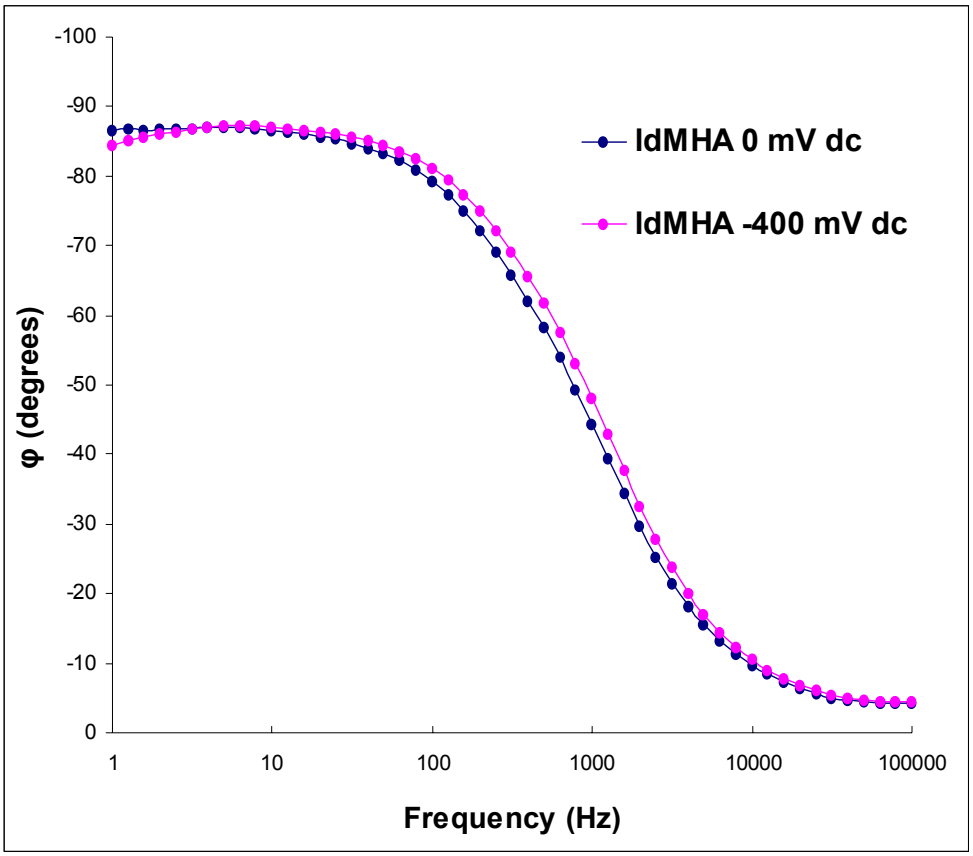

Figure 5.14. Effect of applied potential on impedance phase angle of low-density MHA backfilled with MHA.

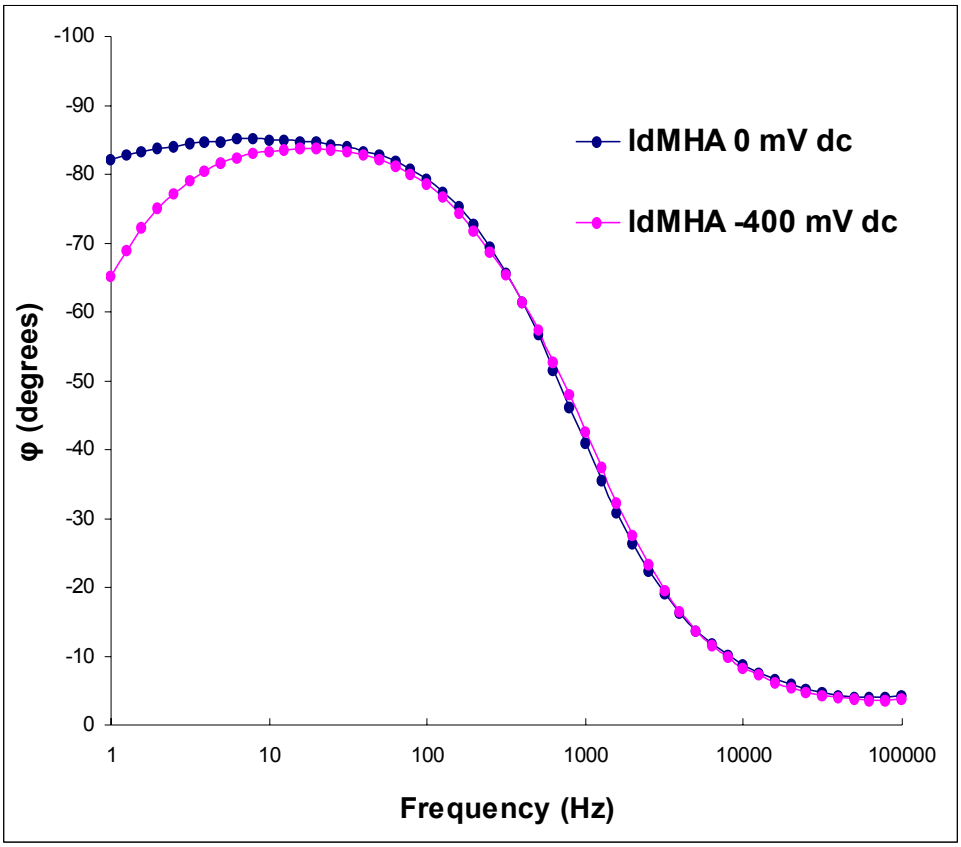

Figure 5.15. Effect of applied potential on impedance phase angle of low-density MHA incubated in 1 mM stearic acid dissolved in ethanol.

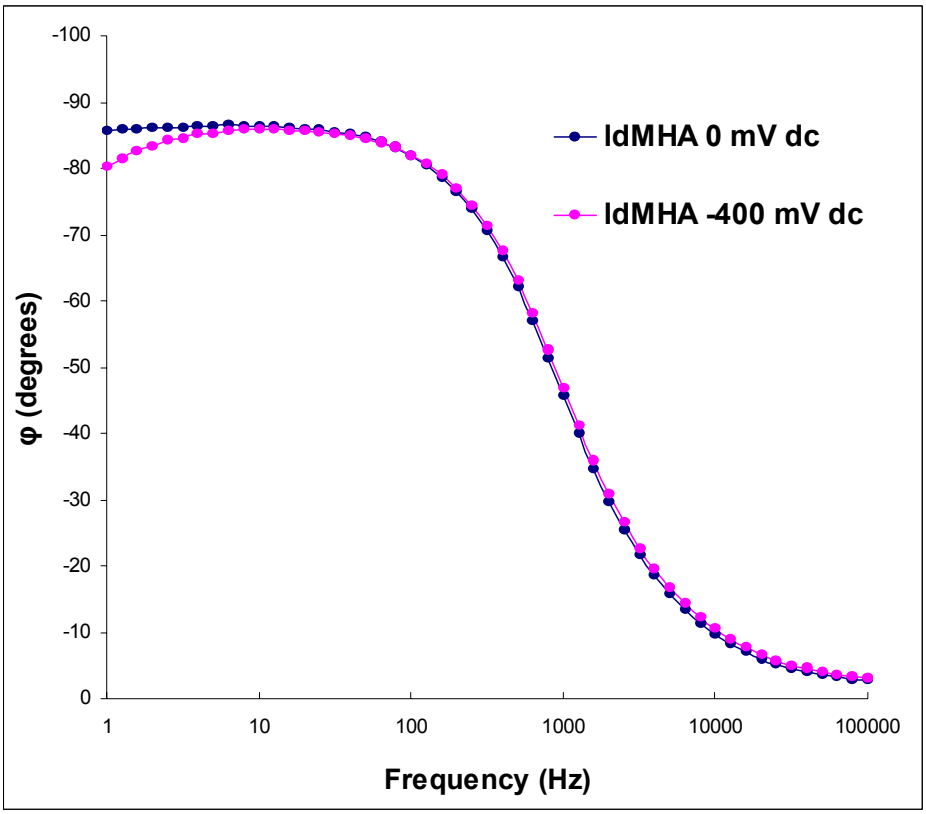

Figure 5.16. Effect of applied potential on impedance phase angle of low-density MHA incubated in 1 mM stearic acid dissolved in 2:1 ethanol:water.

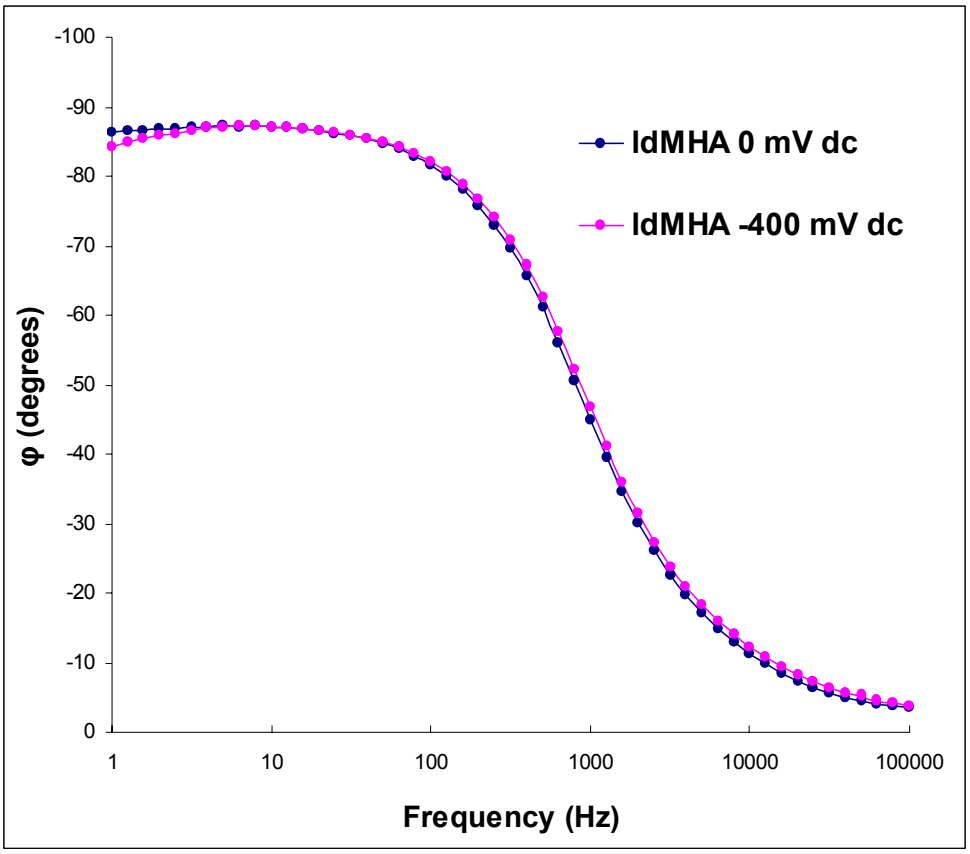

Figure 5.17. Effect of applied potential on impedance phase angle of low-density MHA incubated in 1 mM stearic acid dissolved in 1:1 ethanol:water.

(a)

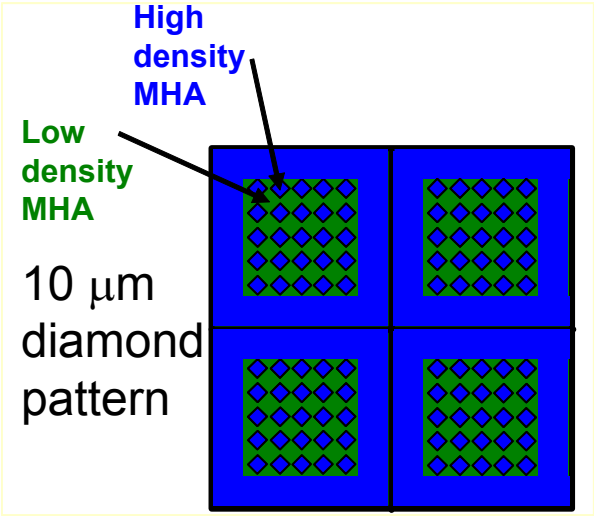

(b)

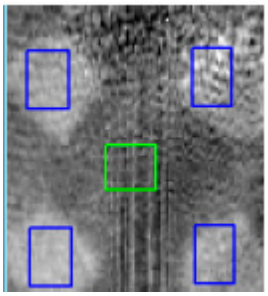

Figure 5.18. (a) Schematic illustration of a patterned surface with low-density SAM regions within a high-density SAM background (b) imaging ellipsometry picture of the prepared surface.

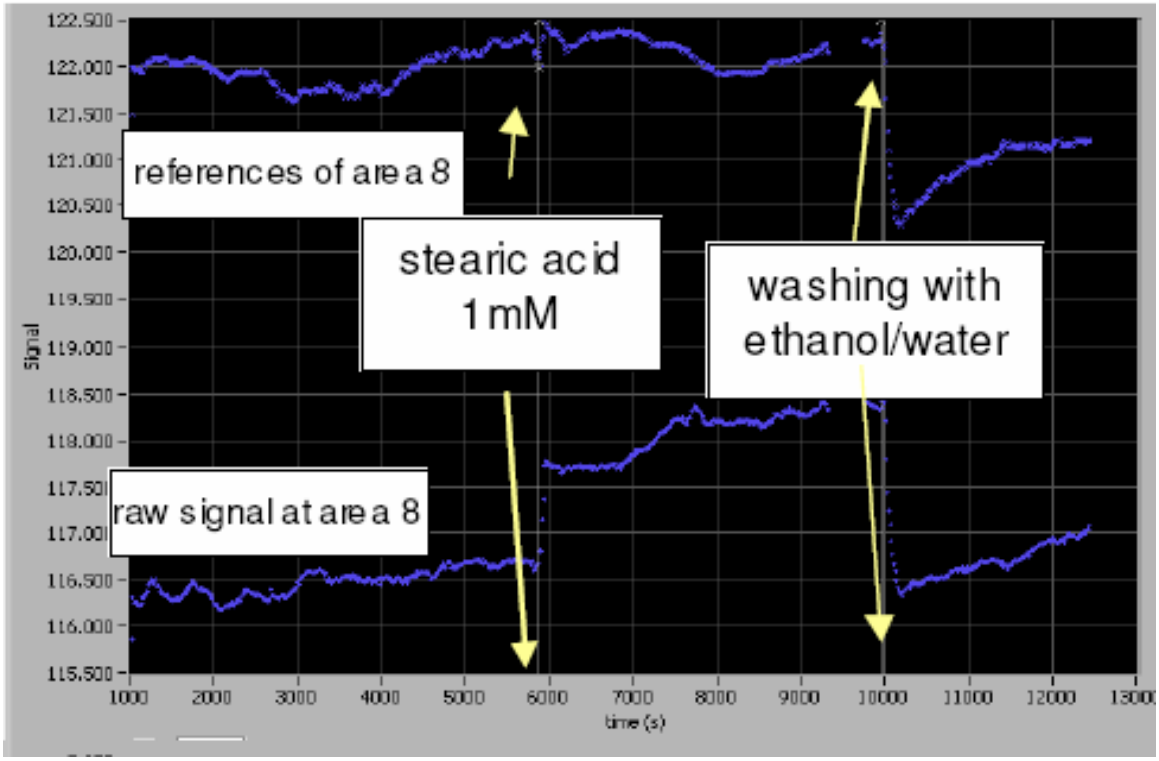

Figure 5.19. Changes in surface plasmon resonance experienced by the patterned surface when exposed in flow-through mode to a 1 mM stearic acid solution in 65:35 ethanol:water. Bottom line represents low-density intercalation-susceptible region. Top line represents high-density control region.

References

(1) Love, J.C.; Estroff, L.A.; Kriebel, J.K.; Nuzzo, R.G.; Whitesides, G.M. *Chemical Reviews* **2005**, *105*, 1103-1169.

(2) Schreiber, F. *Progress in Surface Science* **2000**, *65*, 151-256.

(3) Ulman, A. *Chem. Rev.* **1996**, *96*, 1533-1554.

(4) Dubois, L.H.; Nuzzo RG. *Annu. Rev. Phys. Chem.* **1992**, *43*, 437-63.

(5) Schwartz, D.K. *Annu. Rev. Phys. Chem.* **1991**, *52*, 107-37.

(6) Badia, A.; Lennox, R.B.; Reven, L. *Accounts of Chemical Research* **2000**, *33*, 475-481.

(7) Sandhyarani, N.; Pradeep, T. *International Reviews in Physical Chemistry* **2003**, *22*, 221-262.

(8) Delamarche, E.; Michel, B. *Thin Solid Films* **1996**, *273*, 48-53.

(9) Zharnikov, M.; Grunze, M. *Journal of Physics: Condensed Matter* **2001**, *13*, 11333-11365.

(10) Duwez, A.S. *Journal of Electron Spectroscopy and Related Phenomena* **2004**, *134*, 97-138.

(11) Li, X.M.; Huskens, J.; Reinhoudt, D.N. *Journal of Materials Chemistry* **2004**, *14*, 2954-2971.

(12) Sullivan, T.P.; Huck, W.T.S. *European Journal of Organic Chemistry* **2003**, *1*, 17-29.

(13) Chechik, V.; Crooks, R.M.; Stirling, C.J.M. *Advanced Materials* **2000**, *12*, 1161-1171.

(14) Smith, R.K.; Lewis, P.A.; Weiss, P.S. *Progress in Surface Science* **2004**, *75*, 1-68.

(15) Wilbur, J.L.; Kumar, A.; Biebuyck, H.A.; Kim, E.; Whitesides, G.M. *Nanotechnology* **1996**, *7*, 452-457.

(16) Kraemer, S.; Fuierer, R.R.; Gorman, C.B. *Chemical Reviews* **2003**, *103*, 4367-4418.

(17) Liu, G.Y.; Xu, S.; Qian, Y. *Accounts of Chemical Research* **2000**, *33*, 457-466.

(18) Xia, Y.; Zhao, X.M.; Whitesides, G.M. *Microelectronic Engineering* **1996**, *32*, 255-268.

(19) Wirth, M.J.; Fairbank, R.W.P.; Fatunmbi, H.O. *Science* **1997**, *275*, 44-47.

(20) Flink, S.; van Veggel, F.C.J.M.; Reinhoudt, D.N. *Sensors Update* **2001**, *8*, 3-19.

(21) Flink, S.; van Veggel, F.C.J.M; Reinhoudt, D.N. *Advanced Materials* **2000**, *12*, 1315-1328.

(22) Schon, J.H.; Meng, H.; Bao, Z. *Nature* **2001**, *413*, 713-716.

(23) Vuillaume, D. *J. Nanosci. Nanotechnol*. **2002**, *2*, 267-79.

(24) Mirsky, V.M. *Trends in Analytical Chemistry* **2002**, *21*, 439-450.

(25) Vijayamohanan, K.; Aslam, M. *Applied Biochemistry and Biotechnology* **2001**, *96*, 25-39.

(26) Chaki, N.K.; Vijayamohanan, K. *Biosensors and Bioelectronics* **2002**, *17*, 1-12.

(27) Wink, T.; van Zuilen, S.J.; Bult, A.; van Bennkom, W.P. *Analyst* **1997**, *122*, 43R-50R.

(28) Ferretti, S.; Paynter, S.; Russell, D.A.; Sapsford, K.E.; Richardson, D.J. *Trends in Analytical Chemistry* **2000**, *19*, 530-540.

(29) Ostuni, E.; Yan, L.; Whitesides, G.M. *Colloids and Surfaces, B: Biointerfaces* **1999**, *15*, 3-30.

(30) Schaeferling, M.; Schiller, S.; Paul, H.; Kruschina, M.; Pavlickova, P.; Meerkamp, M.; Giammasi, C.; Kambhampati, D. *Electrophoresis* **2002**, *23*, 3097-3105.

(31) Chen, C.S.; Ostuni, E.; Whitesides, G.M.; Ingber, D.E. *Methods in molecular biology* **2000**, *139* 209-19.

(32) Plant, A.L. *Langmuir* **1993**, *9*, 2764-2767.

(33) Meuse, C.W.; Niaura, G.; Lewis, M.L.; Plant, A.L. *Langmuir* **1998**, *14*, 1604-1611.

(34) Choi, E.J.; Foster, M.D.; Daly, S.; Tilton, R.; Przybycien, T.; Majkrzak, C.F.; Witte, P.; Menzel, H. *Langmuir* **2003**, *19*, 5464-6474.

(35) Petrash, S.; Cregger, T.; Zhao, B.; Pokidysheva, E.; Foster, M.D.; Brittain, W.J.; Sevastianov, V.; Majkrzak, C.F. *Langmuir* **2001**, *17*, 7645-7651.

(36) Shao, H.B.; Yu, H.Z.; Zhao, J.W.; Zhang, H.L.; Liu, Z.F. *Chemistry Letters* **1997**, 749-750.

(37) Azzam, W.; Cyganik, P.; Witte, G.; Buck, M.; Woll, C. *Langmuir* **2003**, *19*, 8262-8270.

(38) Shon, Y.S.; Colorado, R.; Williams, C.T.; Bain, C.D.; Lee, T.R. *Langmuir* **2000**, *16*, 541-548.

(39) Park, J.S.; Smith, A.C.; Lee, T.R.. *Langmuir* **2004**, *20*, 5829-5836.

(40) Park, J.S.; Vo, A.N.; Barriet, D.; Shon, Y.S.; Lee, T.R. *Langmuir* **2005**, *21*, 2902-2911.

(41) Arduengo, A.J.; Moran, J.R.; Rodriguez-Parada, J.; Ward, M.D. *J. Am. Chem. Soc.* **1990**, *112*, 6153-6154.

(42) Bao, H.F.; Peng, Z.Q.; Wang, E.K.; Dong, S.J. *Langmuir* **2004**, *20*, 10992-10997.

(43) Peng, Z.Q.; Dong, S.J. *Langmuir* **2001**, *17*, 4904-4909.

(44) Peng, Z.Q.; Wang, J.G.; Wang, E.K.; Dong, S.J. *Journal of the Electrochemical Society* **2003**, *150*, E197-E201.

(45) Cheng, W.L.; Han, X.J.; Wang, E.K.; Dong, S.J. *Electroanalysis* **2004**, *16*, 127-131.

(46) Chen, C.S.; Mrksich, M.; Huang, S.; Whitesides, G.M.; Ingber, D.E. *Science* **1997**, *276*, 1425-1428.

(47) Davey, G.; Buzzai, M.; Assoian, R.K. *J. Cell Sci.* **1999**, *112*, 4663-4672.

(48) Huttenlocher, A.; Ginsberg, M.H.; Horwitz, A.F. *J. Cell Biol.* **1996**, *134*,1551-1562.

(49) Palacek, S.P.; Loftus, J.C.; Ginsberg, M.H.; Lauffenburger, D.A.; Horwitz, A.F. *Nature* **1997**, *385*, 537-540.

(50) Hynes, R.O. *Cell* **1992**, *69*, 11-25.

(51) Pierschbacher, M.D.; Ruoslahti, E. *Nature* **1984**, *309*, 30-33.

(52) Ruoslahti, E. *Annu. Rev. Cell Dev. Biol.* **1996**, *12*, 697-715.

(53) Craig, W.S.; Cheng, S.; Mullen, D.G.; Blevitt, J.; Pierschbacher, M.D. *Biopolymers* **1995**, *37*, 157-175.

(54) Beer, J.H.; Springer, K.T.; Coller, B.S. *Blood* **1992**, *79*, 117-28.

(55) Neff, J.A.; Tresco, P.A.; Caldwell, K.D. *Biomaterials* **1999**, *20*, 2377-93.

(56) Kantlehner, M.; Schaffner, P.; Finsinger, D.; Meyer, J.; Jonczyk, A.; Diefenbach, B.; Nies, B.; Holzemann, G.; Goodman, S.L.; Kessler, H. *ChemBioChem* **2000**, *1*, 107-14.

(57) Mann, B.K.; West, J.L. *J. Biomed. Mater. Res.* **2002**, *60*, 86-93.

(58) Meheshwari, G.; Brown, G.; Lauffenburger, D.A.; Wells, A.; Griffith, L.G. *J. Cell Sci.* **2000**, *113*, 1677-1686.

(59) Irvine, D.J.; Mayes, A.M.; Griffith, L.G. *Biomacromolecules* **2001**, *2*, 85-94.

(60) Houseman, B.T.; Mrksich, M. *Biomaterials* **2001**, *22*, 943-955.

(61) Pakalns, T.; Haverstcik, K.L.; Fields, G.B.; McCarthy, J.B.; Mooradian, D.L.; Tirrell, M. *Biomaterials* **1999**, *20*, 2265-2279.

(62) Smith, R.A.; Saslow, D.; Sawyer, K.A.; Burke, W.; Costanza, M.E.; Evans, W.P.; Foster, R.S.; Hendrick, E.; Eyre, H.J.; Sener, S. *CA Cancer J Clin* **2003**, *53*, 141-169.

(63) *Cancer Prevention and Early Detection Facts and Figures 2005*, American Cancer Society.

(64) Hiramatsu, K.; Takahashi, K.; Yamaguchi, T.; Matsumoto, H.; Miyamoto, H.; Tanaka, S.; Tanaka, C.; Tamamori, Y.; Imajo, M.; Kawaguchi, M.; Toi, M.; Mori, T.; Kawakita, M. *Clinical Cancer Research* (**2005**) *11*, 2986-2990.

(65) Philips, M.; Cataneo, R.N.; Ditkoff, B.A.; Fisher, P.; Greenberg, J.; Gunawardena, R.; Kwon, C.S.; Rahbari-Oskoui, F.; Wong, C. *The Breast Journal* (**2003**) *9*, 184-191.

(66) McDonald, J. *Impedance Spectroscopy*, Wiley, New York, 1987.

CHAPTER 6

CONCLUSIONS AND FUTURE DIRECTIONS

Conclusions

In this dissertation, the properties of low-density self-assembled monolayers have been examined from a fundamental standpoint through characterization of electrochemical properties, storage stability, and thiol mobility, and from an applied standpoint through assessment of technologically relevant functions such as impedance switching and analyte intercalation.

In Chapter 2, we demonstrated that low-density SAMs are electrochemically responsive to the application of even small electrical potentials. We extended prior studies on MHA SAMs to shorter MUA thiols, and we further extended our observations to samples produced on silver substrates in addition to gold. Impedance spectroscopy conducted in PBS buffer at physiological pH values has proven to be a sensitive method for studying reversible transitions in low-density monolayers, and tunable responses to electrical stimuli have been demonstrated using this tool. The potential-induced changes in impedance were found to be fully reversible, as demonstrated by the repeated switching of low-density SAMs of MHA and MUA on both gold and silver electrodes.

In Chapter 3, we addressed the issue of long-term storage stability of low-density SAMs. We conducted studies in which low-density self-assembled monolayers of

mercaptohexadecanoic acid on gold were stored under air, argon (25 and 4 °C), and ethanol. Analysis by electrochemical impedance spectroscopy showed no significant change in the electrochemical insulating properties of the air, argon, and ethanol samples over the course of 4 weeks. Oxidative degradation of these samples was also not observed by X-ray photoelectron spectroscopy. However, the fine structure of low-density SAMs as determined by Fourier transform infrared spectroscopy showed a trend toward decreasing alkyl chain fluidity over time. Increased ordering of the MHA molecules on the surface is a possible cause of these observations. The robust chemical and electrochemical stability of low-density SAMs under a variety of practical storage conditions points toward the applicability of these systems in potential technological applications.

In Chapter 4, we observed that density-defined micropatterning and high-temperature exposure had a consistent trend of effects on SAMs with respect to film thickness as measured by ellipsometry, conformational structure as measured by FTIR spectroscopy, and electrochemical barrier properties as measured by EIS. Elevated temperature appears to cause migration of thiolates from high density regions to low density regions. This effect was observed to depend both on temperature and on SAM chain length, suggesting interplay between the energetics of the gold-thiol interaction and inter-chain van der Waals interactions. Independent of the lateral migration effect, micropatterned SAMs of low-density MHA and MUA showed good thermal stability at temperatures up to 373 K and 333 K, respectively, which may have positive implications for potential technological applications.

In Chapter 5, we observed the intercalation of fatty acids (stearic and palmitic acid) and octadecyl rhodamine within low density monolayers, as assessed by electrochemical impedance spectroscopy, infrared spectroscopy, and surface plasmon resonance spectroscopy. A time-course study of intercalation showed that a steady increase of impedance accompanies intercalation of stearic acid until about 7 hours, when equilibrium is reached. The influence of external solvent on intercalation was also assessed, with more polar solvents promoting greater levels of intercalation.

Future Directions

Assessing the intercalation potential of a wider variety of analytes, including those with potential clinical relevance, is a logical next step for further study. Assessing factors such as analyte concentration and the influence of solution pH and ionic strength would also deepen our understanding of the intercalation process. Preparation of precursor molecules with chain lengths shorter than C11 would further test the limits of conformational flexibility and stimuli-responsiveness of the switchable surfaces. The influence of applied potential may also be more fully explored as a method for tuning binding capabilities and releasing trapped analytes. Such development of switchable low-density SAMs may not only provide greater understanding of this unique smart material platform, but may ultimately lead to exciting technological applications such as diagnostic sensors for non-invasive detection of disease markers and dynamic substrates for cell growth and tissue development.